

1N-20
136219

NASA Contractor Report 190797

Numerical Modeling of a Vortex Stabilized Arcjet

Gary E. Pawlas
University of Toledo
Toledo, Ohio

(NASA-CR-190797) NUMERICAL
MODELING OF A VORTEX STABILIZED
ARCJET Ph.D. Thesis, 1991 Final
Report (Toledo Univ.) ~~154 p~~

N93-14883

Unclas

G3/20 0136219

485812 172P

November 1992

NASA

Acknowledgements

I would like to take this opportunity to thank my advisor Dr. Theo G. Keith, Jr. for his support, knowledge, and understanding. Much of what I have learned during this research had nothing to do with fluid mechanics or numerical analysis. My co-advisor, Dr. Kenneth DeWitt, provided an excellent foundation for this research through a series of fundamental courses in transport phenomenon. Dr. Abdollah Afjeh and Dr. Paul F. Penko (at NASA Lewis Research Center) were gracious to serve as committee members.

This research was funded by NASA Lewis Research Center under the direction of Dr. Frank Curran of the Low Thrust Propulsion Branch. His experimental arcjet studies provided a guide for the development of this research. The computational facilities (and computer librarians) at NASA Lewis made this research effort possible.

As in most bodies of work occurring over a long time period many individuals contribute to its scope, content, understanding, and ultimately its success. Among those individuals are Dr. Paul Penko, Greg Wilson of Stanford University, and Dr. Datta Gaitonde at Wright-Patterson Air Force Base. Each has contributed greatly to my understanding and development of MacCormack's numerical algorithm. Dr. Milind Bakhle of NASA Lewis shared his understanding and expertise of the NASA Lewis computer systems.

The thoughts and prayers of friends and family too numerous to mention helped me through the inevitable ups and downs. Their concern was much appreciated and very helpful.

The most important pillar of support for me was my wife, Annette Arnone Pawlas. She trusted us enough to risk a long endeavor. Without her love and understanding none of this work would have been possible nor would it have mattered. She has helped me grow to be not only a better engineer but a better person. I can ask for nothing more.

An Abstract of
**Numerical Modeling
of a
Vortex Stabilized Arcjet**

Gary E. Pawlas

Submitted in partial fulfillment
of the requirements of the
Doctor of Philosophy Degree in
Engineering Science

The University of Toledo
December 1991

Arcjet thrusters are being actively considered for use in Earth orbit maneuvering applications. Satellite station-keeping is an example of a maneuvering application requiring the low thrust, high specific impulse of an arcjet. Experimental studies are currently the chief means of determining an optimal thruster configuration. Earlier numerical studies have failed to include all of the effects found in typical arcjets including complex geometries, viscosity and swirling flow.

Arcjet geometries are large area ratio converging-diverging nozzles with centerbodies in the subsonic portion of the nozzle. The nozzle walls serve as the anode while the centerbody functions as the cathode. Viscous effects are important because the Reynolds number, based on the throat radius, is typically less than 1,000. Experimental studies have shown a swirl or circumferential velocity component stabilizes a constricted arc.

This dissertation describes the equations governing flow through a constricted arcjet thruster. An assumption the flowfield is in local thermodynamic equilibrium leads to a single fluid plasma temperature model. An order of magnitude analysis reveals the governing fluid mechanics equations are uncoupled from the electromagnetic field equations. A numerical method is developed to solve the governing fluid mechanics equations, the Thin Layer Navier-Stokes equations. A coordinate transformation is employed in deriving the governing equations to simplify the application of boundary conditions in complex geometries.

An axisymmetric formulation is employed to include the swirl velocity component as well as the axial and radial velocity components. The numerical method is an implicit finite-volume technique and allows for large time steps to reach a converged steady-state

solution. The inviscid fluxes are flux-split and Gauss-Seidel line relaxation is used to accelerate convergence.

Converging-diverging nozzles with exit-to-throat area ratios up to 100:1 and annular nozzles were examined. Comparisons with experimental data and previous numerical results were in excellent agreement. Quantities examined included Mach number and static wall pressure distributions, and oblique shock structures. As the level of swirl and viscosity in the flowfield increased the mass flow rate and thrust decreased. The technique was used to predict the flow through a typical arcjet thruster geometry. Results indicate swirl and viscosity play an important role in the complex geometry of an arcjet by shifting the Mach contours upstream and reducing the mass flow rate and thrust.

A Dissertation
entitled

**Numerical Modeling
of a
Vortex Stabilized Arcjet**

by
Gary E. Pawlas

as partial fulfillment of the requirements of
the Doctor of Philosophy Degree in
Engineering Science

Theo G. Keith. J
Advisor

Dean of the Graduate School

The University of Toledo
December 1991

Table of Contents

	<i>Page</i>
Acknowledgements	iii
Abstract	iv
List of Tables	viii
List of Figures	ix
Nomenclature	xii
 <i>Chapter 1</i> Introduction	 1
1.1 Background	1
1.2 Previous Research	2
1.3 Present Research Effort	5
 <i>Chapter 2</i> Governing Equation Formulation	 6
2.1 Introduction	6
2.2 Basic Assumptions	6
2.3 Order of Magnitude Analysis	10
2.4 Non-dimensional Governing Equations	19
2.5 Transformed Governing Equations	25
 <i>Chapter 3</i> Numerical Method	 30
3.1 Introduction	30
3.2 Implicit Formulation	30
3.2.1 Inviscid Flux Vectors	32
3.2.2 Viscous Flux Vector	35
3.2.3 Source Terms	37
3.2.4 Finite Volume Approximation	38
3.3 Boundary Conditions	39
3.3.1 Upper and Lower Boundaries	40
3.3.1.1 Explicit Implementation	40
3.3.1.2 Implicit Implementation	46
3.3.2 Inlet and Outlet Planes- Method of Characteristics	50
3.3.2.1 One-dimensional MOC Example	51
3.3.2.2 Application of MOC in Present Research	56
3.4 Solution Procedure	58

<i>Chapter 4</i>	Grid Generation	59
4.1	Introduction	59
4.2	Previous Research	60
4.3	Wall Orthogonality Modifications	69
<i>Chapter 5</i>	Results and Discussion	78
5.1	Introduction	78
5.2	Previous Numerical Research	78
5.3	Nozzle Performance Parameters	79
5.4	Computations and Comparisons for a Variety of Nozzles	80
5.4.1	Dutton's initial nozzle	81
5.4.2	Dutton's experimental nozzle	95
5.4.3	Back and Cuffel nozzle	103
5.4.4	Annular nozzle	108
5.4.5	100:1 area ratio nozzle	114
5.4.6	Arcjet thruster nozzle	118
5.5	Computational Requirements	121
<i>Chapter 6</i>	Summary and Recommendations	123
6.1	Summary	123
6.2	Conclusions	124
6.2	Recommendations for Future Research	126
References		128
Appendix A	Derivation of Quasi-neutrality Condition	132
Appendix B	Derivation of the Transformed Governing Equations	134
Appendix C	Derivation of the Inviscid Flux Vector Jacobians	144
Appendix D	Derivation of the Implicit Viscous and Source Term Matrices	149
Vita		153

List of Tables

<i>Table</i>	<i>Page</i>
2.1 Momentum Equation Order of Magnitude Analysis	15
2.2 Energy Equation Order of Magnitude Analysis for $r_{th} = 2.0 \times 10^{-4} \text{ m}$	16
2.3 Energy Equation Order of Magnitude Analysis for $r_{th} = 2.0 \times 10^{-3} \text{ m}$	17
2.4 Ohm's Law Order of Magnitude Analysis	18
3.1 Required Boundary Conditions at Inlet and Outlet Plane Boundaries	52
4.1 Grid Generation Notation (Rosetta Stone)	71
5.1 Nozzle performance summary for Dutton's initial nozzle	85
5.2 Nozzle performance summary for Dutton's experimental nozzle	101
5.3 Nozzle performance summary for the annular nozzle	113

List of Figures

<i>Figure</i>	<i>Page</i>
1.1 Constricted Arcjet Schematic	1
1.2 Characteristic regions of flow through a wall and swirl stabilized arcjet thruster (after Neuberger, 1975)	3
3.1 Direction of streamwise flux travel	33
3.2 Inlet plane boundary condition schematic	56
4.1 Mismatch between an irregular boundary and a rectangular grid	59
4.2 Grid clustering near a solid surface	59
4.3 Coordinate transformation between physical plane and computational plane	60
4.4 Grid boundaries in the computational plane	62
4.5 Thomas and Middlecoff boundary in the physical plane	63
4.6 Grid distribution for Thomas & Middlecoff geometry; equal spacing on boundary BC, (a) Laplace solution, (b) Poisson solution	64
4.7 Grid distribution for Thomas & Middlecoff geometry; clustered spacing on boundary BC, (a) Laplace solution, (b) Poisson solution	66
4.8 Poisson grid distributions for an arcjet thruster geometry with, (a) Same point distributions, (b) different point distributions, on top and bottom boundaries	67
4.9 Magnified view of Poisson grid distributions for an arcjet thruster geometry ((1) upstream nozzle wall, (2) nozzle throat) with, (a) same point distributions, (b) different point distributions, on top and bottom boundaries	68
4.10 Expected orthogonal boundary grid distribution for an unclustered boundary grid pt. distribution	69
4.11 Expected orthogonal boundary grid distribution for a clustered boundary grid pt. distribution	69
4.12 Modified control function grid distributions for an arcjet thruster geometry (a) same point distributions, (b) different point distributions, on top and bottom boundaries	73
4.13 Magnified view of modified control function grid distributions for an arcjet thruster geometry ((1) upstream nozzle wall, (2) nozzle exit) with, (a) same point distributions, (b) different point distributions, on top and bottom boundaries	74
4.14 Modified control functions with spacing control grid distributions for an arcjet thruster geometry, different point distributions on top and bottom boundaries, (a) entire thruster, magnified views of (b) upstream nozzle wall and (c) nozzle exit	74

5.1	Inlet swirl velocity boundary condition profiles	80
5.2	Grid for Dutton's initial nozzle (DIN), (a) inviscid, 45 x 30, (b) viscous, 45 x 40	82
5.3	Inviscid Mach contours in DIN, (a) unswirled flow, (b) 30° constant angle swirl boundary condition	83
5.4	Viscous Mach contours in DIN (Re= 10,000), (a) unswirled flow, (b) 30° constant angle swirl	84
5.5	Comparison of inviscid unswirled and swirling (30° constant angle) nozzle inlet density and axial velocity profiles in DIN	86
5.6	Viscous Mach contours in DIN (Re= 10,000), (a) 52.5° forced vortex, (b) 40° free vortex	88
5.7	Swirl velocity profiles at the inlet, throat, and exit for a 30° constant angle inlet profile in DIN, (a) inviscid, (b) viscous (Re= 10,000) flow	89
5.8	Swirl velocity profiles at the inlet, throat, and exit in DIN for a (a) 52.5° forced vortex, (b) 40° free vortex inlet profile in viscous flow (Re= 10,000)	90
5.9	Dependence of inlet swirl number in DIN on inlet swirl profile and maximum inlet swirl angle in viscous flow (Re= 10,000)	91
5.10	Non-dimensionalized mass flow rate in DIN for a given inlet swirl profile and maximum inlet swirl angle in viscous flow (Re= 10,000)	91
5.11	Dependence of nozzle performance in DIN on inlet swirl number and viscosity (Re= 10,000)	92
5.12	Dependence of nozzle performance in DIN on inlet swirl number and Reynolds number (30° constant angle)	92
5.13	Convergence in DIN as a function of viscosity, grid size, and swirl (Re= 10,000 in viscous flow)	93
5.14	Mass conservation in DIN (axial mass flow rate divided by inlet mass flow rate, Re= 10,000 in viscous flow)	94
5.15	(a) Viscous grid in Dutton's experimental nozzle (DEN) (50 x 40) and (b) inlet stagnation pressure profiles for Dutton's experimental nozzle	96
5.16	Viscous results for a 40° forced vortex inlet swirl profile in DEN, (a) Mach contours, (b) comparison of experimental and numerical static wall pressure distributions (Re= 10,000)	97
5.17	Viscous results for a 50° constant angle inlet swirl profile in DEN, (a) Mach contours, (b) comparison of experimental and numerical static wall pressure distributions (Re= 10,000)	98
5.18	Viscous results for a 40° forced vortex inlet swirl profile in DEN, (a) Mach contours, (b) comparison of experimental and numerical static wall pressure distributions (Re= 10,000)	99
5.19	Swirl velocity profiles at the inlet, throat, and exit in DEN for a (a) 40° forced vortex, (b) 50° constant angle inlet profile in viscous flow (Re= 10,000)	100

5.20	Viscous results for Back & Cuffel (B&C) nozzle in unswirled flow, (a) 60 x 40 grid, (b) Mach contours, (c) comparison of experimental and numerical static wall pressure distributions (Re= 10,000)	104
5.21	Viscous results for Back & Cuffel nozzle, (a) Swirling Mach contours, 60° constant angle, Si= 0.568, (b) swirled and unswirled centerline Mach number distributions (Re= 10,000)	105
5.22	Swirl velocity profiles at the inlet, throat, and exit in B&C nozzle for a 60° constant angle inlet profile in viscous flow (Re= 10,000)	107
5.23	Viscous grid in B&C nozzle, 60 x 40, with cross-stream mesh lines orthogonal to nozzle boundaries	107
5.24	Viscous results for an annular nozzle (a) 50 x 40 grid, (b) unswirled Mach contours (Re= 10,000)	109
5.25	Viscous results for an annular nozzle, (a) swirling Mach contours, 70° constant angle (Si= 1.85), (b) swirl velocity profiles at the inlet, throat, and exit (Re= 10,000)	110
5.26	Viscous results for an annular nozzle with a modified asymptotic inlet swirl profile, (a) swirling Mach contours, 70° constant angle (Si= 0.987), (b) swirl velocity profiles at the inlet, throat, and exit (Re= 10,000)	112
5.27	Viscous results for a 100:1 area ratio nozzle (a) 60 x 45 grid, (b) unswirled Mach contours, (c) swirling Mach contours, 30° constant angle (Re= 850)	115
5.28	Unswirled Mach contours for a 100:1 area ratio nozzle (Re= 5,000)	116
5.29	Comparison of measured and predicted exit plane pitot pressure distribution in 100:1 area ratio nozzle	116
5.30	Viscous results for an arcjet thruster nozzle (a) 60 x 45 grid, (b) unswirled Mach contours (Re= 850)	119
5.31	Viscous results for an arcjet thruster nozzle, (a) swirling Mach contours, 30° constant angle (Si= 0.320), (b) swirl velocity profiles at the inlet, throat, and exit (Re= 850)	120
B.1	Normal and Tangential Velocity Components at Surfaces of Constant η and ξ	136

Nomenclature

A, B	Jacobian matrices of \hat{F} , \hat{G} (Appendix B)
\vec{B}	magnetic field vector
c	speed of sound (Sec. 2.4)
C_A, C_B	Jacobian matrices diagonalizing A, B
C_D	discharge coefficient (Sec. 5.3)
C_I	Jacobian matrix of \hat{H}
c_p	heat capacity at constant pressure
CFL	Courant-Friedrichs-Lewy condition (Section 5.4)
d_A, d_B	magnitude of inverse metrics used in u', v' (Appendix B)
DIN	Dutton's initial nozzle
DEN	Dutton's experimental nozzle
DPR	data processing rate (Section 5.4)
e	unit of electric charge
\vec{E}	electric field vector
e_i	internal energy per unit mass
e_t	total energy per unit mass
E_t	total energy per unit volume
\vec{F}, \vec{G}	inviscid axial and radial flux vectors
\hat{F}, \hat{G}	inviscid flux vectors in rotated coordinates (Section 2.5)
\vec{H}	inviscid source term vector
\hat{H}	inviscid source term in rotated coordinates (Section 2.5)
i, j	axial and radial grid coordinates
$I, JMAX$	maximum axial and radial grid coordinates
\vec{j}	current vector
J	Jacobian of coordinate transformation
k_B	Boltzmann's constant
LTE	local thermodynamic equilibrium (Section 2.2)
m_e	electron mass
\dot{m}	mass flow rate (Section 5.3)
M	Mach number
M_a, M_b	Jacobian matrices used in implicit treatment of viscous terms (Appendix D)
N	Jacobian matrix used in implicit treatment of viscous terms (Appendix D)
n_e	electron number density
P	pressure
P', Q'	grid generation control functions (Table 4.1)
P_M	Magnetic pressure number

Pr	Prandtl number
\vec{q}	heat flux vector
\vec{Q}	vector of conserved variables, Eq. (2.37)
r	radial coordinate
R_A, R_B	rotation matrices of A, B
R_C	conduction number
Re	Reynolds number based on throat radius (Sec. 2.4)
R_F	magnitude of current fluctuation
R_H	Hall parameter
R_{IN}	Magnetic Reynolds number
R_L	Electric heating number
R_S	radiation number
r_{th}	throat radius
RHS	right hand side of Eq. (3.15)
S	Jacobian of \vec{V} with respect to \vec{Q}
S_i	inlet swirl number (Section 5.3)
S_R	radiation source term
T	temperature (Section 2.4), thrust (Section 5.3)
t	time
u, v, w	axial, radial, and swirl (circumferential) velocity components
u', v'	normalized and rotated velocity components (Appendix B)
\vec{v}	velocity vector
\vec{V}	vector of non-conserved (primitive) variables (Appendix C)
V_{ij}	volume of cell i, j
z	axial coordinate

Greek

γ	ratio of specific heats, c_p/c_v
δ	implicit change of a given quantity, See Eq. (3.7)
ϵ	permittivity of vacuum
η_{SI}	specific impulse efficiency (Section 5.3)
η_{vs}	vacuum stream thrust efficiency (Section 5.3)
θ	ratio of v/u , inlet plane boundary condition (Section 3.3.2.2)
Λ_A, Λ_B	diagonal eigenvalue matrices of A, B
μ_M	permeability of vacuum
ξ, η	transformed axial and radial coordinates
ρ	density
ρ_e	net space charge density
σ	electrical conductivity

ϕ	swirl angle= w/u , inlet plane boundary condition (Section 3.3.2.2)
$\vec{\tau}$	shear stress tensor
$\vec{\Omega}$	vector of inlet or exit plane boundary conditions (Section 3.3.2)

Subscripts

c	centerline
com	viscous terms contained in both cartesian and cylindrical formulations (Sec. 3.2.2)
cyl	viscous terms contained only in a cylindrical formulation (Sec. 3.2.2)
e	exit
i	inlet
id	ideal, one-dimensional isentropic values at flow stagnation conditions
ii	ith value of the vector quantity
i,j	axial and radial grid coordinates
o	denotes a dimensional reference value
t	throat
w	wall

Superscripts

\wedge	denotes a dimensional quantity or a vector quantity in transformed coordinates
-1	matrix inverse
+, -	downstream and upstream propagated flux-split variable
n	time level of computation
v	viscous terms
'	denotes a quantity containing both inviscid and viscous terms
\sim	block matrix term (Section 3.2.4)
*	conditions at $M=1$

Difference Operators

$$\frac{D_+ Z_{ij}}{\Delta \xi} \equiv Z_{i+1,j} - Z_{i,j}$$

$$\frac{D_- Z_{ij}}{\Delta \xi} \equiv Z_{i,j} - Z_{i-1,j}$$

$$\frac{D_+ Z_{ij}}{\Delta \eta} \equiv Z_{i,j+1} - Z_{i,j}$$

$$\frac{D_- Z_{ij}}{\Delta \eta} \equiv Z_{i,j} - Z_{i,j-1}$$

Introduction

1.1 Background

An *arcjet* is an electrothermal propulsion device in which a gas propellant is heated by means of a high temperature arc. The propellant expands through a large area ratio nozzle to produce thrust. A typical constricted arcjet configuration is shown in Fig. 1.1. The propellant gas enters a chamber, flows over and past an electrically conducting rod serving as a cathode. An electric arc is established between the cathode and the nozzle walls, which serve as an anode. The arc heats the gas to a high temperature, causing an expansion and resultant acceleration of the gas out through a constant area constrictor region and into the divergent portion of the nozzle where the arc attaches diffusely.

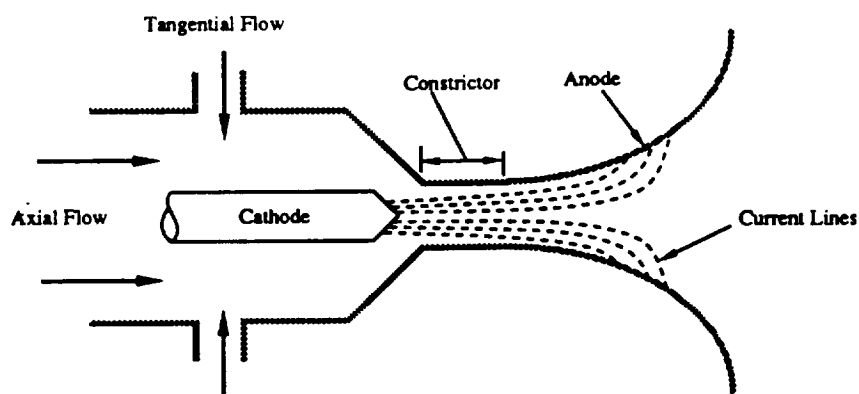


Figure 1.1 Constricted Arcjet Schematic

The constrictor region stabilizes the inherently unstable columnar arc. A "cool" boundary layer surrounds the high temperature ($\gg 10,000$ K) arc, preventing erosion of the nozzle walls. The tangential or swirl velocity component imparted to the inlet gas flow also provides a stabilizing force by establishing a radial pressure gradient. The pressure gradient opposes any kinking occurring in the arc column [1].

The arcjet was identified as a prime candidate for space missions requiring high specific impulse (1,000 -2,000 seconds) and low thrust (≈ 1 lbf) propulsion devices in the

1960's [2]. In contrast the maximum specific impulse of chemical rockets is on the order of 200-400 seconds, and is limited by the chemistry of available fuels [3,4]. A typical mission requiring a high specific impulse would be to maintain a satellite's altitude in a geostationary orbit. Arcjets requiring 1-200 kilowatts (Kw) of power were being developed for a mission such as this in the 1960's. The research and development effort had led to continuous operation of up to 500 hours and overall efficiencies of up to 55 percent. However, excessive weight in the electric power generating systems was cited as a main development hurdle.

Experimental development efforts have identified several items as greatly affecting arcjet performance. As mentioned previously, imparting a swirl or tangential velocity component to the inlet gas flow has been found (as early as 1909, [5]) to stabilize the arc column and reduce erosion of the cathode and nozzle walls. Recent work at NASA by Curran [6] has confirmed the need for a strongly swirling flow.

Unsurprisingly, the cathode shape, nozzle geometry, and constrictor length were also found [6] to have an effect on gross performance parameters such as specific impulse and thrust as well as on localized phenomenon such as the downstream current attachment location, nozzle wall temperatures, etc. In addition, the operating conditions and dimensions of arcjet thrusters lead to Reynolds numbers below 1,000, indicating the flows are laminar yet highly viscous [7]. Any constricted arcjet model developed needs to include the effects of swirl, geometry, and viscosity.

1.2 Previous Research

Because of the modest computational facilities available in the 1960's, the research effort regarding arcjets was largely experimental. The earliest modeling efforts were applicable in a constant area region downstream of the cathode tip (See Fig. 1.2). Among the earliest modeling efforts were those of Stine and Watson [8] and Watson and Pegot [9]. Their simplifying assumptions of unswirled, fully developed, one dimensional flow led to an uncoupled energy equation which accurately modeled the enthalpy distribution in the arc.

Later research by Neuberger [10,11] and Shaeffer [1] involved an axisymmetric model in a constant area geometry, with viscous, swirling flow. Shaeffer also included turbulence and radiation transport effects in his model. Neuberger's results indicate the effect of swirl was small in geometries with large constrictor length/diameter ratios but in small ratio geometries higher averaged enthalpy and efficiencies were reached. Shaeffer demonstrated the stabilizing effect of swirl on the arc column decreased unless secondary gas injection occurs.

However, in examining constant area geometries both Neuberger and Shaeffer assumed radial velocities were small compared to the axial and tangential (swirl) velocities and axial gradients were negligible in comparison to radial gradients. These assumptions

are essentially boundary layer assumptions (also called the quasi-cylindrical assumption) and when applied to an axisymmetric, swirling flow are termed the weak swirl approximation [13]. In this context, they result in a greatly reduced radial momentum equation

$$\frac{\rho w^2}{r} = \frac{\partial P}{\partial r}$$

which is a balance between the centrifugal force and the radial pressure gradient. When no assumptions are made about radial velocity or axial gradient magnitudes a strongly swirling flow can be modeled and consists of the axisymmetric Navier-Stokes equations. The radial momentum equation for a strongly swirling flow is given by

$$\frac{1}{r} \frac{\partial}{\partial r} (r \rho v^2) + \frac{\partial}{\partial z} (r \rho u v) - \frac{\rho w^2}{r} = -\frac{\partial P}{\partial r} + \frac{1}{r} \frac{\partial}{\partial r} (r \tau_{rr}) + \frac{\partial}{\partial z} (\tau_{rz}) + \frac{\tau_{\theta\theta}}{r}$$

Obviously a great deal of the physics of the flow is neglected in an assumption of weakly swirling flow. Yet in a constricted arcjet, in which the geometry varies greatly with axial location, no assumptions can be made about radial velocity or axial gradient magnitudes. Thus, an accurate treatment of the flow from a fluid mechanics standpoint requires a strongly swirling flow to be modeled using the Navier-Stokes equations.

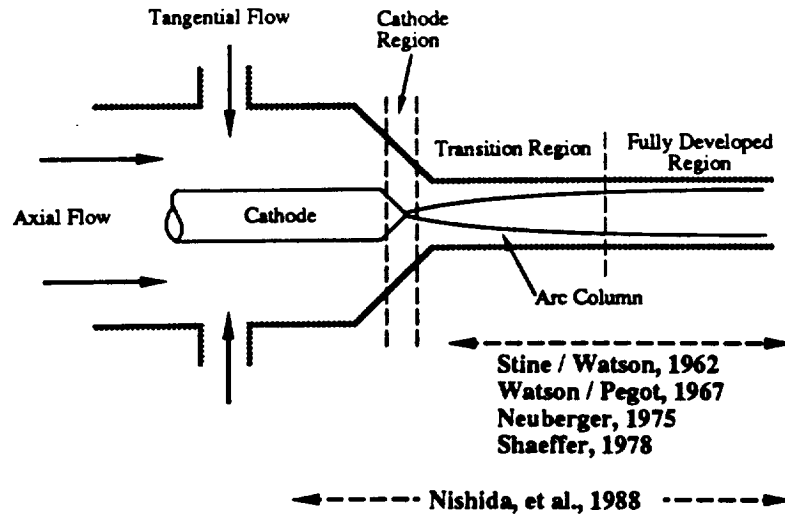


Figure 1.2 Characteristic regions of flow through a wall and swirl stabilized arcjet thruster (after Neuberger, 1975)

It should also be mentioned that a strongly swirling flow is generally indicated by an inlet swirl number, S_i , greater than 1.0. S_i is defined by

$$S_i \equiv \frac{\int_{r_{ci}}^{r_{wi}} \rho u w r^2 dr}{r_{wi} \int_{r_{ci}}^{r_{wi}} \rho u^2 r dr}$$

which is seen to be the axial flux of angular momentum divided by the inlet wall radius times the axial flux of axial momentum, and is a direct measure of the level of swirl at the nozzle inlet. The Neuberger and Shaeffer studies were limited to swirl numbers less than 1.0 and thus were limited to examining the effects of weakly swirling flow. In general, weakly swirling and unswirled flows as well as strongly swirled flows can be examined using the axisymmetric Navier–Stokes equations.

More recently, Nishida, *et. al* [13], modeled a realistic, axisymmetric arcjet geometry, i.e., a diverging nozzle exit as in Fig. 1.1, assuming unswirled, inviscid flow. Also included were nonequilibrium ionization-recombination effects for an argon propellant. The mass flow rate, discharge current, and geometry were that of an experimental thruster undergoing testing. Numerical results indicated a decrease in thrust and specific impulse as the constrictor length increased. No comparisons with experimental data were provided.

In related work, [14,15], researchers at the University of Stuttgart have been developing numerical models of magnetoplasmadynamic (MPD) thrusters (in which high current densities generate self-magnetic fields producing substantial electromagnetic acceleration of the flow and hence greatly complicate the governing equations). Their initial models have been inviscid and partly two-dimensional in nature. Predicted current density distributions in cylindrical geometries have compared favorably with experimental results. Further development efforts are proceeding to reduce the mass flow errors (up to 10%) and implement more realistic subsonic inlet boundary conditions in place of the supersonic inlet conditions currently used.

Worthy of special mention are the detailed analyses of the anode contraction region in high intensity arcs operating at atmospheric pressure performed by Pfender and his students, [16-19]. The analyses used a two temperature model, which accounts for nonequilibrium effects near the anode or cathode surface by including energy equations for electrons and heavy particles (ions and neutral atoms) in addition to the continuity and momentum equations.

No attempt has been made in any of the arcjet modeling efforts discussed above to

include a detailed analysis of regions near the cathode tip or anode wall. The complexity of an analysis of the entire flowfield precludes the ability to accurately predict details in these regions of tremendous current, temperature, and velocity gradients. Eventually electrothermal thruster models would need to incorporate accurate boundary conditions in these regions.

In summary, none of the works examined to date have incorporated the ability to model the effects of strongly swirling, viscous flows throughout an entire arcjet thruster.

1.3 Present Research Effort

In this dissertation a numerical model of a constricted arcjet thruster is developed. The formulation includes all of the flow features found to have significant effects on the operation of a thruster including realistic geometries, viscous effects and a strongly swirling flow.

The continuity, momentum, energy, and electromagnetic field equations are derived in general terms assuming the flowfield is in local thermodynamic equilibrium (LTE). Thus the flow is assumed to have a single mean temperature (electrons, ions and neutral atoms have the same temperature) at any point. This assumption is valid everywhere except in regions close to the anode and cathode surfaces.

An order of magnitude analysis demonstrates the fluid mechanics equations (continuity, momentum, and energy) are uncoupled from the electromagnetic field equations when insignificant terms are neglected. The only link between the two equation sets is through the electrical conductivity, which is a highly non-linear function of pressure and temperature.

Both equation sets are formulated in transformed coordinates. The fluid mechanics equations solved are the Thin Layer Navier–Stokes (TLNS) equations. MacCormack's [20] implicit Gauss–Seidel Line Relaxation method is modified to solve the axisymmetric form of the TLNS equations. The iterative technique needed to obtain a converged solution of the TLNS algorithm and the electromagnetic field equations (solved by a forward in time, centered in space algorithm) is also discussed.

A grid generation algorithm is also developed to create the numerical mesh. The algorithm allows grid to be clustered near upper and lower surfaces as well as at the throat. Thus, regions containing large gradients such as in viscous boundary layers or in the constrictor can be adequately resolved. In addition, the algorithm can generate mesh orthogonal to upper and lower surfaces, allowing the effect of grid orthogonality on solution accuracy to be determined.

The TLNS portion of the formulation (valid for flow through a thruster with the arc turned off, i.e., cold flow) is validated by comparison with experimental data obtained for flows through converging-diverging nozzles. Finally, the effect of swirl on flow through a geometry representative of a thruster is examined.

Governing Equation Formulation

2.1 Introduction

In this chapter the equations governing the flow through a constricted arcjet thruster are presented and non-dimensionalized. An order of magnitude analysis is performed to determine which terms in the governing equations have a negligible effect on the thruster flowfield. A non-dimensionalization is applied to the reduced set of governing equations. Finally, a coordinate transformation is applied to derive the governing fluid mechanics and electromagnetic field equations in transformed coordinates.

2.2 Basic Assumptions

The following assumptions will be made in order to derive the governing equations for a vortex stabilized arcjet thruster:

1) The flowfield is assumed to be in local thermodynamic equilibrium (LTE). Thus the electron, ion, and heavy or neutral particle temperatures are assumed equal and can be equated to a single mean plasma temperature. This results in a single fluid plasma model. This continuum approach is not valid near the anode and cathode surfaces where kinetic theory, i.e. a two temperature plasma model, should be used, [1, 10, 16].

2) The plasma is assumed optically thin, i.e., reabsorption of emitted radiation is neglected, [10, 19].

3) The net space charge density, ρ_e , is assumed to be zero. This results in a quasi-neutral plasma. Appendix A examines the validity of this assumption, [10, 17].

4) External magnetic fields and the effects of gravity are neglected.

5) The Lorentz force (self induced magnetic force) is included in the momentum equation and the transport of electron enthalpy due to the drift (diffusion) of the electrons is included in the energy equation. These terms are, respectively [16, 18]

$$\mathbf{j} \times \vec{B} ; \quad \frac{5 k_B}{2 e} \mathbf{j} \cdot \nabla T$$

Expressions for energy change due to volume expansion and viscous dissipation are also included in the energy equation. An order of magnitude analysis will be performed to determine what terms are retained in the governing equations.

Using the above five assumptions the governing equations for the plasma may be written [21, 22, 23]. These include the continuity equation

$$\frac{\partial \rho}{\partial t} + \nabla \cdot \rho \vec{v} = 0 \quad (2.1)$$

the momentum equation

$$\rho \frac{D\vec{v}}{Dt} = -\nabla P - \nabla \cdot \tau + \mathbf{j} \times \vec{B} \quad (2.2)$$

where τ is the shear stress tensor and if Stoke's assumption for the bulk viscosity is made, may be expressed as

$$\tau_{ij} = -\mu \left[\left(\frac{\partial v_i}{\partial x_j} + \frac{\partial v_j}{\partial x_i} \right) - \frac{2}{3} \delta_{ij} \frac{\partial v_k}{\partial x_k} \right]$$

The conservation of energy equation takes the following form

$$\rho \frac{D e_t}{Dt} = -\nabla \cdot \vec{q} - \nabla \cdot P \vec{v} - \nabla \cdot (\tau \cdot \vec{v}) + \frac{j^2}{\sigma} - S_R + \frac{5 k_B}{2 e} \mathbf{j} \cdot \nabla T \quad (2.3)$$

or

$$\frac{\partial E_t}{\partial t} + \nabla \cdot E_t \vec{v} = -\nabla \cdot \vec{q} - \nabla \cdot P \vec{v} - \nabla \cdot (\tau \cdot \vec{v}) + \frac{j^2}{\sigma} - S_R + \frac{5 k_B}{2 e} \mathbf{j} \cdot \nabla T$$

where

$$\vec{q} = -k \nabla T$$

e_t = total energy per unit mass

$E_t = \rho e_t$ = total energy per unit volume

k_B = Boltzmann's constant

e = unit of electric charge

c_p = specific heat at constant pressure/unit mass

The terms on the right hand side of the Eq. (2.3) represent a change in energy due to heat conduction, volume changes, viscous dissipation, Joule heating, radiation, and the electron enthalpy flux.

Neglecting electron pressure effects and ion slip [22, 23] the Generalized Ohm's Law can be written

$$\frac{\sigma m_e}{n_e e^2} \frac{\partial \vec{j}}{\partial t} + \vec{j} = \sigma \left(\vec{E} + \vec{v} \times \vec{B} \right) - \frac{\sigma}{n_e e} \vec{j} \times \vec{B} \quad (2.4)$$

where

σ = electrical conductivity
 n_e = electron number density
 m_e = electron mass
 e = unit of electric charge

The three terms on the right hand side of the last equation represent the applied electric field, the induced field due to the bulk movement of the plasma, and the Hall effect due to the interaction of the current with the magnetic field, respectively.

In addition the electromagnetic fields obey Maxwell's equations, which are, for a net space charge density equal to zero (Assumption 2); the induction law

$$\nabla \times \vec{E} = - \frac{\partial \vec{B}}{\partial t} \quad (2.5)$$

This implies $\nabla \cdot \vec{B} = 0$ as may be seen by taking the divergence of Eq. (2.5) (since the divergence of the curl of a vector field is zero).

By neglecting the magnetization of the plasma, the magnetic permeability is essentially that of a vacuum, and the current law is

$$\nabla \times \vec{B} = \mu_{M0} \vec{j} \quad (2.6)$$

where

μ_{M0} = permeability of vacuum
 $= 4 \pi \cdot 10^{-7}$ henry/m

If the divergence of the last equation is taken we obtain a current continuity equation:

$$\nabla \cdot \vec{j} = 0$$

In addition we will assume the plasma obeys the perfect gas law (even though ionized gases should not be considered perfect)

$$P = \rho R T \quad (2.7)$$

where

$$R = \mathcal{R} / \text{M.W.}$$

\mathcal{R} = universal gas constant

M.W. = molecular weight

Finally, we have the following set of dimensional governing equations (where the ^ indicates a dimensional quantity):

$$\text{Continuity Eq} \quad \frac{\partial \hat{\rho}}{\partial \hat{t}} + \hat{\nabla} \cdot \hat{\rho} \hat{\mathbf{v}} = 0 \quad (2.8)$$

$$\text{Momentum Eq} \quad \hat{\rho} \frac{\hat{D} \hat{\mathbf{v}}}{\hat{D} \hat{t}} = - \hat{\nabla} \hat{P} - \hat{\nabla} \cdot \hat{\boldsymbol{\tau}} + \hat{\mathbf{j}} \times \hat{\mathbf{B}} \quad (2.9)$$

Energy Eq

$$\frac{\partial \hat{E}_t}{\partial \hat{t}} + \hat{\nabla} \cdot \hat{E}_t \hat{\mathbf{v}} = - \hat{\nabla} \cdot \hat{\mathbf{q}} - \hat{\nabla} \cdot \hat{\mathbf{p}} \hat{\mathbf{v}} - \hat{\nabla} \cdot (\hat{\boldsymbol{\tau}} \cdot \hat{\mathbf{v}}) + \frac{\hat{j}^2}{\hat{\sigma}} - \hat{S}_R + \frac{5}{2} \frac{\hat{k}_B}{\hat{e}} \hat{\mathbf{j}} \cdot \hat{\nabla} \hat{T} \quad (2.10)$$

Generalized Ohm's Law

$$\frac{\hat{\sigma} \hat{m}_e}{\hat{n}_e \hat{e}^2} \frac{\partial \hat{\mathbf{j}}}{\partial \hat{t}} + \hat{\mathbf{j}} = \hat{\sigma} \left(\hat{\mathbf{E}} + \hat{\mathbf{v}} \times \hat{\mathbf{B}} \right) - \frac{\hat{\sigma}}{\hat{n}_e \hat{e}} \hat{\mathbf{j}} \times \hat{\mathbf{B}} \quad (2.11)$$

Induction

$$\hat{\nabla} \times \hat{\mathbf{E}} = - \frac{\partial \hat{\mathbf{B}}}{\partial \hat{t}} \quad (2.12)$$

Current

$$\hat{\nabla} \times \hat{\mathbf{B}} = \mu_{Mo} \hat{\mathbf{j}} \quad (2.13)$$

$$\hat{\nabla} \cdot \hat{\mathbf{B}} = 0$$

$$\hat{\nabla} \cdot \hat{\mathbf{j}} = 0$$

Equation of State

$$\hat{P} = \hat{\rho} \hat{R} \hat{T} \quad (2.14)$$

2.3 Order of Magnitude Analysis

The total number of equations including the equation of state is 15. The 22 dimensional variables are (where the superscript " ^ " indicates a **dimensional** value of the quantity)

$$\widehat{\vec{v}}, \widehat{\vec{B}}, \widehat{\vec{E}}, \widehat{\vec{j}}, \widehat{\rho}, \widehat{P}, \widehat{T}, \widehat{\sigma}, \widehat{k}, \widehat{\mu}, \widehat{n_e}, \widehat{c_p}, \widehat{S_R}, \gamma$$

Letting: (where the subscript " o " indicates a **dimensional reference** value of the quantity)

$$\begin{aligned} \widehat{\vec{v}} &= \vec{v} \cdot v_o & \widehat{\vec{B}} &= \vec{B} \cdot B_o & \widehat{\vec{E}} &= \vec{E} \cdot E_o \\ \widehat{\vec{j}} &= \vec{j} \cdot \sigma_o E_o & \widehat{\rho} &= \rho \cdot \rho_o & \widehat{P} &= P \cdot P_o \\ \widehat{T} &= T \cdot T_o & \widehat{\sigma} &= \sigma \cdot \sigma_o & \widehat{k} &= k \cdot k_o \\ \widehat{\mu} &= \mu \cdot \mu_o & \widehat{n_e} &= n_e \cdot n_{eo} & \widehat{c_p} &= c_p \cdot c_{po} \\ \widehat{S_R} &= S_R \cdot S_{Ro} & \widehat{x_i} &= x_i \cdot r_{th} & \widehat{t} &= t \cdot (r_{th} / v_o) \\ \widehat{\tau} &= \tau \cdot (\mu_o \cdot v_o / r_{th}) & \widehat{\nabla} &= \nabla / r_{th} \\ \widehat{D/Dt} &= D/Dt \cdot v_o / r_{th} & \widehat{E_t} &= E_t \cdot (\rho_o \cdot c_{po} \cdot T_o) \end{aligned}$$

and where

$$\begin{aligned} P_o &= \rho_o R T_o \\ R &= c_{po} - c_{vo} & \gamma_o &= c_{po} / c_{vo} \end{aligned}$$

and defining j_o , E_o , and B_o with:

$$j_o = I_o / \pi r_{th}^2 \quad E_o = j_o / \sigma_o \quad B_o = \mu_{Mo} \sigma_o E_o r_{th}$$

We can now obtain the familiar non-dimensional parameters: Re, M, Pr, etc.,

$$Re = \text{Reynolds number} = v_o r_{th} \rho_o / \mu_o = \text{Inertia forces} / \text{viscous forces}$$

M_O = Mach number = $v_o / (\gamma_o R T_o)^{1/2}$ = Fluid velocity / speed of sound

Pr = Prandtl number = $c_{po} \mu_o / k_o$ = Momentum diffusivity / thermal diffusivity

P_M = Magnetic pressure number = $B_o^2 / (P_o \mu_{M_o})$
= Pressure of magnetic field forces / static pressure

R_L = Electric heating number = $\sigma_o E_o^2 r_{th}^2 / (k_o \cdot T_o)$
= Electric energy supplied / energy transport by heat conduction

R_S = radiation number = $S_{ro} \cdot r_{th}^2 / (k_o \cdot T_o)$
= Radiated energy / energy transport by heat conduction

R_C = conduction number = $k_o \sigma_o E_o / (e \cdot (k_o / r_{th}))$
= electrical conduction / thermal conduction

R_F = magnitude of current fluctuation = $m_e \cdot \sigma_o \cdot v_o / n_{eo} \cdot e^2 \cdot r_{th}$

R_H = Hall parameter = $\sigma_o B_o / n_{eo} e$ = Hall current / current parallel to electric field

R_{IN} = Magnetic Reynolds number = $v_o \cdot B_o / E_o = v_o \cdot \mu_{M_o} \cdot \sigma_o \cdot r_{th}$
= induced electric field / applied electric field

Substituting the above quantities into Eqs. (2.8) - (2.14) yields the following non-dimensional equations:

Continuity Eq
$$\frac{\partial \rho}{\partial t} + \nabla \cdot \rho \vec{v} = 0 \quad (2.15)$$

Momentum Eq
$$\rho \frac{D\vec{v}}{Dt} = - \frac{1}{\gamma_o M_o^2} \nabla P - \frac{1}{Re} \nabla \cdot \tau + \frac{P_M}{\gamma_o M_o^2} \vec{j} \times \vec{B} \quad (2.16)$$

Energy Eq

$$\begin{aligned} \frac{\partial E_t}{\partial t} + \nabla \cdot E_t \vec{v} = & \frac{1}{Re Pr} \nabla \cdot (k \nabla T) - \frac{\gamma_o - 1}{\gamma_o} \nabla \cdot P \vec{v} - \frac{M_o^2 (\gamma_o - 1)}{Re} \nabla \cdot (\tau \cdot \vec{v}) \\ & + \frac{R_L}{Re Pr} \frac{j^2}{\sigma} - \frac{R_S}{Re Pr} S_R + \frac{5}{2} \frac{R_C}{Re Pr} \vec{j} \cdot \nabla T \end{aligned} \quad (2.17)$$

Generalized Ohm's Law

$$R_F \frac{\sigma}{n_e} \frac{\partial \vec{j}}{\partial t} + \vec{j} = \sigma \vec{E} + R_{IN} \sigma \vec{v} \times \vec{B} - R_H \frac{\sigma}{n_e} \vec{j} \times \vec{B} \quad (2.18)$$

$$\text{Induction Law} \quad \nabla \times \vec{E} = - R_{IN} \frac{\partial \vec{B}}{\partial t} \quad (2.19)$$

$$\text{Current Law} \quad \nabla \times \vec{B} = \vec{j} \quad (2.20)$$

$$\text{Equation of State} \quad P = \rho T \quad (2.21)$$

Thus, the dimensional values of: P_o , ρ_o , T_o , μ_o , c_{po} , k_o , S_{ro} , σ_o , E_o , r_{th} , γ_o , n_{eo} are needed to estimate the similarity parameters. A review of recent arcjet literature [6, 24, 25, 26] provides the following representative values for a pure nitrogen propellant gas in an arcjet:

$$P_o = 1 \text{ atm} = 1 \times 10^5$$

$$T_o = 10,000 \text{ K}$$

$$r_{th} = 2.0 \times 10^{-4} \text{ m}$$

$$n_{eo} = 2 \times 10^{21} \text{ electrons / m}^3$$

$$j_o = 10 \text{ amp} / (\pi r_{th}^2) = 7.96 \times 10^7 \text{ amp / m}^2$$

$$\text{Mass flow rates} = 2.7 - 6.1 \times 10^{-5} \text{ kg / sec}$$

The following values were extracted from the nitrogen equilibrium transport properties compiled by Liu [16] from 12 independent sources

$$c_{po} = 5.55 \times 10^3 \text{ J / kg K}$$

$$\rho_o = 1.68 \times 10^{-2} \text{ kg / m}^3$$

$$\mu_o = 2.57 \times 10^{-4} \text{ N s / m}^2$$

$$k_o = 1.18 \text{ W / m K}$$

$$\sigma_o = 2.84 \times 10^3 \text{ 1 / ohm m}$$

$$S_{ro} = 1.47 \times 10^8 \text{ W / m}^3$$

Thus, the following values can now be calculated

$$E_o = j_o / \sigma_o = 28,028 \text{ volt / m}$$

$$B_o = \mu_{Mo} \sigma_o E_o r_{th} = 2.00 \times 10^{-2} \text{ kg / coul sec}$$

In addition, for nitrogen:

$$\begin{aligned} R &= \mathfrak{R} / \text{M.W.} = (8.314 \text{ J / mole K}) / (28 \times 10^{-3} \text{ kg / mole}) \\ &= 296.93 \text{ J / kg K} \end{aligned}$$

$$\gamma_o = c_{po} / (c_{po} - R) = 1.056$$

$$c_o = (\gamma_o R T_o)^{1/2} = 1,770 \text{ m / sec}$$

Values for the non-dimensional parameters independent of the velocity, v_o , i.e., Pr , P_M , R_L , R_S , R_C , and R_H , can now be calculated. The remaining non-dimensional parameters: M_o , Re , R_F , and R_{IN} , will be calculated for a range of velocities. Tables 2.1-2.4 contain the results of these calculations for nitrogen under the above conditions, with $r_{th} = 2.0 \times 10^{-4}$, and $2.0 \times 10^{-3} \text{ m}$.

In order to neglect the effect of a term in a governing equation the magnitude of the non-dimensional parameters of the term need to be 1-2 orders less than the next largest term in the governing equation. Examination of the parameters within the Momentum equation, Table 2.1, shows the only term that might be neglected is the Lorentz force but it is not at least an order of magnitude less than the pressure and viscous terms. Of course, the effect of the self induced magnetic field on the flow can only be examined by retaining this term.

Examination of the Energy equation, Table 2.2 shows the viscous dissipation term can be neglected. The radiation term could be neglected but will be retained. This term will appear as a source term in the governing equations when they are placed into the proper format used in the numerical procedure which will be discussed later.

Examination of the parameters in Ohm's Law, Table 2.4, indicates that the unsteady current term and the induced electric field can be neglected. However, the Hall effect, which contains a $\dot{j} \times \vec{B}$ term, is almost of sufficient magnitude to retain the term along with the applied electric field, \vec{E} , which has an order of magnitude of one. Yet, in the Momentum Equation the Lorentz force, which also contains $\dot{j} \times \vec{B}$, is of a much lower magnitude.

Examination of the non-dimensionalization reveals

$$\text{Lorentz Force} \Rightarrow \frac{P_M}{\gamma_o M_o^2} \approx \frac{1}{r_{th}^2}$$

$$\text{Hall Effect} \Rightarrow R_H \approx \frac{1}{r_{th}}$$

$$\text{Induced field} \Rightarrow R_{IN} \approx r_{th}$$

As the length parameter, r_{th} , of the non-dimensionalized equations increases both the Lorentz force and Hall effect terms decrease as shown above. Table 2.3 reveals that if r_{th} is increased by a factor of ten the Hall effect and induced field terms are negligible when compared to the applied field. The induced field increases proportional to r_{th} but it is of such a small magnitude that it may still be neglected. Tables 2.1 and 2.4 show that when r_{th} is increased by a factor of ten the $\vec{j} \times \vec{B}$ terms can both be neglected in their respective governing equations.

Thus, the order of magnitude analysis demonstrates that for completeness when modeling an arcjet the Hall effect term would be retained in Ohm's Law if the Lorentz force was included in the Momentum Equation. In this study, as in other arcjet studies [13, 16, 17] the effect of the induced field and Hall effect terms will be considered negligible and the Lorentz force will be retained in the Momentum Equation.

The final expression to examine is Eq. (2.19), the Induction Law. R_{IN} , whose magnitude is shown in Table 2.4, is sufficiently small to neglect the unsteady term.

The resulting set of non-dimensional governing equations is

$$\text{Continuity Eq} \quad \frac{\partial \rho}{\partial t} + \nabla \cdot \rho \vec{v} = 0 \quad (2.22)$$

$$\text{Momentum Eq} \quad \rho \frac{D\vec{v}}{Dt} = - \frac{1}{\gamma_0 M_0^2} \nabla P - \frac{1}{Re} \nabla \cdot \tau + \frac{P_M}{\gamma_0 M_0^2} \vec{j} \times \vec{B} \quad (2.23)$$

Energy Eq

$$\begin{aligned} \frac{\partial E_t}{\partial t} + \nabla \cdot E_t \vec{v} = & \frac{1}{Re Pr} \nabla \cdot (k \nabla T) - \frac{\gamma_0 - 1}{\gamma_0} \nabla \cdot P \vec{v} \\ & + \frac{R_L}{Re Pr} \frac{j^2}{\sigma} - \frac{R_S}{Re Pr} S_R + \frac{5}{2} \frac{R_C}{Re Pr} \vec{j} \cdot \nabla T \end{aligned} \quad (2.24)$$

Generalized Ohm's Law

$$\vec{j} = \sigma \vec{E} \quad (2.25)$$

Induction Law

$$\nabla \times \vec{E} = 0 \quad (2.26)$$

Current Law

$$\nabla \times \vec{B} = \vec{j} \quad (2.27)$$

Equation of State

$$P = \rho T \quad (2.28)$$

Table 2.1 Momentum Equation Order of Magnitude Analysis

$r_{th} = 2.0 \times 10^{-4} \text{ m}$					
V (m/s)	Mach No.	Re	Pressure Force	Viscous Force	Lorentz Force
17.7	0.01	.23	0.95 E+04	0.43 E+01	0.30 E+02
177	0.10	2.3	0.95 E+02	0.43 E+00	0.30 E+00
1,770	1.00	23.	0.95 E+00	0.43 E-01	0.30 E-02
3,541	2.00	46.	0.24 E+00	0.22 E-01	0.18 E-03

$r_{th} = 2.0 \times 10^{-3} \text{ m}$					
V (m/s)	Mach No.	Re	Pressure Force	Viscous Force	Lorentz Force
17.7	0.01	2.3	0.95 E+04	0.43 E+00	0.30 E+00
177	0.10	23	0.95 E+02	0.43 E-01	0.30 E-02
1,770	1.00	230	0.95 E+00	0.43 E-02	0.30 E-04
3,541	2.00	460	0.24 E+00	0.22 E-02	0.18 E-05

$$\frac{1}{\gamma_0 M_0^2} \Rightarrow \text{Pressure Force}$$

$$\frac{1}{Re} \Rightarrow \text{Viscous Force}$$

$$\frac{P_M}{\gamma_0 M_0^2} \Rightarrow \text{Lorentz Force}$$

$$\rho \frac{D\vec{v}}{Dt} = -\frac{1}{\gamma_0 M_0^2} \nabla P - \frac{1}{Re} \nabla \cdot \tau + \frac{P_M}{\gamma_0 M_0^2} \hat{j} \times \vec{B}$$

Table 2.2 **Energy Equation Order of Magnitude Analysis**
for $r_{th} = 2.0 \times 10^{-4} \text{ m}$

$r_{th} = 2.0 \times 10^{-4} \text{ m}$			
$V \text{ (m/s)}$	Thermal Conduction	Volume Changes	Viscous Dissipation
17.7	0.36 E+01	0.53 E-01	0.24 E-04
177	0.36 E+00	0.53 E-01	0.24 E-03
1,770	0.36 E-01	0.53 E-01	0.24 E-02
3,541	0.18 E-01	0.53 E-01	0.49 E-02
	Joulean Heating	Radiation	Electron Enthalpy
17.7	0.27 E+02	0.22 E-02	0.42 E+01
177	0.27 E+01	0.22 E-03	0.42 E+00
1,770	0.27 E+00	0.22 E-04	0.42 E-01
3,541	0.14 E+00	0.11 E-04	0.21 E-01

$$\frac{1}{Re \, Pr} \Rightarrow \text{Thermal Conduction}$$

$$\frac{\gamma_0 - 1}{\gamma_0} \Rightarrow \text{Volume Changes}$$

$$\frac{M_0^2 (\gamma_0 - 1)}{Re} \Rightarrow \text{Viscous Dissipation}$$

$$\frac{R_L}{Re \, Pr} \Rightarrow \text{Joulean Heating}$$

$$\frac{R_S}{Re \, Pr} \Rightarrow \text{Radiation}$$

$$\frac{R_C}{Re \, Pr} \Rightarrow \text{Electron Enthalpy}$$

$$\begin{aligned} \frac{\partial E_t}{\partial t} + \nabla \cdot E_t \vec{v} = & \frac{1}{Re \, Pr} \nabla \cdot (k \nabla T) - \frac{\gamma_0 - 1}{\gamma_0} \nabla \cdot p \vec{v} - \frac{M_0^2 (\gamma_0 - 1)}{Re} \nabla \cdot (\tau \cdot \vec{v}) \\ & + \frac{R_L}{Re \, Pr} \frac{j^2}{\sigma} - \frac{R_S}{Re \, Pr} S_R + \frac{5}{2} \frac{R_C}{Re \, Pr} \vec{j} \cdot \nabla T \end{aligned}$$

Table 2.3 **Energy Equation Order of Magnitude Analysis**
for $r_{th} = 2.0 \times 10^{-3} \text{ m}$

$r_{th} = 2.0 \times 10^{-3} \text{ m}$			
V (m/s)	Thermal Conduction	Volume Changes	Viscous Dissipation
17.7	0.36 E+00	0.53 E-01	0.24 E-05
177	0.36 E-01	0.53 E-01	0.24 E-04
1,770	0.36 E-02	0.53 E-01	0.24 E-03
3,541	0.18 E-02	0.53 E-01	0.49 E-03
	Joulean Heating	Radiation	Electron Enthalpy
17.7	0.27 E-01	0.22 E-01	0.42 E-01
177	0.27 E-02	0.22 E-02	0.42 E-02
1,770	0.27 E-03	0.22 E-03	0.42 E-03
3,541	0.14 E-03	0.11 E-03	0.21 E-03

$$\frac{1}{Re \, Pr} \Rightarrow \text{Thermal Conduction}$$

$$\frac{\gamma_0 - 1}{\gamma_0} \Rightarrow \text{Volume Changes}$$

$$\frac{M_0^2 (\gamma_0 - 1)}{Re} \Rightarrow \text{Viscous Dissipation}$$

$$\frac{R_L}{Re \, Pr} \Rightarrow \text{Joulean Heating}$$

$$\frac{R_S}{Re \, Pr} \Rightarrow \text{Radiation}$$

$$\frac{R_C}{Re \, Pr} \Rightarrow \text{Electron Enthalpy}$$

$$\begin{aligned} \frac{\partial E_t}{\partial t} + \nabla \cdot E_t \vec{v} = & \frac{1}{Re \, Pr} \nabla \cdot (k \nabla T) - \frac{\gamma_0 - 1}{\gamma_0} \nabla \cdot P \vec{v} - \frac{M_0^2 (\gamma_0 - 1)}{Re} \nabla \cdot (\tau \cdot \vec{v}) \\ & + \frac{R_L}{Re \, Pr} \frac{j^2}{\sigma} - \frac{R_S}{Re \, Pr} S_R + \frac{5}{2} \frac{R_C}{Re \, Pr} \vec{j} \cdot \nabla T \end{aligned}$$

Table 2.4 Ohm's Law Order of Magnitude Analysis

$r_{th} = 2.0 \times 10^{-4} \text{ m}$			
V (m/s)	Unsteady	Induced Field	Hall Effect
17.7	0.45 E-05	0.13 E-04	0.18 E+00
177	0.45 E-04	0.13 E-03	0.18 E+00
1,770	0.45 E-03	0.13 E-02	0.18 E+00
3,541	0.89 E-03	0.25 E-02	0.18 E+00

$r_{th} = 2.0 \times 10^{-3} \text{ m}$			
V (m/s)	Unsteady	Induced Field	Hall Effect
17.7	0.45 E-06	0.13 E-03	0.18 E-01
177	0.45 E-05	0.13 E-02	0.18 E-01
1,770	0.45 E-04	0.13 E-01	0.18 E-01
3,541	0.89 E-04	0.25 E-01	0.18 E-01

$R_F \Rightarrow$ Unsteady term

$R_{IN} \Rightarrow$ Induced field

$R_H \Rightarrow$ Hall Effect

$$R_F \frac{\sigma}{n_e} \frac{\partial \vec{j}}{\partial t} + \vec{j} = \sigma \vec{E} + R_{IN} \sigma \vec{v} \times \vec{B} - R_H \frac{\sigma}{n_e} \vec{j} \times \vec{B}$$

2.4 Non-dimensional Governing Equations

The preceding non-dimensional analysis was useful in demonstrating that the viscous dissipation term in the energy equation and the induced field and Hall effect terms in Ohm's Law can be neglected. In order to provide a consistent set of notation with which to compare the governing equations and results of this investigation to the work of other researchers, another group of non-dimensional parameters will be introduced.

The final set of non-dimensional parameters will be based on the dimensional inlet stagnation values of density, ρ_o , temperature, T_o , speed of sound, c_o , kinematic viscosity, μ_o , and the throat radius, r_{th} . The following non-dimensional quantities are defined, where the subscript "o" and the superscript " ^ " are as noted at the beginning of Section 2.3,

$$\begin{aligned}
 \widehat{\vec{v}} &= \vec{v} \cdot c_o & \widehat{\vec{B}} &= \vec{B} \cdot B_o & \widehat{\vec{E}} &= \vec{E} \cdot E_o \\
 \widehat{\vec{j}} &= \vec{j} \cdot \sigma_o E_o & \widehat{\rho} &= \rho \cdot \rho_o & \widehat{P} &= P \cdot (\rho_o \cdot c_o^2) \\
 \widehat{T} &= T \cdot T_o & \widehat{\sigma} &= \sigma \cdot \sigma_o & \widehat{k} &= k \cdot k_o \\
 \widehat{\mu} &= \mu \cdot \mu_o & \widehat{n_e} &= n_e \cdot n_{eo} & \widehat{c_p} &= c_p \cdot c_{po} \\
 \widehat{S_R} &= S_R \cdot S_{Ro} & \widehat{x_i} &= x_i \cdot r_{th} & \widehat{c_v} &= c_v \cdot c_{po} \\
 \widehat{\tau} &= \tau \cdot (\mu_o \cdot c_o / r_{th}) & \widehat{t} &= t \cdot (r_{th} / c_o) & \widehat{E_t} &= E_t \cdot (\rho_o \cdot c_o^2) \\
 \widehat{D/Dt} &= D/Dt \cdot c_o / r_{th} & \widehat{\nabla} &= \nabla / r_{th} & \widehat{e_t} &= e_t \cdot c_o^2
 \end{aligned}$$

The non-dimensional speed of sound, c , is

$$c^2 = \frac{\widehat{c^2}}{c_o^2} = \frac{\gamma \cdot \widehat{R} \cdot \widehat{T}}{\gamma_o \cdot \widehat{R} \cdot T_o} = \frac{\gamma}{\gamma_o} T = \gamma \frac{P}{\rho}$$

$$\text{where} \quad \gamma_o = \frac{c_{po}}{c_{vo}} \quad \text{and} \quad \gamma = \frac{\widehat{c_p}}{\widehat{c_v}} = \frac{c_p}{c_v}$$

The non-dimensional perfect gas relationship becomes

$$P = \frac{1}{\gamma_0} \rho T$$

with $c_p = \frac{\gamma R}{\gamma - 1}$ $c_v = \frac{R}{\gamma - 1}$

where $R = \frac{\hat{R}}{\hat{c}_{po}} = \frac{(\hat{R} / \text{M.W.})}{\hat{c}_{po}} = c_p - c_v$
 \hat{R} = universal gas constant
M.W. = Molecular weight

The non-dimensional total energy per unit volume is

$$E_t = \rho e_t = \rho \left(e_i + \frac{u^2 + v^2 + w^2}{2} \right)$$

where u, v, and w are the axial, radial, and circumferential velocity components, respectively, and e_i is the non-dimensional internal energy per unit mass given by

$$e_i = \frac{\hat{e}_i}{\hat{c}_0^2} = \frac{\hat{c}_v \hat{T}}{\hat{c}_0^2} = \frac{1}{(\gamma - 1) \gamma_0} T = \frac{1}{(\gamma - 1)} \frac{P}{\rho}$$

In addition, the pressure P can be expressed as

$$P = \rho (\gamma - 1) \left(e_t - \frac{u^2 + v^2 + w^2}{2} \right)$$

Only one non-dimensional parameter, the Reynolds number, must be redefined as

$$\text{Re} = \text{Reynolds number} = c_0 r_{th} \rho_0 / \mu_0 = \text{Inertia forces} / \text{viscous forces}$$

with the remaining non-dimensional parameters unchanged.

With the current non-dimensionalization the non-dimensional governing equations become

Continuity Eq $\frac{\partial \rho}{\partial t} + \nabla \cdot \rho \vec{v} = 0$ (2.29)

$$\text{Momentum Eq} \quad \rho \frac{D\vec{v}}{Dt} = -\nabla P - \frac{1}{Re} \nabla \cdot \tau + \frac{P_M}{\gamma_0} \hat{j} \times \vec{B} \quad (2.30)$$

Energy Eq

$$\begin{aligned} \frac{\partial E_t}{\partial t} + \nabla \cdot E_t \vec{v} = & \frac{1}{Re Pr (\gamma_0 - 1)} \nabla \cdot (k \nabla T) - \nabla \cdot P \vec{v} \\ + \frac{R_L}{Re Pr (\gamma_0 - 1)} \frac{j^2}{\sigma} - \frac{R_S}{Re Pr (\gamma_0 - 1)} S_R + \frac{5}{2} \frac{R_c}{Re Pr (\gamma_0 - 1)} \hat{j} \cdot \nabla T \end{aligned} \quad (2.31)$$

Generalized Ohm's Law

$$\hat{j} = \sigma \vec{E} \quad (2.32)$$

Induction Law

$$\nabla \times \vec{E} = 0 \quad (2.33)$$

Current Law

$$\nabla \times \vec{B} = \hat{j} \quad (2.34)$$

Equation of State

$$P = \frac{1}{\gamma_0} \rho T \quad (2.35)$$

Making the assumption the flow is axisymmetric ($\frac{\partial}{\partial \theta} = 0$) and representing the axial, radial, and circumferential or swirl velocity components as u , v , and w , respectively, we can write Eqs. (2.29-2.31) in vector form as:

$$\frac{\partial \vec{Q}}{\partial t} + \frac{\partial \vec{F}}{\partial z} + \frac{\partial \vec{G}}{\partial r} + \vec{H} = 0 \quad (2.36).$$

where the rows in the vectors \vec{Q} , \vec{F} , \vec{G} , \vec{H} contain the components of the continuity equation, axial, radial, and circumferential momentum equations, and the energy equation:

$$\vec{Q} = \begin{bmatrix} \rho \\ \rho u \\ \rho v \\ \rho w \\ E_t \end{bmatrix} \quad (2.37)$$

$$\vec{F} = \begin{bmatrix} \rho u \\ \rho u^2 + P + \frac{\tau_{zz}}{Re} \\ \rho uv + \frac{\tau_{rz}}{Re} \\ \rho uw + \frac{\tau_{\theta z}}{Re} \\ \left\{ E_t + P \right\} u - \frac{k}{Re Pr(\gamma_0 - 1)} \frac{\partial T}{\partial z} \end{bmatrix} \quad (2.38)$$

$$\vec{G} = \begin{bmatrix} \rho v \\ \rho uv + \frac{\tau_{rz}}{Re} \\ \rho v^2 + P + \frac{\tau_{rr}}{Re} \\ \rho vw + \frac{\tau_{\theta r}}{Re} \\ \left\{ E_t + P \right\} v - \frac{k}{Re Pr(\gamma_0 - 1)} \frac{\partial T}{\partial r} \end{bmatrix} \quad (2.39)$$

$$\vec{H'} = \left[\begin{array}{c} \frac{\rho v}{r} \\ \frac{\rho uv}{r} - \frac{P_M}{\gamma_0} j_r B_\theta + \frac{\tau_{rz}}{r \text{ Re}} \\ \frac{\rho v^2}{r} - \frac{\rho w^2}{r} + \frac{P_M}{\gamma_0} j_z B_\theta + \frac{\tau_{rr}}{r \text{ Re}} - \frac{\tau_{\theta\theta}}{r \text{ Re}} \\ \frac{2\rho vw}{r} + \frac{2\tau_{r\theta}}{r \text{ Re}} \\ \left(E_t + P \right) \frac{v}{r} - \frac{1}{r} \frac{1}{\text{Re Pr}(\gamma_0 - 1)} k \frac{\partial T}{\partial r} - \frac{R_L}{\text{Re Pr}(\gamma_0 - 1)} \frac{j^2}{\sigma} + \dots \\ \dots + \frac{R_S}{\text{Re Pr}(\gamma_0 - 1)} S_R - \frac{5}{2} \frac{R_C}{\text{Re Pr}(\gamma_0 - 1)} \left(j_r \frac{\partial T}{\partial r} + j_z \frac{\partial T}{\partial z} \right) \end{array} \right] \quad (2.40)$$

Lastly, the shear stress terms for an axisymmetric case [21] are:

$$\begin{aligned} \tau_{rr} &= -\mu \left(2 \frac{\partial v}{\partial r} - \frac{2}{3} \nabla \cdot \vec{v} \right) & \tau_{r\theta} &= -\mu \left(r \frac{\partial}{\partial r} \left(\frac{w}{r} \right) \right) \\ \tau_{\theta\theta} &= -\mu \left(2 \frac{v}{r} - \frac{2}{3} \nabla \cdot \vec{v} \right) & \tau_{\theta z} &= -\mu \left(\frac{\partial w}{\partial z} \right) \\ \tau_{zz} &= -\mu \left(2 \frac{\partial u}{\partial z} - \frac{2}{3} \nabla \cdot \vec{v} \right) & \tau_{rz} &= -\mu \left(\frac{\partial u}{\partial r} + \frac{\partial v}{\partial z} \right) \end{aligned} \quad (2.41)$$

where

$$\nabla \cdot \vec{v} = \frac{1}{r} \frac{\partial}{\partial r} (r v) + \frac{\partial u}{\partial z}$$

For the axisymmetric case, the components of the Current Law, Eq. (2.34), are:

$$\begin{aligned} j_r &= -\frac{\partial B_\theta}{\partial z} \\ j_\theta &= \frac{\partial B_r}{\partial z} - \frac{\partial B_z}{\partial r} \\ j_z &= -\frac{1}{r} \frac{\partial}{\partial r} (r B_\theta) . \end{aligned}$$

In addition, for the axisymmetric case B_r, B_z are identically equal to zero [10], so

$$\begin{aligned} j_r &= -\frac{\partial B_\theta}{\partial z} \\ j_\theta &= 0 \\ j_z &= -\frac{1}{r} \frac{\partial}{\partial r}(rB_\theta) . \end{aligned} \quad (2.42)$$

Using Eq. (2.42), the components of Ohm's Law, Eq. (2.30), become

$$\begin{aligned} j_r &= \sigma E_r \\ j_\theta &= E_\theta = 0 \\ j_z &= \sigma E_z . \end{aligned} \quad (2.43)$$

Using Eq. (2.43), the components of the Induction Law, Eq. (2.33), for the axisymmetric case become

$$\begin{aligned} (\nabla \times \vec{E})_r &= 0 \\ (\nabla \times \vec{E})_\theta &= \frac{\partial E_r}{\partial z} - \frac{\partial E_z}{\partial r} \\ (\nabla \times \vec{E})_z &= 0 \end{aligned} \quad (2.44)$$

Finally, Eqs. (2.42), (2.43), and (2.44) are combined to obtain the equation governing the electromagnetic field:

$$\frac{\partial}{\partial z} \left(\frac{1}{\sigma} \frac{\partial B_\theta}{\partial z} \right) + \frac{\partial}{\partial r} \left(\frac{1}{r\sigma} \frac{\partial}{\partial r}(rB_\theta) \right) = 0 \quad (2.45)$$

Thus, the governing fluid mechanics equations, Eq. (2.36) are uncoupled from the governing electromagnetic field equation, Eq. (2.45). The link between the two sets of equations is the electrical conductivity, σ , which is a strong function of pressure and temperature. Once the pressure and temperature distribution are known σ can be determined using tabular data, empirical models, etc. Given σ and appropriate boundary conditions for B_θ , Eq. (2.45) can be solved. The components of \vec{j} are then solved for using Eqs. (2.42)-(2.44). The source terms containing the components of \vec{j} and B_θ appearing in \vec{H} can then be calculated.

An iterative procedure is thus established between the fluid mechanics and the electromagnetic field portions of the flowfield. Both sets of governing equations are solved repeatedly until a steady-state solution is achieved.

2.5 Transformed Governing Equations

We will now consider the transformation from the physical domain (z,r) to the computational domain (ξ,η) where

$$\xi = \xi(z,r)$$

and

$$\eta = \eta(z,r)$$

Applying the chain rule of partial differentiation yields

$$\frac{\partial}{\partial z} = \frac{\partial \xi}{\partial z} \frac{\partial}{\partial \xi} + \frac{\partial \eta}{\partial z} \frac{\partial}{\partial \eta}$$

$$\frac{\partial}{\partial r} = \frac{\partial \xi}{\partial r} \frac{\partial}{\partial \xi} + \frac{\partial \eta}{\partial r} \frac{\partial}{\partial \eta}$$

Applying this transformation to the governing equations, Eqs. (2.36), (see Appendix B) yields

$$\frac{\partial \hat{Q}}{\partial t} + \frac{\partial \hat{F}'}{\partial \xi} + \frac{\partial \hat{G}'}{\partial \eta} + \hat{H}' = 0 \quad (2.46)$$

where the vectors $\hat{Q}, \hat{F}', \hat{G}', \hat{H}'$ are the $\vec{Q}, \vec{F}', \vec{G}', \vec{H}'$ vectors in the transformed coordinate system. Splitting the \hat{F}', \hat{G}' , and \hat{H}' vectors into inviscid ($\hat{F}, \hat{G}, \hat{H}$) and viscous ($\hat{F}_v, \hat{G}_v, \hat{H}_v$) components yields

$$\frac{\partial \hat{Q}}{\partial t} + \frac{\partial \hat{F}}{\partial \xi} + \frac{\partial \hat{F}_v}{\partial \xi} + \frac{\partial \hat{G}}{\partial \eta} + \frac{\partial \hat{G}_v}{\partial \eta} + \hat{H} + \hat{H}_v = 0 \quad (2.47)$$

An assumption has already been made the flow is axially symmetric, causing gradients of terms in the circumferential direction to be eliminated. However, the resulting axisymmetric Navier-Stokes equations do contain a circumferential or swirl velocity

component as well as axial and radial velocity components. These equations can be said to model a strongly swirling flow since only variations in the circumferential direction are neglected and all other terms are retained in the momentum equations.

In contrast, a weakly swirling axisymmetric flow can be adequately represented by applying the standard boundary layer approximations [12]

$$\begin{aligned} v_\theta, v_z &\approx O(1) \\ \frac{\partial}{\partial r} &\approx O\left(\frac{1}{\epsilon}\right) \text{ where } \epsilon \ll 1 \\ \frac{\partial}{\partial z} &\approx O(1) \end{aligned}$$

to the axisymmetric Navier-Stokes. However, the radial momentum equation, in the physical coordinate system, reduces to

$$\frac{\rho v_\theta^2}{r} = \frac{\partial P}{\partial r}$$

a balance between centripetal and pressure forces. In addition, all viscous terms in the momentum equations containing derivatives in the streamwise direction are found to be negligible. These are the governing equations used in [1, 10].

One of the aims of this study is to determine the effect of swirling flow on the current and velocity profiles. Obviously the radial momentum equation is simplified so immensely by a boundary layer assumption, no shear stress terms for example, that the effect of a large circumferential (or swirl, or tangential) velocity component cannot be adequately represented. Instead an assumption that the streamwise diffusion terms are small compared to the normal diffusion terms will be made, i.e.,

$$\frac{\partial}{\partial \eta} \gg \frac{\partial}{\partial \xi}$$

This is referred to as the Navier-Stokes thin layer approximation (TLA) [27]. Using this approximation only the viscous terms in the streamwise direction are eliminated and all other terms in the momentum equations are retained.

The resulting TLA equations contain more information about the flow than the boundary layer type equations which are valid only for weakly swirling flows. Thus, the TLA will be able to represent a stronger swirling flow than the boundary layer type equations yet only neglect the streamwise derivatives in the shear stress terms.

Applying the TLA to Eq. (2.47) yields

$$\frac{1}{J} \frac{\partial \vec{Q}}{\partial t} + \frac{\partial \hat{F}}{\partial \xi} + \frac{\partial \hat{G}}{\partial \eta} + \frac{\partial \hat{G}_v}{\partial \eta} + \hat{H} + \hat{H}_v = 0 \quad (2.48)$$

where the components of the vectors are

$$\vec{Q} = \begin{bmatrix} \rho \\ \rho u \\ \rho v \\ \rho w \\ E_t \end{bmatrix} \quad (2.49)$$

$$\hat{F} = d_A \begin{bmatrix} \rho u' \\ \rho u u' + \frac{1}{d_A} r_\eta P \\ \rho v u' + \frac{-1}{d_A} z_\eta P \\ \rho w u' \\ \{E_t + P\} u' \end{bmatrix} \quad (2.50)$$

$$\hat{G} = d_B \begin{bmatrix} \rho v' \\ \rho u v' + \frac{-1}{d_B} r_\xi P \\ \rho v v' + \frac{1}{d_B} z_\xi P \\ \rho w v' \\ \{E_t + P\} v' \end{bmatrix} \quad (2.51)$$

where u' and v' are the rotated velocity components normal to surfaces of constant ξ and η , respectively (see Appendix B).

$$\hat{F}_V = \frac{1}{Re} \begin{bmatrix} 0 \\ J(\beta_4 u_\eta + \beta_2 v_\eta) - \frac{2\mu}{3r} r_\xi v \\ J(\beta_2 u_\eta + \beta_1 v_\eta) + \frac{2\mu}{3r} z_\xi v \\ J\beta_3 w_\eta + \frac{\mu}{r} z_\xi w \\ \frac{J}{Re Pr(\gamma_0 - 1)} \beta_5 \frac{\partial T}{\partial \eta} \end{bmatrix} \quad (2.52)$$

where

$$\begin{aligned} \beta_1 &= -\mu \left(\frac{4}{3} z_\xi^2 + r_\xi^2 \right) & \beta_2 &= \frac{1}{3} \mu z_\xi r_\xi \\ \beta_3 &= -\mu (z_\xi^2 + r_\xi^2) & \beta_4 &= -\mu \left(z_\xi^2 + \frac{4}{3} r_\xi^2 \right) \\ \beta_5 &= -k (z_\xi^2 + r_\xi^2) \end{aligned}$$

$$\hat{H} = \frac{1}{J} \begin{bmatrix} \frac{\rho v}{r} \\ \frac{\rho uv}{r} \\ \frac{\rho v^2}{r} - \frac{\rho w^2}{r} \\ \frac{2}{r} \rho vw \\ \{E_t + P\} \frac{v}{r} \end{bmatrix} \quad (2.53)$$

$$\hat{H}_v = \begin{bmatrix} 0 \\ -\frac{P_M}{J \gamma_0} j_r B_\theta - \frac{\mu}{r Re} (z_\xi u_\eta - r_\xi v_\eta) \\ \frac{P_M}{J \gamma_0} j_z B_\theta + \frac{2\mu}{r Re} \left(\frac{v}{r} - z_\xi v_\eta \right) \\ \frac{2\mu}{r Re} \left(\frac{w}{r} - z_\xi w_\eta \right) \\ -\frac{k z_\xi T_\eta}{r Re Pr(\gamma_0 - 1)} - \frac{R_L}{J Re Pr(\gamma_0 - 1)} \frac{j^2}{\sigma} + \dots \\ \dots + \frac{R_S}{J Re Pr(\gamma_0 - 1)} S_R - \frac{5}{2} \frac{R_C}{Re Pr(\gamma_0 - 1)} (z_\xi j_r - r_\xi j_z) T_\eta \end{bmatrix} \quad (4)$$

Lastly, using the chain rule of partial differentiation the coordinate transformation is applied to the equation governing the electromagnetic field, Eq. (2.45) to yield

$$\begin{aligned} \eta_z \frac{\partial}{\partial \eta} \left(\frac{1}{\sigma} (\eta_z B_\eta + \xi_z B_\xi) \right) + \xi_z \frac{\partial}{\partial \xi} \left(\frac{1}{\sigma} (\eta_z B_\eta + \xi_z B_\xi) \right) \\ + \eta_r \frac{\partial}{\partial \eta} \left(\frac{1}{\sigma} (\eta_r B_\eta + \xi_r B_\xi + \frac{B}{r}) \right) + \xi_r \frac{\partial}{\partial \xi} \left(\frac{1}{\sigma} (\eta_r B_\eta + \xi_r B_\xi + \frac{B}{r}) \right) = 0 \end{aligned} \quad (2.55)$$

where

where $B_\eta \Rightarrow \frac{\partial B_\theta}{\partial \eta}$, etc.

The relationship between the Jacobian, J , metrics, $\xi_r, \xi_z, \eta_r, \eta_z$, and inverse metrics, $z_\eta, r_\eta, z_\xi, r_\xi$, of the coordinate transformation as well as details of the preceding derivation are contained in Appendix B.

Numerical Method

3.1 Introduction

This chapter discusses MacCormack's [20] implicit, flux-split, Gauss-Seidel line solver algorithm. The algorithm is used to solve the finite volume approximation to the governing fluid mechanics equations. The implicit and explicit forms of the inviscid, viscous, and source term portions of the governing equations are developed. The boundary conditions and procedures needed to model solid wall and centerline conditions are discussed and presented. An appropriate boundary condition procedure for a subsonic, swirling, viscous flow in an axisymmetric nozzle is also developed for the nozzle inlet plane.

3.2 Implicit Formulation

The flux-split finite volume approximation to the governing fluid mechanics equations in transformed coordinates (recalling Eq. (2.48))

$$\frac{1}{J} \frac{\partial \vec{Q}}{\partial t} + \frac{\partial \hat{F}}{\partial \xi} + \frac{\partial \hat{G}}{\partial \eta} + \frac{\partial \hat{G}_v}{\partial \eta} + \hat{H}' = 0 \quad (3.1)$$

will be developed now.

Since the inviscid flux vectors, \hat{F} , \hat{G} , are homogeneous functions of degree one [28] we can write

$$\hat{F} = \frac{\partial \hat{F}}{\partial \vec{Q}} \vec{Q} = A \vec{Q} \quad \text{and} \quad \hat{G} = \frac{\partial \hat{G}}{\partial \vec{Q}} \vec{Q} = B \vec{Q}$$

where A,B are the rotated Jacobian matrices of \hat{F} , \hat{G} and are derived in Appendix C. A consequence of this is that the inviscid flux vectors can be split into subvectors. One subvector is associated with all positive eigenvalues and the other with all negative eigenvalues. The subvectors are then differenced with an appropriate one-sided scheme.

The flux vectors are split after the Jacobians A, B have been diagonalized in the following manner, such that Λ_A and Λ_b are diagonal matrices composed of the eigenvalues

of A and B, respectively

$$A = S^{-1} R_A^{-1} C_A^{-1} \Lambda_A C_A R_A S$$

$$B = S^{-1} R_B^{-1} C_B^{-1} \Lambda_B C_B R_B S$$

where

$$\Lambda = \begin{bmatrix} \lambda_1 & & & & \\ & \lambda_2 & 0 & & \\ & & \lambda_3 & & \\ & 0 & & \lambda_4 & \\ & & & & \lambda_5 \end{bmatrix}$$

The matrices diagonalizing A and B, i.e., S, R, and C and the matrix of eigenvalues, Λ , are developed in Appendix C.

The individual eigenvalues are split by writing

$$\lambda_i = \lambda_i^+ + \lambda_i^-$$

where $\lambda_i^+ = \frac{\lambda_i + |\lambda_i|}{2}$ and $\lambda_i^- = \frac{\lambda_i - |\lambda_i|}{2}$

So that if

$$\lambda_i \geq 0, \quad \text{then} \quad \lambda_i^+ = \lambda_i \quad \text{and} \quad \lambda_i^- = 0$$

$$\lambda_i < 0, \quad \text{then} \quad \lambda_i^+ = 0 \quad \text{and} \quad \lambda_i^- = \lambda_i$$

Using these results we can write

$$\Lambda = \Lambda^+ + \Lambda^-$$

where the diagonal matrices Λ^+ and Λ^- contain the elements λ_i^+ and λ_i^- respectively. For subsonic flows, using the eigenvalues obtained in Appendix C, we have

$$\Lambda_A^+ = \text{diag}(d_A u', d_A u', d_A u', d_A(u' + c), 0)$$

$$\Lambda_A^- = \text{diag}(0, 0, 0, 0, d_A(u' - c))$$

and for supersonic flows

$$\Lambda_A^+ = \text{diag}(d_A u', d_A u', d_A u', d_A(u' + c), d_A(u' - c))$$

$$\Lambda_A^- = \text{diag}(0, 0, 0, 0, 0)$$

Finally, the flux vectors can be written

$$\begin{aligned}\hat{F} &= A \vec{Q} = S^{-1} R_A^{-1} C_A^{-1} \Lambda_A C_A R_A S \vec{Q} \\ &= S^{-1} R_A^{-1} C_A^{-1} (\Lambda_A^+ + \Lambda_A^-) C_A R_A S \vec{Q} \\ &= (A^+ + A^-) \vec{Q} \\ &= \hat{F}^+ + \hat{F}^-\end{aligned}$$

where

$$A^+ = S^{-1} R_A^{-1} C_A^{-1} \Lambda_A^+ C_A R_A S \quad A^- = S^{-1} R_A^{-1} C_A^{-1} \Lambda_A^- C_A R_A S$$

$$\hat{F}^+ = A^+ \vec{Q} \quad \hat{F}^- = A^- \vec{Q}$$

and

$$A = A^+ + A^-$$

The \hat{G} flux vector can be written in the same manner using the eigenvalues and matrices diagonalizing the B matrix.

The finite volume approximation to Eq. (3.1) can now be developed. Implicitly differencing the equation using first order accurate differences in space and time yields

$$\frac{\vec{Q}^{n+1} - \vec{Q}^n}{J} + \Delta t \left[\frac{D \hat{F}^{n+1}}{\Delta \xi} + \frac{D \hat{G}^{n+1}}{\Delta \eta} + \frac{D \hat{G}_v^{n+1}}{\Delta \eta} \right] + \hat{H}^{n+1} = 0 \quad (3.2)$$

The direction of the difference operators, D, will be discussed as each term is examined.

3.2.1 Implicit Formulation- Inviscid Flux Vectors

The finite difference representation of $\frac{D \hat{F}^{n+1}}{\Delta \xi}$ (and similarly of $\frac{D \hat{G}^{n+1}}{\Delta \eta}$) will be derived by central differencing the expression such that

$$\frac{D \hat{F}^{n+1}}{\Delta \xi} = \frac{\hat{F}_{i+1/2,j}^{n+1} - \hat{F}_{i-1/2,j}^{n+1}}{\Delta \xi} \quad (3.3)$$

Thus the flux in the ξ direction crossing the surface of a control volume located at (i,j)

enters and leaves through the surfaces located at $(i \pm 1/2, j)$. This is illustrated in Fig. 3.1.

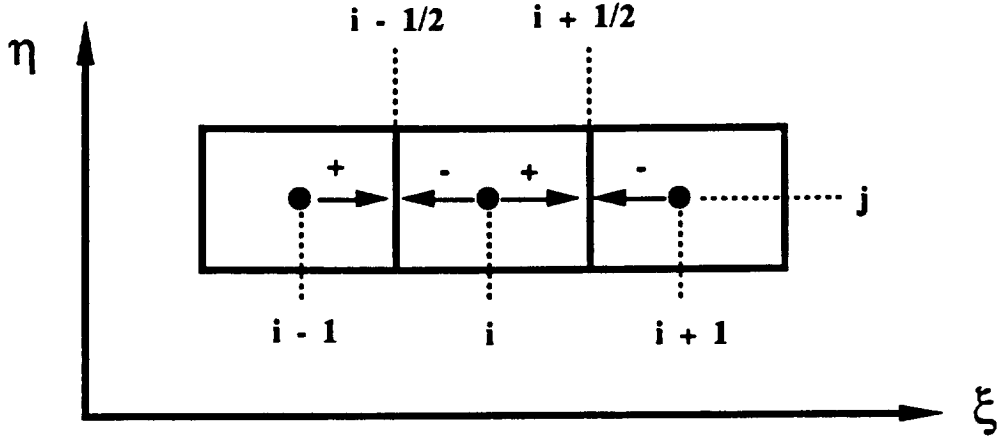


Figure 3.1 Direction of streamwise flux travel

The flux crossing the surface located at $(i + 1/2, j)$ in the positive ξ direction originates at i, j and the flux traveling in the negative ξ direction originates at $(i + 1, j)$. Accordingly, the inviscid flux across the surface located at $(i + 1/2, j)$ is

$$\hat{F}_{i+1/2,j}^n = A_{i+1/2,j}^{+n} \bar{Q}_{i,j}^n + A_{i+1/2,j}^{-n} \bar{Q}_{i+1,j}^n \quad (3.4)$$

whereas the flux crossing the surface located at $(i - 1/2, j)$ is

$$\hat{F}_{i-1/2,j}^n = A_{i-1/2,j}^{-n} \bar{Q}_{i,j}^n + A_{i-1/2,j}^{+n} \bar{Q}_{i-1,j}^n \quad (3.5)$$

Note that the Jacobian coefficient matrices are evaluated at the cell edge. Clearly, the net flux crossing the surface of a control volume is proportional to the difference between Eqs. (3.4) and (3.5), however, the grid point at which each A^n is evaluated is not explicit because only information at the cell center is available, not at the surface of the control volume where the Jacobians need to be evaluated. A method to resolve this ambiguity was proposed by Steger and Warming [28]. For a flux traveling in the positive ξ direction the Jacobian is evaluated at the point upstream of the surface and for a flux traveling in the negative ξ direction the Jacobian is evaluated at the point downstream of the surface. Thus, the Jacobians would be evaluated at

$$\begin{aligned} A_{i+1/2,j}^{+n} &\rightarrow A_{i,j}^{+n} & A_{i+1/2,j}^{-n} &\rightarrow A_{i+1,j}^{-n} \\ A_{i-1/2,j}^{-n} &\rightarrow A_{i,j}^{-n} & A_{i-1/2,j}^{+n} &\rightarrow A_{i-1,j}^{+n} \end{aligned}$$

An alternate method has been proposed by MacCormack [20] and discussed in more detail by Candler in [29]. In this method both Jacobians, A^{-n} and A^{+n} , are always evaluated at the same point. The point chosen alternates the half integer indices $i+1/2$ ($i-1/2$) between i and $i+1$ ($i-1$ and i). Equivalently the half integer points at $i + 1/2$ ($i - 1/2$) can be evaluated using the average of the flow variables from the points i and $i+1$ (i and $i-1$).

MacCormack and Candler [30] demonstrated the Steger-Warming form of flux splitting results in excessive numerical diffusion in the boundary layer while the MacCormack flux split procedure prevented excessive numerical diffusion. Flows containing shocks must be evaluated with a different procedure [31]. The MacCormack procedure, evaluating the half integer points using the average of the flow variables, was used in the present study.

The inviscid flux vectors are made second order accurate [32,33] by linearly extrapolating the value of \vec{Q}^n . Thus the value of value of \vec{Q}^n approaching the $i+1/2$ surface from the upstream (downstream) direction is $3/2\vec{Q}_{i,j}^n - 1/2\vec{Q}_{i-1,j}^n$ ($3/2\vec{Q}_{i+1,j}^n - 1/2\vec{Q}_{i+2,j}^n$). Pressure switches are used to degrade the accuracy to first order in regions of large pressure gradient. For example Eq. (3.4) becomes

$$\begin{aligned}\hat{F}_{i+1/2,j}^n = & A_{i+1/2,j}^{+n} \left(\vec{Q}_{i,j}^n + SW_{i-1/2,j} \left(\vec{Q}_{i,j}^n - \vec{Q}_{i-1,j}^n \right) \right) \\ & + A_{i+1/2,j}^{-n} \left(\vec{Q}_{i+1,j}^n + SW_{i+3/2,j} \left(\vec{Q}_{i+1,j}^n - \vec{Q}_{i+2,j}^n \right) \right)\end{aligned}$$

with

$$SW_{i+3/2,j} = \text{Max} \left\{ 0.0, 0.5 - \frac{|P_{i+2} - P_{i+1}|}{\text{Min}(P_{i+2}, P_{i+1})} \right\}$$

By evaluating A at time level n the inviscid flux can be linearized to yield

$$\hat{F}^{n+1} = \hat{F}^n + A^n \left(\vec{Q}^{n+1} - \vec{Q}^n \right) + O(\Delta t^2) \quad (3.6)$$

In summary, the ξ directed inviscid flux at time level $n+1$ crossing the surface $(i+1/2, j)$ is approximated using Eqs. (3.4) and (3.6) as

$$\begin{aligned}\hat{F}_{i+1/2,j}^{n+1} = & A_{i+1/2,j}^{+n} \vec{Q}_{i,j}^{n+1} + A_{i+1/2,j}^{-n} \vec{Q}_{i+1,j}^{n+1} \\ = & A_{i+1/2,j}^{+n} \vec{Q}_{i,j}^n + A_{i+1/2,j}^{-n} \vec{Q}_{i+1,j}^n + A_{i+1/2,j}^{+n} \delta \vec{Q}_{i,j}^n + A_{i+1/2,j}^{-n} \delta \vec{Q}_{i+1,j}^n\end{aligned} \quad (3.7)$$

where

$$\delta \vec{Q}^n \equiv \vec{Q}_{i,j}^{n+1} - \vec{Q}_{i,j}^n = \Delta t \frac{\partial \vec{Q}}{\partial t}$$

Similarly the flux crossing the $(i-1/2, j)$ surface is expressed as

$$\hat{F}_{i-1/2,j}^{n+1} = A_{i-1/2,j}^{\cdot n} \bar{Q}_{i,j}^n + A_{i-1/2,j}^{+n} \bar{Q}_{i-1,j}^n + A_{i-1/2,j}^{\cdot n} \delta \bar{Q}_{i,j}^n + A_{i-1/2,j}^{+n} \delta \bar{Q}_{i-1,j}^n \quad (3.8)$$

Finally substituting Eqs. (3.7) and (3.8) into (3.3) and gathering terms yields

$$\frac{D \hat{F}^{n+1}}{\Delta \xi} = \frac{1}{\Delta \xi} \left\{ [D_- A_{i+1/2,j}^{\cdot n} + D_+ A_{i-1/2,j}^{\cdot n}] (\delta \bar{Q}_{i,j}^n + \bar{Q}_{i,j}^n) \right\} \quad (3.9)$$

where D_- and D_+ are backwards and forward difference operators, respectively. Similarly in the η direction we have

$$\frac{D \hat{G}^{n+1}}{\Delta \eta} = \frac{1}{\Delta \eta} \left\{ [D_- B_{i,j+1/2}^{\cdot n} + D_+ B_{i,j-1/2}^{\cdot n}] (\delta \bar{Q}_{i,j}^n + \bar{Q}_{i,j}^n) \right\} \quad (3.10)$$

3.2.2 Implicit Formulation- Viscous Flux Vector

The finite difference representation of $\frac{D \hat{G}_v^{n+1}}{\Delta \eta}$ will be expressed at time level n by defining

$$\hat{G}_v^{n+1} = \hat{G}_v^n + \delta \hat{G}_v^n$$

\hat{G}_v can be partitioned into: 1) the terms common to both the cartesian and cylindrical formulations and 2) the additional terms arising from the cylindrical axisymmetric formulation

$$\hat{G}_v = \hat{G}_{vcom} + \hat{G}_{vcyl}$$

where

$$\hat{G}_{vcom} = \frac{1}{Re} \begin{bmatrix} 0 \\ J(\beta_4 u_\eta + \beta_2 v_\eta) \\ J(\beta_2 u_\eta + \beta_1 v_\eta) \\ J \beta_3 w_\eta \\ \frac{J}{Re Pr (\gamma_0 - 1)} \beta_5 \frac{\partial T}{\partial \eta} \end{bmatrix} \quad \hat{G}_{vcyl} = \frac{1}{Re} \begin{bmatrix} 0 \\ -\frac{2\mu}{3r} r_\xi v \\ \frac{2\mu}{3r} z_\xi v \\ \frac{\mu}{r} z_\xi w \\ 0 \end{bmatrix}$$

By employing the vector of primitive variables, \vec{V}

$$\vec{V} = (\rho \ u \ v \ w \ T)^T$$

we can write

$$\begin{aligned} \delta \hat{G}_v &= \delta \hat{G}_{vcom} + \delta \hat{G}_{vcyl} \\ &= M_a \frac{\partial}{\partial \eta} \delta \vec{V} + M_b \delta \vec{Q} \end{aligned}$$

where

$$\delta \vec{V} = (\delta \rho \ \delta u \ \delta v \ \delta w \ \delta T)^T$$

Matrices M_a and M_b are given in Appendix D. We can change variables from $\delta \vec{V}$ to $\delta \vec{Q}$ by defining the Jacobian N where $N = \frac{\partial \vec{V}}{\partial \vec{Q}}$ such that $\delta \vec{V} = N \delta \vec{Q}$. This yields

$$\delta \hat{G}_v = M_a \frac{\partial N \delta \vec{Q}}{\partial \eta} + M_b \delta \vec{Q}$$

Matrix N is also given in Appendix D.

Thus the viscous flux in the η direction becomes

$$\begin{aligned} \frac{D \hat{G}_v^{n+1}}{\Delta \eta} &= \frac{D}{\Delta \eta} \left(\hat{G}_v^n + M_a \frac{D N \delta \vec{Q}}{\Delta \eta} + M_b \delta \vec{Q} \right) \\ &= \frac{D}{\Delta \eta} \hat{G}_{vi,j}^n + \frac{D}{\Delta \eta} \left(M_{ai,j+1/2} \frac{D_+ N \delta \vec{Q}_{i,j}}{\Delta \eta} \right) + \frac{D}{\Delta \eta} (M_{bi,j} \delta \vec{Q}_{i,j}) \end{aligned} \quad (3.11)$$

The middle and final terms in Eq. (3.11) are central differenced [34] with the final term expressed as

$$\begin{aligned} \frac{D}{\Delta \eta} (M_b \delta \vec{Q})_{i,j} &= [(M_b \delta \vec{Q})_{i,j+1/2} - (M_b \delta \vec{Q})_{i,j-1/2}] / \Delta \eta \\ &= [M_{bi,j+1/2} (\delta \vec{Q}_{i,j+1} + \delta \vec{Q}_{i,j}) / 2 + M_{bi,j-1/2} (\delta \vec{Q}_{i,j} + \delta \vec{Q}_{i,j-1}) / 2] / \Delta \eta \end{aligned}$$

In other works, [29,30], the Thin Layer Approximation (TLA, see Section 2.5) was also applied during the formulation of the implicit algorithm. Consequently, these formulations also neglect the viscous flux in the ξ direction in the implicit portion of the

formulation. However, the viscous derivatives in the ξ direction could be retained in the explicit portion of the formulation, thus influencing the converged solution [20].

If the ξ direction viscous terms, $\frac{\partial \hat{F}_v}{\partial \xi}$, were retained they would be approximated as the \hat{G}_v term was

$$\frac{\partial \hat{F}_v}{\partial \xi} \equiv \frac{D \hat{F}_v^{n+1}}{\Delta \xi} = \frac{D}{\Delta \xi} (\hat{F}_v^n + \delta \hat{F}_v^n)$$

The TLA is now applied to the both the explicit and implicit derivatives, the implication being that gradients of the viscous terms are much larger in the η direction than in the ξ direction

$$\frac{D}{\Delta \eta} (\hat{G}_v^n + \delta \hat{G}_v^n) \gg \frac{D}{\Delta \xi} (\hat{F}_v^n + \delta \hat{F}_v^n)$$

resulting in

$$\frac{D}{\Delta \xi} (\hat{F}_v^n + \delta \hat{F}_v^n) \equiv 0 \quad (3.12)$$

3.2.3 Implicit Formulation- Source Term

The source term can be split into inviscid and "viscous" portions. The inviscid portion of the source term is due to the additional convection terms that arise due to the axisymmetric geometry. The "viscous" portion of the source term contains terms arising from the shear stress terms in an axisymmetric geometry as well as terms due to the current flow and radiation. Consequently, the source term can be linearized, as the inviscid flux terms were, to be

$$\begin{aligned} \hat{H}_{i,j}^{n+1} &= \hat{H}_{i,j}^n + \delta \hat{H}_{i,j}^n \\ &= \hat{H}_{i,j}^n + \hat{H}_{v,i,j}^n + \delta \hat{H}_{i,j}^n + \delta \hat{H}_{v,i,j}^n \end{aligned}$$

The viscous source terms will be neglected in the implicit side of the formulation, $\delta \hat{H}_{v,i,j} = 0$, but will be retained in the explicit portion of the formulation, i.e., $\hat{H}_{v,i,j} \neq 0$. Hence, the physics of the flow will be retained in the explicit portion of the solution (all terms are retained in the explicit source term) and therefore influence the converged solution. Finally, using these assumptions the source term can be written as

$$\hat{H}_{i,j}^{n+1} = \hat{H}_{i,j}^n + C_{i,j} \delta \hat{Q}_{i,j}^n \quad (3.13)$$

where

$$\widehat{H}_{i,j}^n = (\widehat{H} + \widehat{H}_v)_{i,j}^n \quad \text{and} \quad C_{li,j} = \frac{\partial \widehat{H}}{\partial \bar{Q}}$$

The matrix $C_{li,j}$ can be found in Appendix D.

3.2.4 Implicit Formulation- Finite Volume Approximation

Substituting Eqs. (3.9)-(3.13) into Eq. (3.2), yields the finite volume difference equation approximating the governing equations

$$\left\{ I + \frac{\Delta t}{V_{ij}} \left[\frac{D_-}{\Delta \xi} A_{i+1/2,j}^{+n} + \frac{D_+}{\Delta \xi} A_{i-1/2,j}^{-n} + \frac{D_-}{\Delta \eta} B_{i,j+1/2}^{+n} + \frac{D_+}{\Delta \eta} B_{i,j-1/2}^{-n} \right. \right. \\ \left. \left. + \frac{D_-}{\Delta \eta} \left(M_{ai,j+1/2}^n \frac{D_+}{\Delta \eta} N_{i,j}^n \right) + \frac{D_-}{\Delta \eta} M_{bi,j}^n + C_{li,j}^n \right] \right\} \delta \bar{Q}_{i,j}^n = \Delta \bar{Q}_{i,j}^n \quad (3.14)$$

where

$$V_{ij} = \text{cell volume} = 1/J$$

$$\Delta \bar{Q}_{i,j}^n = - \frac{\Delta t}{V_{ij}} \left[\frac{D_-}{\Delta \xi} A_{i+1/2,j}^{+n} + \frac{D_+}{\Delta \xi} A_{i-1/2,j}^{-n} + \frac{D_-}{\Delta \eta} B_{i,j+1/2}^{+n} + \frac{D_+}{\Delta \eta} B_{i,j-1/2}^{-n} \right] \bar{Q}_{i,j}^n \\ - \frac{\Delta t}{V_{ij}} \left[\frac{D_-}{\Delta \eta} \widehat{G}_{vi,j}^n + \widehat{H}_{i,j}^n + \widehat{H}_{vi,j}^n \right]$$

In the present work the grid point spacing in the computational plane is uniform yielding $\Delta \xi = \Delta \eta = 1$. Finally, Eq. (3.14) can be written in a form used in the Gauss-Seidel procedure as

$$\tilde{B}_{i,j} \delta \bar{Q}_{i,j+1}^n + \tilde{A}_{i,j} \delta \bar{Q}_{i,j}^n + \tilde{C}_{i,j} \delta \bar{Q}_{i,j-1}^n = \text{RHS}_{i,j} \quad (3.15)$$

where

$$\tilde{B}_{i,j} = \frac{\Delta t}{V_{ij}} \left(B_{i,j+1/2}^{-n} + M_{ai,j+1/2}^n N_{i,j+1}^n + \frac{M_{bi,j+1/2}^n}{2} \right)$$

$$\begin{aligned}\tilde{A}_{ij} = & I + \frac{\Delta t}{V_{ij}} (A_{i+1/2,j}^{+n} - A_{i-1/2,j}^n) + \frac{\Delta t}{V_{ij}} (B_{i,j+1/2}^{+n} - B_{i,j-1/2}^n) \\ & - \frac{\Delta t}{V_{ij}} \left(M_{ai,j+1/2}^n N_{i,j}^n + M_{ai,j-1/2}^n N_{i,j}^n - \left(\frac{M_{bi,j+1/2}^n \cdot M_{bi,j-1/2}^n}{2} \right) \right) + \frac{\Delta t}{V_{ij}} C_{ii,j}^n\end{aligned}$$

$$\tilde{C}_{ij} = \frac{\Delta t}{V_{ij}} \left(-B_{i,j-1/2}^{+n} + M_{ai,j-1/2}^n N_{i,j-1}^n - \frac{M_{bi,j-1/2}^n}{2} \right)$$

$$RHS_{ij} = -\tilde{D}_{ij} \delta \tilde{Q}_{i+1,j}^n - \tilde{E}_{ij} \delta \tilde{Q}_{i-1,j}^n + \Delta \tilde{Q}_{i,j}^n$$

$$\tilde{D}_{ij} = \frac{\Delta t}{V_{ij}} A_{i+1/2,j}^{+n} \quad \tilde{E}_{ij} = -\frac{\Delta t}{V_{ij}} A_{i-1/2,j}^{+n}$$

3.3 Boundary Conditions

The block-tridiagonal set of equations given in Eq. (3.15) can be written in matrix form as

$$\begin{bmatrix} \tilde{B}_{JMAX-1} & \tilde{A}_{JMAX-1} & \tilde{C}_{JMAX-1} & & & \\ & \ddots & \ddots & \ddots & & \\ & & \tilde{B}_j & \tilde{A}_j & \tilde{C}_j & \\ & & & \ddots & \ddots & \ddots \\ & & & \tilde{B}_2 & \tilde{A}_2 & \tilde{C}_2 \end{bmatrix}_i \begin{bmatrix} \delta \tilde{Q}_{JMAX} \\ \delta \tilde{Q}_{JMAX-1} \\ \vdots \\ \delta \tilde{Q}_j \\ \vdots \\ \delta \tilde{Q}_2 \\ \delta \tilde{Q}_1 \end{bmatrix}_i = \begin{bmatrix} RHS_{JMAX} \\ RHS_{JMAX-1} \\ \vdots \\ RHS_j \\ \vdots \\ RHS_3 \\ RHS_2 \end{bmatrix}_i$$

(3.16)

Boundary conditions representing a solid wall or centerline symmetry conditions on the upper and lower boundaries are imposed through the $j=2$ and $JMAX-1$ rows of the block matrices shown above. The appropriate inviscid and viscous boundary conditions are implemented differently in the explicit and implicit portions of the block matrices and will be discussed separately.

The boundary conditions imposed at the inlet and outlet planes of the thruster, $i=2$ and $i=IMAX-1$ respectively, are implemented using a Method of Characteristics (MOC) procedure and are also discussed subsequently.

3.3.1 Boundary Conditions- Upper and Lower Boundaries

Several different methods could be used to implement the boundary conditions on the upper and lower boundaries. One method is to use a fictitious element outside of the computational domain. The wall volume element common to the interior elements and the fictitious elements represents the physical boundary of the object being modeled, e.g. nozzle wall, centerline, etc. Using the boundary conditions and flow information from the interior elements the flow conditions in the fictitious elements can be set to yield the proper boundary conditions, e.g., no-slip along a solid wall. The flux crossing the surface is calculated in the same manner as for all other cells. The resulting flux should represent the desired boundary conditions.

Another method, implemented in the present work, calculates the flux by directly applying the boundary conditions to the affected fluxes, e.g., no normal flow across a surface representing a solid wall or centerline. Thus, fictitious elements are not used. However, to allow for the possibility of investigating several methods of applying boundary conditions the notation used in this study also allows fictitious boundary elements. The subscripts i,j represent a cell located at the i th element in the streamwise and the j th element in the cross-stream direction. Therefore, the fictitious elements not used in the present study are elements located at: $(i=1 \Rightarrow IMAX, j=1)$, $(i=1 \Rightarrow IMAX, j=JMAX)$, $(i=1, j=1 \Rightarrow JMAX)$, $(i=IMAX, j=1 \Rightarrow JMAX)$. Thus, in a grid described as 60×40 , $IMAX=60$, $JMAX=40$, and the computational domain actually contains 58×38 elements.

3.3.1.1 Upper and Lower Boundary- Explicit Boundary Conditions

The explicit inviscid boundary conditions across a surface of $\eta = \text{cst}$ will be examined first. There is no flux of mass, momentum, or energy across a surface representing an impermeable wall or centerline and the normal velocity to the surface is zero. These boundary conditions are expressed in the explicit inviscid flux vector as (which is obtained by setting $v' = 0$ in \hat{G})

$$\hat{G} = \begin{bmatrix} 0 & -r_{\xi}P & z_{\xi}P & 0 & 0 \end{bmatrix}^T \quad (3.17)$$

The explicit viscous flux boundary conditions are set by the following conditions along the lower and upper boundaries

$$\begin{aligned}
u'_{i,1} &= \begin{cases} + u'_{i,2} & \text{centerline symmetry} \\ - u'_{i,2} & \text{solid wall, no slip} \end{cases} \\
v'_{i,1} &= \begin{cases} + v'_{i,2} & \text{centerline symmetry} \\ - v'_{i,2} & \text{solid wall, no slip} \end{cases} \\
w_{i,1} &= \begin{cases} + w_{i,2} & \text{centerline symmetry} \\ - w_{i,2} & \text{solid wall, no slip} \end{cases} \\
T_{i,1} &= \begin{cases} T_{i,2} & \text{adiabatic wall/centerline symmetry} \\ 2 T_{i,\text{wall}} - T_{i,2} & \text{isothermal or prescribed wall temperature} \end{cases}
\end{aligned} \tag{3.18}$$

Centerline symmetry velocity conditions state the axial, radial and swirl velocity components of the two volume elements on either side of the centerline have the same magnitude and direction. An adiabatic wall condition is expressed by a temperature equality. There will be no heat transfer across the surface if the temperatures of the two cells adjacent to the boundary have the same temperature. The isothermal or prescribed wall temperature condition is derived using an arithmetic average of the temperatures of the two volume elements adjacent to the wall, $T_{i,\text{wall}} = (T_{i,1} + T_{i,2}) / 2$.

For example, the explicit inviscid and viscous boundary conditions for the lower surface are implemented through the term $\text{RHS}_{i,2}$, where

$$\text{RHS}_{i,2} = - \tilde{D}_{i,2} \delta \tilde{Q}_{i+1,2} - \tilde{E}_{i,2} \delta \tilde{Q}_{i-1,2} + \Delta \tilde{Q}_{i,2}$$

by modifying the terms contained in the explicit term $\Delta \tilde{Q}_{i,2}$

$$\begin{aligned}
\Delta \tilde{Q}_{i,2} &= - \Delta t \left[\frac{D_-}{\Delta \xi} A_{i+1/2,2}^+ + \frac{D_+}{\Delta \xi} A_{i-1/2,2}^- + \frac{D_-}{\Delta \eta} B_{i,2+1/2}^+ + \frac{D_+}{\Delta \eta} B_{i,1+1/2}^- \right] \tilde{Q}_{i,2} \\
&\quad - \Delta t \left[\frac{D}{\Delta \eta} \hat{G}_{vi,2} + \hat{H}_{i,2} \right]
\end{aligned} \tag{3.19}$$

Explicit Inviscid Boundary Conditions

The explicit inviscid boundary conditions given by Eq. (3.17) are implemented by modifying the inviscid terms at the lower boundary, in the η direction, in Eq. (3.19) given by

$$\begin{aligned} & \left(\frac{D_-}{\Delta\eta} B_{i,2+1/2}^+ + \frac{D_+}{\Delta\eta} B_{i,1+1/2}^- \right) \tilde{Q}_{i,2} \\ &= \left(B_{i,2+1/2}^+ \tilde{Q}_{i,2} + B_{i,2+1/2}^- \tilde{Q}_{i,3} \right) - \left(B_{i,1+1/2}^+ \tilde{Q}_{i,1} + B_{i,1+1/2}^- \tilde{Q}_{i,2} \right) \end{aligned}$$

The second bracketed term in the last expression represents the flux crossing the surface located at $j = 1 + 1/2$. Using Eq. (3.17) the resulting flux is

$$\left(B_{i,1+1/2}^+ \tilde{Q}_{i,1} + B_{i,1+1/2}^- \tilde{Q}_{i,2} \right) = \hat{G}_{i,1+1/2}^* = \begin{bmatrix} 0 & -r_\xi P_{i,2} & z_\xi P_{i,2} & 0 & 0 \end{bmatrix}^T$$

and the metrics are evaluated at the surface $j = 1 + 1/2$. If the surface is a centerline, the metric r_ξ will equal zero.

Thus the explicit inviscid flux terms in the η direction at $j=2$ become

$$\begin{aligned} & \left(\frac{D_-}{\Delta\eta} B_{i,2+1/2}^+ + \frac{D_+}{\Delta\eta} B_{i,1+1/2}^- \right) \tilde{Q}_{i,2} \\ &= \left(B_{i,2+1/2}^+ \tilde{Q}_{i,2} + B_{i,2+1/2}^- \tilde{Q}_{i,3} \right) - \left(\hat{G}_{i,1+1/2}^* \right) \end{aligned}$$

Following an analogous procedure the explicit inviscid flux at the upper boundary is set by modifying the inviscid flux terms at $j=JMAX-1$

$$\begin{aligned} & \left(\frac{D_-}{\Delta\eta} B_{i,JMAX-1/2}^+ + \frac{D_+}{\Delta\eta} B_{i,JMAX-3/2}^- \right) \tilde{Q}_{i,JMAX-1} \\ &= \left(B_{i,JMAX-1/2}^+ \tilde{Q}_{i,JMAX-1} + B_{i,JMAX-1/2}^- \tilde{Q}_{i,JMAX} \right) \\ &\quad - \left(B_{i,JMAX-3/2}^+ \tilde{Q}_{i,JMAX-2} + B_{i,JMAX-3/2}^- \tilde{Q}_{i,JMAX-1} \right) \end{aligned}$$

The first bracketed term in the above expression represents the flux crossing the $j=JMAX-1/2$ surface. Using Eq. (3.17) the explicit inviscid flux terms in the η direction at

$j=JMAX-1$ become

$$\begin{aligned} & \left(\frac{D_-}{\Delta\eta} B_{i,JMAX-1/2}^+ + \frac{D_+}{\Delta\eta} B_{i,JMAX-3/2}^- \right) \tilde{Q}_{i,JMAX-1} \\ &= \left(\hat{G}_{i,JMAX-1/2}^* \right) - \left(B_{i,JMAX-3/2}^+ \tilde{Q}_{i,JMAX-2} + B_{i,JMAX-3/2}^- \tilde{Q}_{i,JMAX-1} \right) \end{aligned}$$

where

$$\hat{G}_{i,JMAX-1/2}^* = \begin{bmatrix} 0 & -r_\xi P_{i,JMAX-1} & z_\xi P_{i,JMAX-1} & 0 & 0 \end{bmatrix}^T$$

and the metrics are evaluated at the surface $j=JMAX-1/2$.

Explicit Viscous Boundary Conditions

The explicit viscous boundary conditions given by Eq. (3.18) are implemented by modifying the viscous terms at the lower boundary, in the η direction, in Eq. (3.19) given by

$$\begin{aligned} \frac{D}{\Delta\eta} \hat{G}_{vi,2} &= \frac{D_-}{\Delta\eta} \left(M_{ai,2+1/2} \frac{D_+}{\Delta\eta} \tilde{V}_{i,2} \right) + \frac{D}{\Delta\eta} \left(\hat{G}_{vcyl} \right)_{i,2} \\ &= \left\{ M_{ai,2+1/2} (\tilde{V}_{i,3} - \tilde{V}_{i,2}) - M_{ai,1+1/2} (\tilde{V}_{i,2} - \tilde{V}_{i,1}) \right\} \\ &\quad + \left\{ \hat{G}_{vcyl\ i,2+1/2} - \hat{G}_{vcyl\ i,1+1/2} \right\} \end{aligned} \quad (3.20)$$

where

$$\tilde{V} = \begin{bmatrix} \rho \\ u \\ v \\ w \\ T \end{bmatrix} \quad \hat{G}_{vcyl} = \frac{\mu}{r Re} \begin{bmatrix} 0 \\ -\frac{2}{3} r_\xi v \\ \frac{2}{3} z_\xi v \\ z_\xi w \\ 0 \end{bmatrix}$$

The explicit viscous boundary conditions are implemented by modifying the two bracketed expressions in Eq. (3.20). The first bracketed expression contains the terms common to either a cartesian or cylindrical coordinate formulation and will be modified first.

Consider the boundary conditions for the lower surface located at $j = 1 + 1/2$. The second term in the first bracketed expression in Eq. (3.20) is

$$M_{ai,1+1/2} (\vec{V}_{i,2} - \vec{V}_{i,1}) = M_{ai,1+1/2} \begin{bmatrix} \rho_2 - \rho_1 \\ u_2 - u_1 \\ v_2 - v_1 \\ w_2 - w_1 \\ T_2 - T_1 \end{bmatrix}$$

Using the explicit viscous boundary conditions given in Eq. (3.18) this expression can be written as

$$M_{ai,1+1/2} (\vec{V}_{i,2} - \vec{V}_{i,1}) = M_{ai,1+1/2} \begin{bmatrix} \rho_2 - \rho_1 \\ t_u u_2 \\ t_u v_2 \\ t_u w_2 \\ t_T T_2 \end{bmatrix}$$

where

$$t_u = \begin{cases} 0 & \text{centerline symmetry} \\ 2 & \text{solid wall, no slip} \end{cases}$$

$$t_T = \begin{cases} 0 & \text{adiabatic wall/centerline symmetry} \\ 2(1 - T_w/T_2) & \text{constant wall temperature} \end{cases}$$

Finally the expression can be written as

$$M_{ai,1+1/2} (\vec{V}_{i,2} - \vec{V}_{i,1}) = M_{ai,1+1/2} \begin{bmatrix} \rho_2 \\ u_2 \\ v_2 \\ w_2 \\ T_2 \end{bmatrix} = M_{ai,1+1/2}^* \vec{V}_{i,2} \quad (3.21)$$

where

$$M_{ai,1+1/2}^* = \frac{1}{J Re} \begin{bmatrix} 0 & 0 & 0 & 0 & 0 \\ 0 & t_u \beta_4 & t_u \beta_2 & 0 & 0 \\ 0 & t_u \beta_2 & t_u \beta_1 & 0 & 0 \\ 0 & 0 & 0 & t_u \beta_3 & 0 \\ 0 & 0 & 0 & 0 & \tau_r \frac{1}{Pr(\gamma_0 - 1)} \beta_5 \end{bmatrix}$$

Following an analogous procedure the second bracketed expression in Eq. (3.20), containing the additional viscous terms arising from the cylindrical coordinate formulation, can be modified to implement the viscous boundary conditions along the lower surface. It should be noted that the terms for the surface $j + 1/2$ are evaluated using the average of the cell variables at $j+1$ and j .

At the lower surface the boundary conditions are implemented by modifying the term at the surface

$$\hat{G}_{vcyl\ i,1+1/2} \quad (3.22)$$

After applying the viscous boundary conditions given in Eq. (3.18), and L'Hospital's Rule the last expression can be written as

$$\hat{G}_{vcyl\ i,1+1/2}^* = \frac{\mu}{Re} \begin{bmatrix} 0 \\ 0 \\ \frac{2}{3} z_\xi \frac{\partial v}{\partial r} \\ z_\xi \frac{\partial w}{\partial r} \\ 0 \end{bmatrix} \quad (3.23)$$

Substituting Eqs. (3.21) and (3.23) into Eq. (3.20) yields the modified expression for the viscous terms on the lower boundary

$$\begin{aligned} \frac{D}{\Delta \eta} \hat{G}_{vi,2} = & \left(M_{ai,2+1/2} (\bar{V}_{i,3} - \bar{V}_{i,2}) - M_{ai,1+1/2}^* \bar{V}_{i,2} \right) \\ & + \hat{G}_{vcyl\ i,2+1/2} - \hat{G}_{vcyl\ i,1+1/2}^* \end{aligned} \quad (3.24)$$

Following an analogous procedure the explicit viscous boundary conditions at the upper boundary are set by modifying the viscous flux terms at $j=JMAX-1$

$$\begin{aligned} \frac{D}{\Delta\eta} \hat{G}_{vi,JMAX-1} &= \frac{D_-}{\Delta\eta} \left(M_{ai,JMAX-1/2} \frac{D_+}{\Delta\eta} \tilde{V}_{i,JMAX-1} \right) + \frac{D}{\Delta\eta} \left(\hat{G}_{vcyl} \right)_{i,JMAX-1} \\ &= \left(M_{ai,JMAX-1/2} \left(\tilde{V}_{i,JMAX} - \tilde{V}_{i,JMAX-1} \right) - M_{ai,JMAX-3/2} \left(\tilde{V}_{i,JMAX-1} - \tilde{V}_{i,JMAX-2} \right) \right) \\ &\quad + \left(\hat{G}_{vcyl\ i,JMAX-1/2} - \hat{G}_{vcyl\ i,JMAX-3/2} \right) \end{aligned}$$

The modified viscous flux terms at $j=JMAX-1$ are

$$\begin{aligned} \frac{D}{\Delta\eta} \hat{G}_{vi,JMAX-1} &= \left(- M_{ai,JM-1/2}^* \tilde{V}_{i,JM-1} - M_{ai,JM-3/2} \left(\tilde{V}_{i,JM-1} - \tilde{V}_{i,JM-2} \right) \right) \\ &\quad - \hat{G}_{vcyl\ i,JMAX-3/2}^* \end{aligned}$$

$M_{ai,JM-1/2}^*$ contains the same terms as $M_{ai,1+1/2}^*$ but is now evaluated at $i,JMAX-1/2$.

The η derivative terms appearing in the explicit viscous source term, H_v , are evaluated using central differences just as was done for the \hat{G}_{vcyl} terms.

3.3.1.2 Upper and Lower Boundary- Implicit Boundary Conditions

The implicit inviscid boundary conditions across a surface of $\eta = \text{cst}$ will be examined first. The following conditions are specified to maintain impermeability of a solid wall or enforce centerline symmetry at the lower boundary

$$\begin{aligned} \delta\rho_{i,1} &= \delta\rho_{i,2} \\ \delta\rho u'_{i,1} &= \delta\rho u'_{i,2} \\ \delta\rho v'_{i,1} &= \begin{cases} +\delta\rho v'_{i,2} & \text{centerline symmetry} \\ -\delta\rho v'_{i,2} & \text{solid wall} \end{cases} \quad (3.25) \\ \delta\rho w_{i,1} &= \delta\rho w_{i,2} \\ \delta E_{ti,1} &= \delta E_{ti,2} \end{aligned}$$

where u' and v' are the rotated velocity components (See Appendix B) tangential and normal to a surface where $\eta = \text{cst}$.

The implicit viscous flux boundary conditions are set by the following conditions along the lower boundary

$$\begin{aligned}
 \delta u'_{i,1} &= \begin{cases} +\delta u'_{i,2} & \text{centerline symmetry} \\ -\delta u'_{i,2} & \text{solid wall, no slip} \end{cases} \\
 \delta v'_{i,1} &= \begin{cases} +\delta v'_{i,2} & \text{centerline symmetry} \\ -\delta v'_{i,2} & \text{solid wall, no slip} \end{cases} \\
 \delta w_{i,1} &= \begin{cases} +\delta w_{i,2} & \text{centerline symmetry} \\ -\delta w_{i,2} & \text{solid wall, no slip} \end{cases} \\
 \delta T_{i,1} &= \begin{cases} +\delta T_{i,2} & \text{adiabatic wall/centerline symmetry} \\ -\delta T_{i,2} & \text{constant temperature wall} \end{cases}
 \end{aligned} \tag{3.26}$$

These conditions are obtained by applying the operator $\delta = \Delta t \frac{\partial}{\partial t}$ to the explicit viscous boundary conditions in Eq. (3.18).

The implicit boundary conditions for the lower and upper boundaries are implemented by eliminating the $\hat{C}_{i,2}$ and $\hat{B}_{i,JMAX-1}$, matrices, respectively. The terms contained within them are incorporated into the $\tilde{A}_{i,2}$ and $\tilde{A}_{i,JMAX-1}$ matrices using the implicit boundary conditions to form the modified matrices $\tilde{A}_{i,2}^*$, $\tilde{A}_{i,JMAX-1}^*$.

Implicit Inviscid Boundary Conditions

The lower surface boundary conditions will be illustrated first. The inviscid terms in the cross-stream direction at the lower surface are contained in

$$\begin{aligned}
 \tilde{A}_{i,2} &\Rightarrow \frac{\Delta t}{V_{ij}} (B_{i,2+1/2}^{+n} - B_{i,1+1/2}^n) \\
 \tilde{C}_{i,2} &\Rightarrow \frac{\Delta t}{V_{ij}} (-B_{i,1+1/2}^{+n})
 \end{aligned}$$

The inviscid terms at the lower surface, $j = 1+1/2$, are combined along with the boundary conditions and placed into \tilde{A}_2^* as

$$\begin{aligned}\tilde{A}_{i,2}^* &\Rightarrow \frac{\Delta t}{V_{ij}} \left(B_{i,2+1/2}^{+n} - (B_{i,1+1/2}^{-n} + B_{i,1+1/2}^{+n}) \right) \\ &= \frac{\Delta t}{V_{ij}} \left(B_{i,2+1/2}^{+n} - (\delta B_{i,1+1/2}) \right)\end{aligned}\quad (3.27)$$

where $\delta B_{i,1+1/2}$ implements the implicit inviscid boundary condition

$$\delta B_{i,1+1/2} \delta Q_{i,2} = \begin{bmatrix} 0 & -r_\xi \delta P_{i,2} & z_\xi \delta P_{i,2} & 0 & 0 \end{bmatrix}^T$$

and is given by

$$\delta B_{i,1+1/2} = \begin{bmatrix} 0 & 0 & 0 & 0 & 0 \\ -r_\xi \alpha \beta & r_\xi u \beta & r_\xi v \beta & r_\xi w \beta & -r_\xi \beta \\ z_\xi \alpha \beta & -z_\xi \frac{\beta}{2} u & -z_\xi v \beta & -z_\xi w \beta & z_\xi \beta \\ 0 & 0 & 0 & 0 & 0 \\ 0 & 0 & 0 & 0 & 0 \end{bmatrix}$$

$$\alpha = \frac{u^2 + v^2 + w^2}{2} \quad \beta = (\gamma - 1)$$

All properties are evaluated at $j = 2$ and the metrics are evaluated at the $j = 1 + 1/2$ surface. Thus Eq. (3.27) is the implicit analog to Eq. (3.17).

In an analogous fashion the inviscid terms contained in \tilde{A}_{JMAX-1}^* are obtained by placing the inviscid term from $\hat{B}_{i,JMAX-1}$ into \tilde{A}_{JMAX-1} and applying the boundary conditions to obtain $\delta B_{i,JMAX-1/2}$ such that

$$\tilde{A}_{JMAX-1}^* = \frac{\Delta t}{V_{ij}} \left(\delta B_{i,JMAX-1/2} - (B_{i,JMAX-3/2}^{-n}) \right)$$

All properties in $\delta B_{i,JMAX-1/2}$ are evaluated at $j = JMAX-1$ and the metrics are evaluated at the $j = JMAX - 1/2$ surface.

Implicit Viscous Boundary Conditions

The lower surface boundary conditions will be illustrated first. The viscous terms in

the cross-stream direction at the lower surface are contained in

$$\begin{aligned}\tilde{A}_2 &\Rightarrow -\frac{\Delta t}{V_{ij}} \left(M_{ai,2+1/2}^n N_{i,2}^n + M_{ai,1+1/2}^n N_{i,2}^n - \left(\frac{M_{bi,2+1/2}^n \cdot M_{bi,1+1/2}^n}{2} \right) \right) \\ \tilde{C}_2 &\Rightarrow \frac{\Delta t}{V_{ij}} \left(M_{ai,1+1/2}^n N_{i,1}^n - \frac{M_{bi,1+1/2}^n}{2} \right)\end{aligned}$$

The viscous terms contained in \tilde{C}_2 at the lower surface, $j = 1+1/2$, are combined along with the boundary conditions and placed into \tilde{A}_2^* , resulting in

$$\tilde{A}_2^* \Rightarrow -\frac{\Delta t}{V_{ij}} \left(M_{ai,2+1/2}^n N_{i,2}^n + M_{ai,1+1/2}^* N_{i,2}^n - \left(\frac{M_{bi,2+1/2}^n \cdot M_{bi,1+1/2}^*}{2} \right) \right) \quad (3.28)$$

$M_{ai,1+1/2}^*$ is the same matrix used in the explicit calculation. $M_{bi,1+1/2}^*$ is obtained by applying the boundary conditions and L'Hospital's Rule as was done for the explicit viscous boundary condition.

In an analogous fashion the viscous terms contained in \tilde{A}_{JMAX-1}^* are obtained by placing the viscous terms from $\hat{B}_{i,JMAX-1}$ into \tilde{A}_{JMAX-1} and applying the boundary conditions to obtain

$$\begin{aligned}\tilde{A}_{JMAX-1}^* &\Rightarrow -\frac{\Delta t}{V_{ij}} \left(M_{ai,JMAX-1/2}^* N_{i,JMAX-1}^n + M_{ai,JMAX-3/2}^n N_{i,JMAX-1}^n \right) \\ &\quad - \frac{\Delta t}{V_{ij}} \left(- \left(\frac{M_{bi,JMAX-1/2}^* \cdot M_{bi,JMAX-3/2}^n}{2} \right) \right)\end{aligned}$$

$M_{ai,JMAX-1/2}^*$ is the same matrix used in the explicit calculation. $M_{bi,JMAX-1/2}^*$ is obtained by applying the boundary conditions and is found to be

$$M_{bi,JMAX-1/2}^* = [0]$$

Thus, the Gauss-Seidel expression to be evaluated at $j = 2$, i.e.,

$$\tilde{B}_{i,2} \delta \tilde{Q}_{i,3} + \tilde{A}_{i,2} \delta \tilde{Q}_{i,2} + \tilde{C}_{i,2} \delta \tilde{Q}_{i,1} = \text{RHS}_{i,2}$$

can be expressed as

$$\tilde{B}_{i,2} \delta \tilde{Q}_{i,3} + \tilde{A}_{i,2}^* \delta \tilde{Q}_{i,2} = \text{RHS}_{i,2}^*$$

where $\tilde{A}_{i,2}^*$ and $\text{RHS}_{i,2}^*$ contain the modified implicit and explicit terms, respectively. The modified terms implement the lower surface boundary conditions.

The Gauss-Seidel expression to be evaluated at $j = \text{JMAX}-1$

$$\tilde{B}_{i,\text{JM}-1} \delta \tilde{Q}_{i,\text{JM}} + \tilde{A}_{i,\text{JM}-1} \delta \tilde{Q}_{i,\text{JM}-1} + \tilde{C}_{i,\text{JM}-1} \delta \tilde{Q}_{i,\text{JM}-2} = \text{RHS}_{i,\text{JM}-1}$$

can be expressed as

$$\tilde{A}_{i,\text{JMAX}-1}^* \delta \tilde{Q}_{i,\text{JMAX}-1} + \tilde{C}_{i,\text{JMAX}-1} \delta \tilde{Q}_{i,\text{JMAX}-2} = \text{RHS}_{i,\text{JMAX}-1}^*$$

where $\tilde{A}_{i,\text{JMAX}-1}^*$ and $\text{RHS}_{i,\text{JMAX}-1}^*$ contain the modified implicit and explicit terms, respectively. The modified terms implement the upper surface boundary conditions.

The final form of the block-tridiagonal system, Eq. (3.16), is

$$\begin{bmatrix} \tilde{A}_{\text{JMAX}-1}^* & \tilde{C}_{\text{JMAX}-1} & & & \\ & \ddots & & & \\ & & \tilde{B}_j & \tilde{A}_j & \tilde{C}_j \\ & & & \ddots & \\ & & & & \tilde{B}_2 & \tilde{A}_2^* \end{bmatrix}_i \begin{bmatrix} \delta \tilde{Q}_{\text{JMAX}-1} \\ \vdots \\ \delta \tilde{Q}_j \\ \vdots \\ \delta \tilde{Q}_2 \end{bmatrix}_i = \begin{bmatrix} \text{RHS}_{\text{JMAX}-1}^* \\ \vdots \\ \text{RHS}_j \\ \vdots \\ \text{RHS}_2^* \end{bmatrix}_i \quad (3.29)$$

where superscript * indicates the term has been modified to implement the inviscid and viscous boundary conditions.

3.3.2 Boundary Conditions- Inlet and Outlet Planes

The Method of Characteristics (MOC) procedure about to be discussed was developed by Rai and Chaussee [35] as a variant of the method proposed by Chakravarthy [36]. Discussions and examples of implementing the following MOC procedure can also be found in [37, 38, 39].

The five eigenvalues of the \hat{E} flux in this study are given by (see Appendix C):

$$\begin{aligned} \lambda_{1,2,3} &= d_A u' \\ \lambda_4 &= d_A (u' + c) \\ \lambda_5 &= d_A (u' - c) \end{aligned}$$

These eigenvalues imply waves travel in specific directions (see Table 3.1). For example, in a subsonic inlet flow there are 4 positive eigenvalues given by $\lambda_{1,2,3,4}$. The fifth eigenvalue is negative and conveys information from the interior of the flow, upstream to the inlet plane. The equations containing the positive eigenvalues, which would propagate information from outside the boundary to the inlet plane (in the positive ξ direction), need to be discarded and replaced with boundary conditions since the characteristics coming from outside the boundary are not defined [36].

The MOC procedure will be briefly described. First the characteristics propagating information from outside the computational domain to the boundary are eliminated. Then the finite difference/volume representation of the governing equations is multiplied by the eigenmatrix normal to the boundary. This yields a decoupled set of characteristic equations. Multiplying the characteristic equations by a selection matrix allows the characteristic(s) within the computational domain to be retained. The eliminated characteristic equations are then replaced by appropriate boundary conditions.

3.3.2.1 Inlet and Outlet Planes- One-dimensional MOC Example

The MOC procedure will be illustrated using a simple example [36, 39]. First the characteristic equations for the one-dimensional Euler equations will be obtained. The quasi one-dimensional Euler equations can be written in vector form as

$$\frac{\partial \vec{Q}}{\partial t} + \frac{\partial \vec{E}}{\partial x} = \vec{H}$$

where

$$Q = \begin{bmatrix} \rho a \\ \rho u a \\ e a \end{bmatrix} \quad E = \begin{bmatrix} \rho u a \\ (\rho u^2 + P)a \\ (e + P)ua \end{bmatrix} \quad H = \begin{bmatrix} 0 \\ P \frac{da}{dx} \\ 0 \end{bmatrix}$$

In these expressions a = cross-sectional area. Defining the Jacobian matrix as $A \equiv \frac{\partial \vec{E}}{\partial \vec{Q}}$

produces

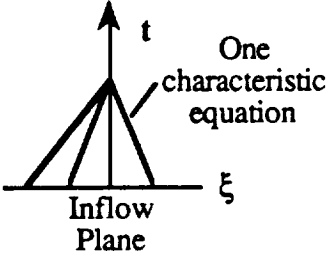
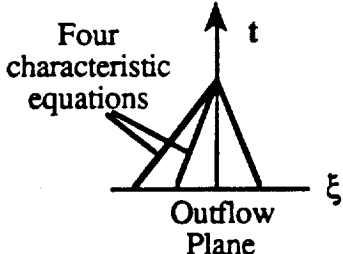
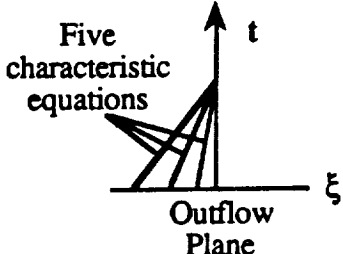
$$\frac{\partial \vec{Q}}{\partial t} + A \frac{\partial \vec{Q}}{\partial x} = \vec{H}$$

Transforming A to a diagonal matrix using the similarity transforms $A = L^{-1} \Lambda L$ yields

$$\frac{\partial \vec{Q}}{\partial t} + L^{-1} \Lambda L \frac{\partial \vec{Q}}{\partial x} = \vec{H}$$

where Λ is the diagonal matrix containing the eigenvalues $\lambda_{1,2,3} = u, u+c, u-c$ and L is a matrix composed of rows of eigenvectors.

Table 3.1 Required Boundary Conditions at Inlet and Outlet Plane Boundaries

Speed	Signal Propagation	Description	Specified Boundary Conditions
$c > u' > 0$		<p>Subsonic Inflow</p> $\lambda_{1,2,3,4} > 0$ $\lambda_5 < 0$	$P_t, T_t, v/u, w/u$
$c > u' > 0$		<p>Subsonic Outflow</p> $\lambda_{1,2,3,4} > 0$ $\lambda_5 < 0$	P
$u' > c$		<p>Supersonic Outflow</p> $\lambda_{1,2,3,4,5} > 0$	None, Extrapolate to obtain boundary values

Multiplying the above by L and defining $\frac{\partial \tilde{Q}}{\partial t} = L \frac{\partial \vec{Q}}{\partial t}$ and $\tilde{H} = L \vec{H}$ yields

$$\frac{\partial \tilde{Q}}{\partial t} + \Lambda \frac{\partial \tilde{Q}}{\partial x} = \tilde{H} \quad (3.30)$$

which is equivalent to the three decoupled characteristic equations

$$\frac{\partial \tilde{q}_i}{\partial t} + \lambda_i \frac{\partial \tilde{q}_i}{\partial x} = \tilde{h}_i$$

Each of the three equations has a specific direction and governs wave propagation in that direction. Thus there are left and right running waves in the flow.

Next a flux split algorithm to solve the one-dimensional Euler equations will be considered. As developed earlier for MacCormack's algorithm the flux vector, \vec{E} , in the one-dimensional Euler equations can be split into two parts with positive and negative eigenvalues

$$\vec{E} = \vec{E}^+ + \vec{E}^-$$

Using the Steger and Warming form of splitting

$$\Lambda = \Lambda^+ + \Lambda^-$$

and
$$\Lambda^+ = \frac{(\Lambda + |\Lambda|)}{2} \quad \Lambda^- = \frac{(\Lambda - |\Lambda|)}{2}$$

In addition
$$A = A^+ + A^-$$

with
$$A^+ = L^{-1} \Lambda^+ L \quad A^- = L^{-1} \Lambda^- L$$

and since \vec{E} is a homogeneous function of degree one we can write

$$\vec{E} = \vec{E}^+ + \vec{E}^- = (A^+ + A^-) \vec{Q}$$

By employing Euler implicit differencing in time, the flux split system can be

written as

$$\left[I - \Delta t D + \Delta t \left(\frac{\partial A^+}{\partial x} + \frac{\partial A^-}{\partial x} \right) \right] \delta \vec{Q} = -\Delta t \text{ RHS} \quad (3.31)$$

where

$$D = \frac{\partial \vec{H}}{\partial \vec{Q}} \quad \text{RHS} = \left(\frac{\partial \vec{E}^+}{\partial x} + \frac{\partial \vec{E}^-}{\partial x} - H \right)^n$$

The MOC will now be illustrated for subsonic flow at inlet and outlet boundaries. The first step is to neglect the incoming characteristics at the inlet in both the explicit and implicit portions of the algorithm. At the inlet the discretized equations reduce to

$$\left[I - \Delta t D + \Delta t \frac{\partial A^-}{\partial x} \right] \delta \vec{Q} = -\Delta t \left(\frac{\partial \vec{E}^-}{\partial x} - H \right)^n = -\Delta t \text{ RHS}$$

and at the outlet boundary

$$\left[I - \Delta t D + \Delta t \frac{\partial A^+}{\partial x} \right] \delta \vec{Q} = -\Delta t \left(\frac{\partial \vec{E}^+}{\partial x} - H \right)^n = -\Delta t \text{ RHS}$$

In the next step the modified governing equations at the inlet are multiplied by the eigenmatrix normal to the boundary, L . Using the definitions

$$A^\pm = L^{-1} \Lambda^\pm L \quad \text{and} \quad \delta \tilde{Q} = L \delta \vec{Q} \quad \text{yields}$$

$$\left[I - \Delta t D + \Delta t \frac{\partial \Lambda^-}{\partial x} \right] \delta \tilde{Q} = -\Delta t L \left(\frac{\partial \vec{E}^-}{\partial x} - H \right)^n$$

which is equivalent to the characteristic equation given in Eq. (3.30). Writing the last equation in terms of $\delta \tilde{Q}$ yields

$$L \left[I - \Delta t D + \Delta t \frac{\partial A^-}{\partial x} \right] \delta \vec{Q} = -\Delta t L \left(\frac{\partial \vec{E}^-}{\partial x} - H \right)^n \quad (3.32)$$

The next step is to multiply the characteristic equations given by Eq. (3.32) by a selection matrix, N^- , such that only the characteristic corresponding to the λ_3 eigenvalue is retained at the inlet. Thus N^- is given by

$$N^- = \begin{bmatrix} 0 & 0 & 0 \\ 0 & 0 & 0 \\ 0 & 0 & 1 \end{bmatrix}$$

Similarly, at the outlet in a subsonic flow the selection matrix, N^+ , must select the two characteristics corresponding to the two eigenvalues λ_1 and λ_2 .

$$N^+ = \begin{bmatrix} 1 & 0 & 0 \\ 0 & 1 & 0 \\ 0 & 0 & 0 \end{bmatrix}$$

Thus the expression at the inlet boundary, Eq. (3.32), becomes

$$N^- L \left[I - \Delta t D + \Delta t \frac{\partial A^-}{\partial x} \right] \delta \vec{Q} = -\Delta t N^- L \left(\frac{\partial \vec{E}^-}{\partial x} - H \right)^n \quad (3.33)$$

whereas at the outlet boundary

$$N^+ L \left[I - \Delta t D + \Delta t \frac{\partial A^+}{\partial x} \right] \delta \vec{Q} = -\Delta t N^+ L \left(\frac{\partial \vec{E}^+}{\partial x} - H \right)^n$$

The final step is to replace the characteristics that were removed with the appropriate boundary conditions. For a subsonic inlet flow the stagnation pressure, P_t , and stagnation temperature, T_t , are often specified.

The boundary conditions are expressed in vector form [36] by

$$\vec{\Omega}(\vec{Q}) \equiv (P_t \ T_t \ 0)^T \quad (3.34)$$

Performing a Taylor Series expansion of $\vec{\Omega}$ with respect to time yields

$$\vec{\Omega}^{n+1} = \vec{\Omega}^n + \Delta t \frac{\partial \vec{\Omega}}{\partial t} + \dots = \vec{\Omega}^n + \Delta t \frac{\partial \vec{\Omega}}{\partial \vec{Q}} \frac{\partial \vec{Q}}{\partial t} + \dots$$

But

$$\frac{\partial \vec{Q}}{\partial t} = \frac{\vec{Q}^{n+1} - \vec{Q}^n}{\Delta t} = \frac{\delta \vec{Q}^n}{\Delta t}$$

so

$$\vec{\Omega}^{n+1} = \vec{\Omega}^n + \frac{\partial \vec{\Omega}}{\partial \vec{Q}} \delta \vec{Q}^n$$

And hence

$$\delta \vec{\Omega} = \vec{\Omega}^{n+1} - \vec{\Omega}^n = \frac{\partial \vec{\Omega}}{\partial \vec{Q}} \delta \vec{Q}$$

To accelerate convergence to the desired steady-state solution, $\vec{\Omega}^{n+1}$ is held constant at the specified inlet distribution of $\vec{\Omega}_{\text{inlet}}$

$$\delta \vec{\Omega} = \frac{\partial \vec{\Omega}}{\partial \vec{Q}} \delta \vec{Q} = \vec{\Omega}_{\text{inlet}} - \vec{\Omega}^n \quad (3.35)$$

Finally, Eq. (3.35) is added to Eq. (3.33) to yield

$$\left[\frac{\partial \vec{\Omega}}{\partial \vec{Q}} + N \cdot L \left(I - \Delta t D + \Delta t \frac{\partial A}{\partial x} \right) \right] \delta \vec{Q} = \vec{\Omega}_{\text{inlet}} - \vec{\Omega}^n - \Delta t N \cdot L \left(\frac{\partial \vec{E}}{\partial x} - H \right)^n \quad (3.36)$$

This completes an example of how the MOC procedure is applied to the one-dimensional Euler equations.

3.3.2.2 MOC Applied to Present Numerical Procedure

The MOC procedure as applied to the present numerical algorithm will be illustrated now for a subsonic inlet flow (see Fig. 3.2). Consider the control volume at $i=2$ whose left edge is the inlet plane of the computational domain

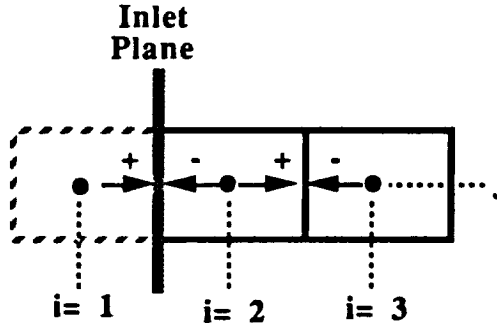


Figure 3.2 Inlet plane boundary condition schematic

The first step of the MOC procedure is to modify the numerical algorithm by removing the positive traveling characteristics at the inlet plane. Thus the implicit flux term, $\tilde{E}_{2,j}$, and the corresponding explicit flux term contained in $\text{RHS}_{2,j}$ are set equal to zero in Eq. (3.15)

$$\tilde{E}_{2,j} = - \frac{\Delta t}{\Delta \xi} A_{1+1/2,j}^+ \Rightarrow 0$$

In the next step the modified numerical algorithm is multiplied by the eigenmatrix normal to the boundary, L , and the selection matrix for a subsonic flow at the inlet plane, N^- . From the definition of \hat{E}

$$\hat{E} = A \tilde{Q} = S^{-1} R_A^{-1} C_A^{-1} \Lambda_A C_A R_A S \tilde{Q} = L^{-1} \Lambda_A L \tilde{Q}$$

we have

$$L^{-1} = S^{-1} R_A^{-1} C_A^{-1}$$

$$L = C_A R_A S$$

and

$$N^- = \text{diag}(0 \ 0 \ 0 \ 0 \ 1)$$

yielding

$$N^- L [\text{LHS Modified Eq. (3.15)}] = N^- L [\text{RHS Modified Eq. (3.15)}] \quad (3.37)$$

The final step is to replace the characteristics that were removed with the appropriate boundary conditions (since premultiplying the modified governing equations by $N^- L$ yields one equation for the five variables \tilde{Q}). For a subsonic swirling inlet flow Dutton [40, 41] found that specifying the stagnation pressure, P_t , stagnation temperature, T_t , ratio of swirling velocity to axial velocity, $\phi = w/u$, and the ratio of radial velocity to axial velocity, $\theta = v/u$, yielded the best results. Chang [39, 42] also specified these boundary conditions for his modeling work of swirling flow.

The boundary conditions are given by

$$\vec{\Omega}(\tilde{Q}) = (P_t \ T_t \ \frac{w}{u} \ \frac{v}{u} \ 0)^T \quad (3.38)$$

The Jacobian of Eq. (3.38), $\frac{\partial \vec{\Omega}}{\partial \tilde{Q}}$, supplies the remaining four conditions at the inlet. Thus the term $A_{1+1/2,j}^{+n} \delta \tilde{Q}_{1,j}$ is removed and replaced with boundary conditions given by $\left(\frac{\partial \vec{\Omega}}{\partial \tilde{Q}} \delta \tilde{Q} \right)_{1,j}$. Adding $\frac{\partial \vec{\Omega}}{\partial \tilde{Q}} \delta \tilde{Q} = \vec{\Omega}_{\text{inlet}} - \vec{\Omega}^n$ to Eq. (3.37) results in five equations for the five variables contained in \tilde{Q} .

An analogous MOC procedure is applied at the exit plane of the thruster if the flow is subsonic. However, the selection and boundary condition matrices are different because the number of characteristics traveling to the outlet plane from inside the computational plane is different than at the inlet plane. For a subsonic flow there are four characteristics conveying information to the outlet plane from the interior of the computational domain.

Thus, the selection matrix is given by

$$N^- = \text{diag}(1 \ 1 \ 1 \ 1 \ 0)$$

The one characteristic moving in a negative direction is replaced by specifying the static pressure, P. The single boundary condition is given by

$$\vec{\Omega}(\vec{Q}) = (0 \ 0 \ 0 \ 0 \ P)^T = 0$$

If the flow is supersonic at the outlet plane all of the five characteristics are conveying information to the outlet plane from the interior of the computational domain. Thus values of $\delta\vec{Q}$ at the outlet plane are obtained by extrapolation from interior values. However, in the present study extrapolation is used at the exit plane in both subsonic and supersonic regions.

3.4 Solution Procedure

To implement the Gauss-Seidel line relaxation procedure the explicit solution, $\Delta\vec{Q}_{i,j}^n$, is first obtained at all points in the flowfield using data from the current time level, n. The flowfield is then swept in the axial direction from the nozzle exit plane to the inlet and then swept in the opposite direction. At each axial location, i, the block-tridiagonal matrix equation given by Eq. (3.29) is solved at all j using a routine described in [27]. The most current information available for $\delta\vec{Q}_{i-1}^{n+1}$ or $\delta\vec{Q}_{i+1}^{n+1}$ is used during the sweeps. After sweeping the field in both directions the solution is updated using

$$\vec{Q}_{i,j}^{n+1} = \vec{Q}_{i,j}^n + \delta\vec{Q}^n \quad (3.39)$$

The procedure is continued until the solution has converged, i.e., $\delta\vec{Q}^n \approx 0$.

*It has long been an axiom of mine that the little things
are infinitely the most important.*

Sir Arthur Conan Doyle, 1925

Grid Generation

4.1 Introduction

Complicated two- or three-dimensional boundary shapes present several challenges when attempting to obtain a finite difference solution for a fluid mechanics problem. For instance, irregular boundaries will not coincide with a regularly spaced mesh as illustrated in Fig. 4.1.

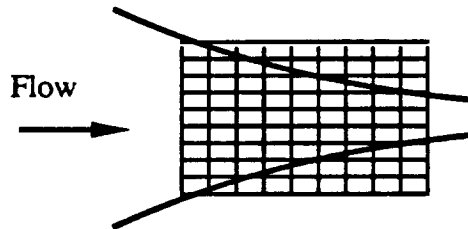


Figure 4.1 Mismatch between an irregular boundary and a rectangular grid

Hence, it would be necessary to interpolate boundary conditions for grid points not falling on a grid point. Because boundary conditions govern the solution obtained in the interior of the region, they must be accurately applied and interpolation would produce errors which will be propagated throughout the interior region.

It may be desirable to "pack" grid in a particular region of interest, e.g. near a wall to resolve the boundary layer flow as illustrated in Fig. 4.2.

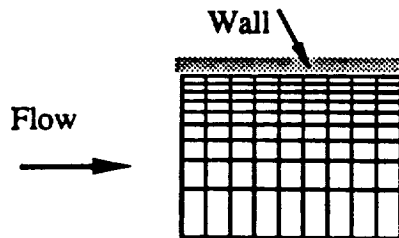


Figure 4.2 Grid clustering near a solid surface

These difficulties can be overcome by using the coordinate transformation, discussed in Section 2.5, to transform the physical plane into a computational plane as illustrated in Fig. 4.3.

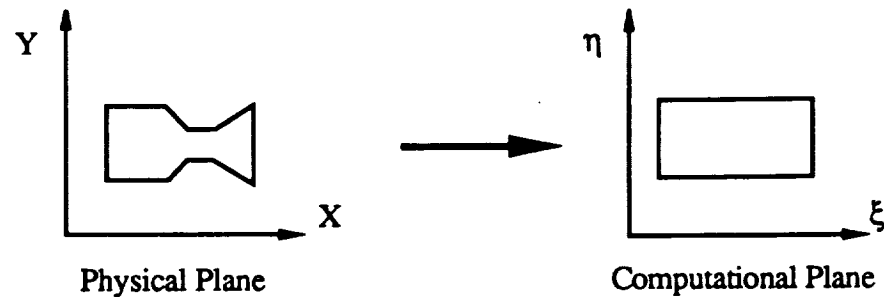


Figure 4.3 **Coordinate transformation between physical plane and computational plane**

The coordinate transformation results in an irregularly shaped object in the physical plane becoming a rectangular object in the computational plane. Because the flowfield boundary is now rectangular, boundary conditions may be applied without interpolation between grid points which in turn allows the clustering of grid points in any region in the physical plane.

Another possible source of error is the skewness of a cell in the physical plane, especially near the boundaries. By providing the ability to compare grids with a variety of cell skewness, especially grids with varying degrees of boundary grid orthogonality, the effect of the grid on the numerical solution can be determined.

The ability to generate a numerical grid for a wide variety of converging-diverging nozzles was needed to accomplish the objectives of this work. Such a scheme should provide for orthogonal grid near boundaries and the ability to "pack" grid in regions of large flow gradients. A grid generation scheme possessing these properties is developed in this chapter by solving a set of elliptic partial differential equations. The initial scheme is found to maintain the boundary distribution of grid points throughout the interior region if Poisson's equation is used in place of Laplace's equation. However, the resulting grid is not orthogonal to the boundaries. The source terms, or control functions, appearing in the Poisson equations are then modified to provide boundary orthogonality and spacing control of grid points near the boundary.

4.2 Previous Research

One method of numerically generating the grid coordinates involves the solution of the following Poisson equations

$$\begin{aligned}\xi_{xx} + \xi_{yy} &= P'(\xi, \eta) \\ \eta_{xx} + \eta_{yy} &= Q'(\xi, \eta)\end{aligned}\tag{4.1}$$

By switching the independent and dependent variables the equations are transformed to ξ, η coordinates resulting in

$$\begin{aligned}\alpha x_{\xi\xi} - 2\beta x_{\xi\eta} + \gamma x_{\eta\eta} &= -J^2(P'(\xi, \eta) x_{\xi} + Q'(\xi, \eta) x_{\eta}) \\ \alpha y_{\xi\xi} - 2\beta y_{\xi\eta} + \gamma y_{\eta\eta} &= -J^2(P'(\xi, \eta) y_{\xi} + Q'(\xi, \eta) y_{\eta}) \\ \alpha &= x_{\eta}^2 + y_{\eta}^2 \\ \beta &= x_{\xi}x_{\eta} + y_{\xi}y_{\eta} \\ \gamma &= x_{\xi}^2 + y_{\xi}^2\end{aligned}\tag{4.2}$$

where J denotes the Jacobian of the coordinate transformation

$$J = \frac{\partial(x, y)}{\partial(\xi, \eta)} = x_{\xi}y_{\eta} - x_{\eta}y_{\xi}\tag{4.3}$$

Thompson, et al. [43] employed this method using various exponential functions containing adjustable parameters for the source terms P' and Q' . These parameters allowed the interior grid spacing to be controlled to some degree. However, as pointed out by Thomas and Middlecoff [44], the proper choice of parameters was geometry dependent and required experimentation.

The spacing of grid points along the physical boundary can be set as desired. While this spacing provides Dirichlet boundary conditions for the physical coordinates in the transformed plane (Eqs. 4.2) it is difficult to maintain this spacing in the interior of the region. When P' and $Q' = 0$, i.e., when Laplace equations are used to solve for the interior grid distribution, internal spacing control is lost and the boundary grid point distribution is not maintained in the interior. Instead, Poisson equations must be used to maintain the boundary grid distribution in the interior by developing expressions for the source terms P' and Q' on the boundary.

Thomas and Middlecoff [44] choose source terms such that Eqs. (4.2) possessed exponential solutions but were not exponential functions themselves and hence had no parameters to adjust

$$\begin{aligned}P' &= \phi(\xi, \eta)(\xi_x^2 + \xi_y^2) = \frac{\phi(\xi, \eta)\alpha}{J^2} \\ Q' &= \psi(\xi, \eta)(\eta_x^2 + \eta_y^2) = \frac{\psi(\xi, \eta)\gamma}{J^2}\end{aligned}\tag{4.4}$$

Eqs. (4.4) are then substituted into Eqs. (4.2) to obtain

$$\begin{aligned}\alpha (x_{\xi\xi} + \phi x_{\xi}) - 2\beta x_{\xi\eta} + \gamma (x_{\eta\eta} + \psi x_{\eta}) &= 0 \\ \alpha (y_{\xi\xi} + \phi y_{\xi}) - 2\beta y_{\xi\eta} + \gamma (y_{\eta\eta} + \psi y_{\eta}) &= 0\end{aligned}\quad (4.5)$$

Constraints that the transverse coordinate curves be locally straight and orthogonal to the boundary were then developed. Along $\xi = \xi(x,y) = \text{constant}$ (See Fig. 4.4) we can write

$$\begin{aligned}d\xi &= \xi_x dx + \xi_y dy = 0 \\ \text{or} \\ \left(\frac{dy}{dx}\right)_{\xi=\text{cst}} &= -\frac{\xi_x}{\xi_y}\end{aligned}\quad (4.6)$$

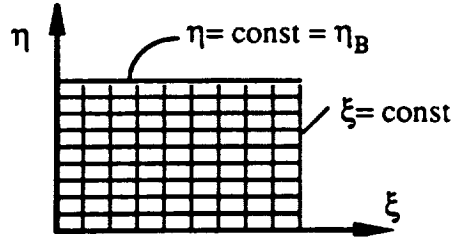


Figure 4.4 Grid boundaries in the computational plane

But from the coordinate transformation (see for instance Anderson et al. [27]) the metrics are $\xi_x = y_{\eta}/J$ and $\xi_y = -x_{\eta}/J$. Thus, the slope can be expressed as

$$\left(\frac{dy}{dx}\right)_{\xi=\text{cst}} = \frac{y_{\eta}}{x_{\eta}} \quad (4.7)$$

Similarly, along $\eta = \eta(x,y) = \text{constant}$

$$\left(\frac{dy}{dx}\right)_{\eta=\text{cst}} = -\frac{\eta_x}{\eta_y} = \frac{y_{\xi}}{x_{\xi}} \quad (4.8)$$

For ξ and η surfaces to be perpendicular the product of their slopes must equal -1 and local orthogonality at a boundary $\eta = \text{constant}$ can be obtained using Eqs. (4.7) and (4.8), i.e.,

$$\begin{aligned}\left(\frac{y_{\xi}}{x_{\xi}}\right) \cdot \left(\frac{y_{\eta}}{x_{\eta}}\right) &= -1 \\ \text{or} \\ x_{\xi} x_{\eta} + y_{\xi} y_{\eta} &= 0 = \beta\end{aligned}\quad (4.9)$$

The constraint that in the neighborhood of the boundary $\eta = \eta_B$, as illustrated in Fig. 4.4, the transverse coordinate lines $\xi = \text{constant}$ be locally straight (i.e., have zero curvature) by requiring the change in slope be zero

$$\frac{\partial}{\partial \eta} \left(\frac{y_\eta}{x_\eta} \right) = 0 \quad (4.10)$$

Expressions can now be derived for ϕ and ψ . Eqs. (4.5) can be combined to eliminate ψ between the two equations. Along a boundary $\eta = \eta_B$ we can then apply the condition of local orthogonality, Eq. (4.9), and zero curvature, Eq. (4.10). A limiting form of Eqs.(4.5) can then be solved directly for the parameter ϕ that is valid at the boundary $\eta = \eta_B$, i.e.,

$$\phi = - (x_\xi x_{\xi\xi} + y_\xi y_{\xi\xi}) / (x_\xi^2 + y_\xi^2) \quad (4.11)$$

An analogous procedure can be followed to obtain an expression for ψ along $\xi = \xi_B$, or by merely substituting ϕ, ξ for ψ, η , respectively, in Eq. (4.11). Hence,

$$\psi = - (x_\eta x_{\eta\eta} + y_\eta y_{\eta\eta}) / (x_\eta^2 + y_\eta^2) \quad (4.12)$$

The parameters ϕ and ψ along the boundaries can now be centrally differenced and evaluated from the given grid point distribution established on $\eta = \eta_B$ (horizontal boundaries) and $\xi = \xi_B$ (vertical boundaries), respectively. ϕ and ψ in the interior are determined by interpolation. The former, ϕ , by linearly interpolating along vertical lines of $\xi = \text{constant}$ and the latter, ψ , by linearly interpolating along horizontal lines of $\eta = \text{constant}$. Once interior values of ϕ and ψ are obtained, Eqs. (4.5) can be solved iteratively for the interior values of x, y by SLOR.

We will now apply this procedure to the physical domain shown in Fig. 4.5 and used by Thomas and Middlecoff [44]

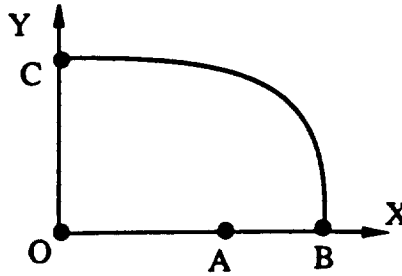


Figure 4.5 Thomas and Middlecoff boundary in the physical plane

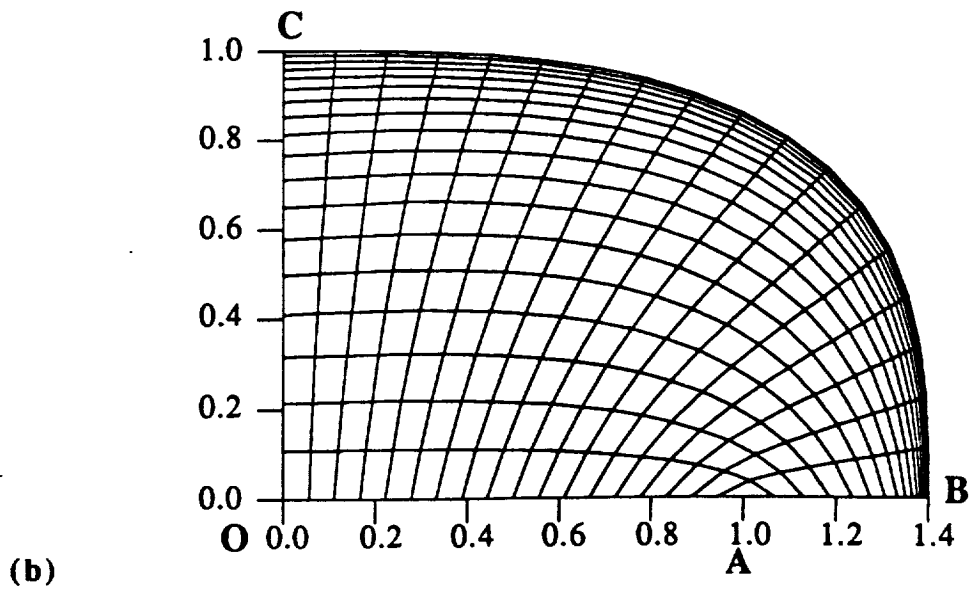
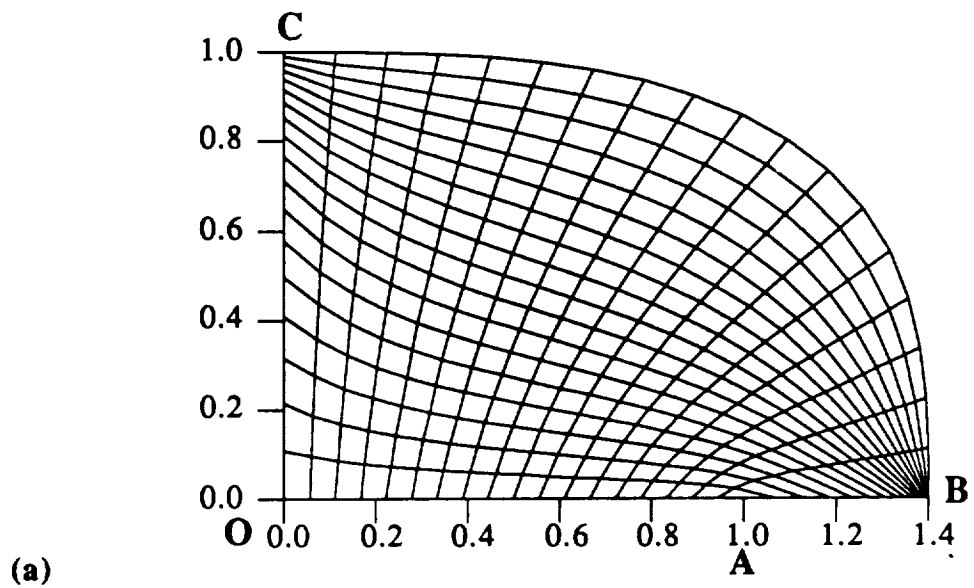


Figure 4.6 Grid distribution for Thomas & Middlecoff geometry; equal spacing on boundary BC, (a) Laplace solution, (b) Poisson solution

In this case, the arc BC (the nozzle wall) was generated by the superellipse $\left(\frac{x}{a}\right)^n + \left(\frac{y}{b}\right)^n = 1$, where $n = 3$, $b/a = 1.0 / 1.4$. Along segments OC, and AB boundary values (x,y) were clustered near the points C and B, respectively. Equally spaced boundary values were specified along boundary segments OA, and BC.

Figure 4.6 shows the results for $P'=Q'=0$ (Laplace's equation), and for P' and $Q' \neq 0$ (Poisson's equation, using the results developed above). In the Laplace solution it can be seen that the boundary point distribution is not maintained in the interior, while the Poisson solution maintains the boundary spacing throughout the interior.

Good grid orthogonality at the boundaries is obtained on all boundaries except segment OA as point A is approached. Non-orthogonality occurs because the boundary conditions derived for P' and Q' assumed coordinate lines were locally straight and orthogonal at the boundary, but these conditions were not enforced in the numerical routine.

Figure 4.7 shows the results for the Laplace and Poisson solutions when the boundary point distribution on segment BC is not equally spaced (all other boundary segment spacings remained the same). The boundary point distribution is again maintained in the interior in the Poisson solution when compared to the Laplace solution. However, orthogonality along boundary segment BC is very poor. Thus, choice of the boundary point distribution greatly affects the orthogonality of the solution using the P' and Q' relationships developed above.

The Poisson procedure that has been described was applied to a geometry representative of current low-power arcjet thrusters [6]. Figure 4.8 shows the results for two different boundary point distributions along the top and bottom boundaries. The first result is for the case in which the top and bottom distributions are the same and are clustered about the center of the nozzle throat. The second is for the same bottom boundary distribution but with tighter clustering around the nozzle throat along the top boundary. In both cases the left and right boundary distributions are the same and are proportioned to resolve the wall boundary layers in viscous flows.

In both cases the boundary point distribution has been maintained in the interior. Orthogonality along parallel surfaces has been maintained but along the sloping walls there is poor orthogonality. In fact the "vertical" coordinate lines are essentially vertical regardless of the slope of the wall they intersect. Magnified views near the wall and at the throat, see Figure 4.9, verify that the grid is not orthogonal at the boundary. It should also be pointed out that the solution obtained for different amounts of clustering about the nozzle throat does exhibit slightly better orthogonality at the wall. This is by virtue of the varied amounts of clustering used on the top and bottom boundaries.

If a numerical routine is developed that provides orthogonality at a boundary we should expect to see vertical grid lines, for a case where the top and bottom boundaries have the same point distribution, that have an "S" shape appearance (see Fig. 4.10).

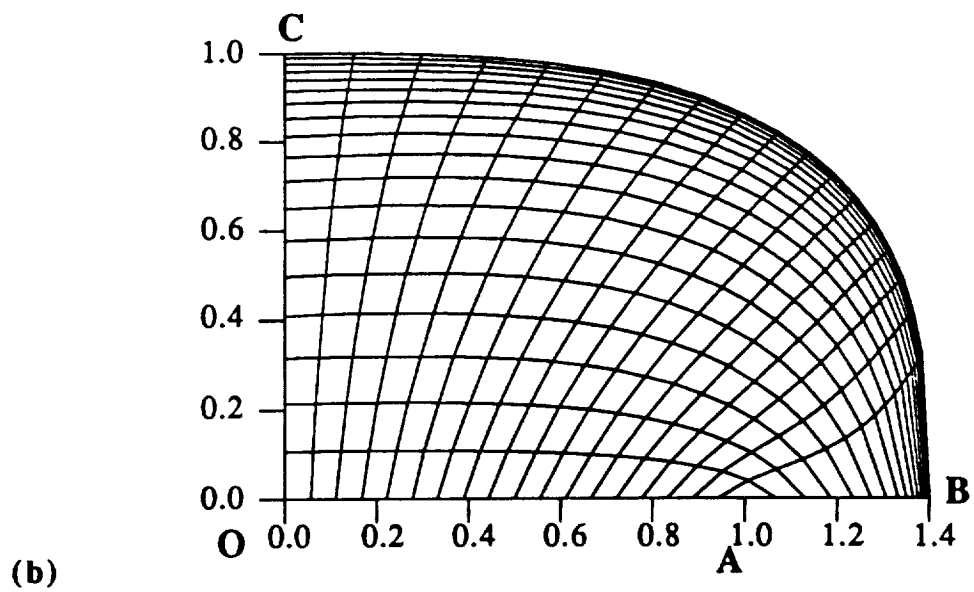
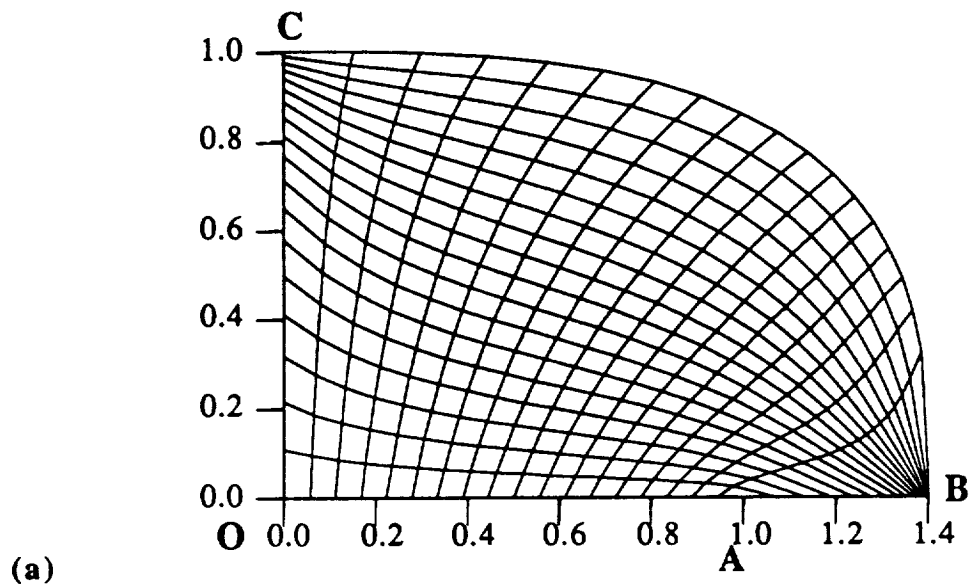
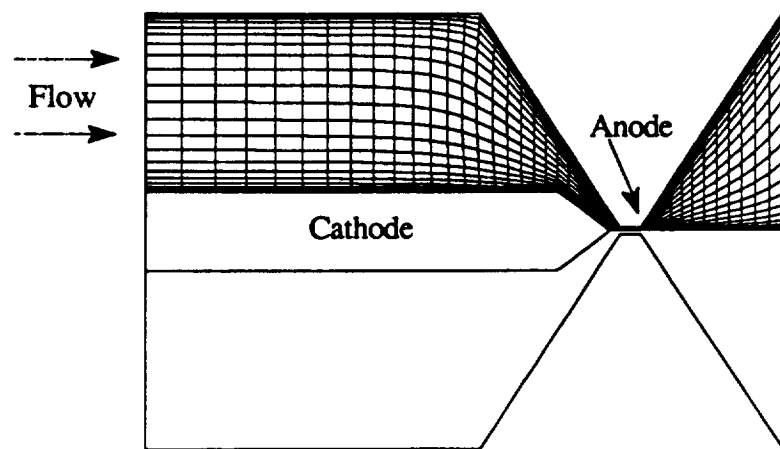
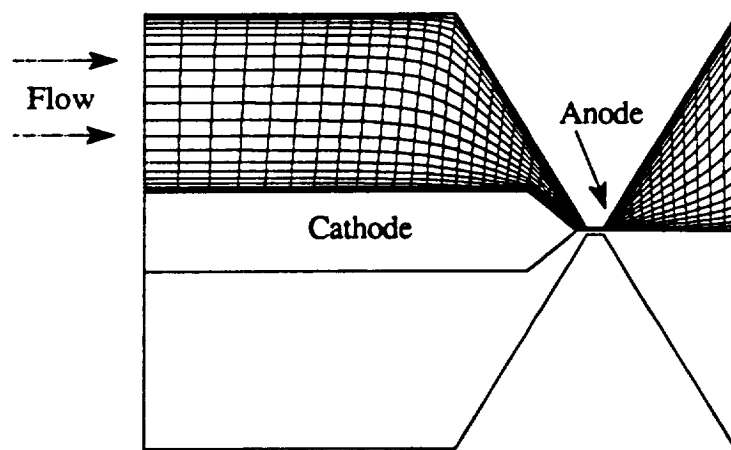


Figure 4.7 Grid distribution for Thomas and Middlecoff [44] geometry; clustered spacing on boundary BC, (a) Laplace solution, (b) Poisson solution



(a)



(b)

Figure 4.8 Poisson grid distributions for an arcjet thruster geometry with, (a) Same point distributions, (b) different point distributions, on top and bottom boundaries

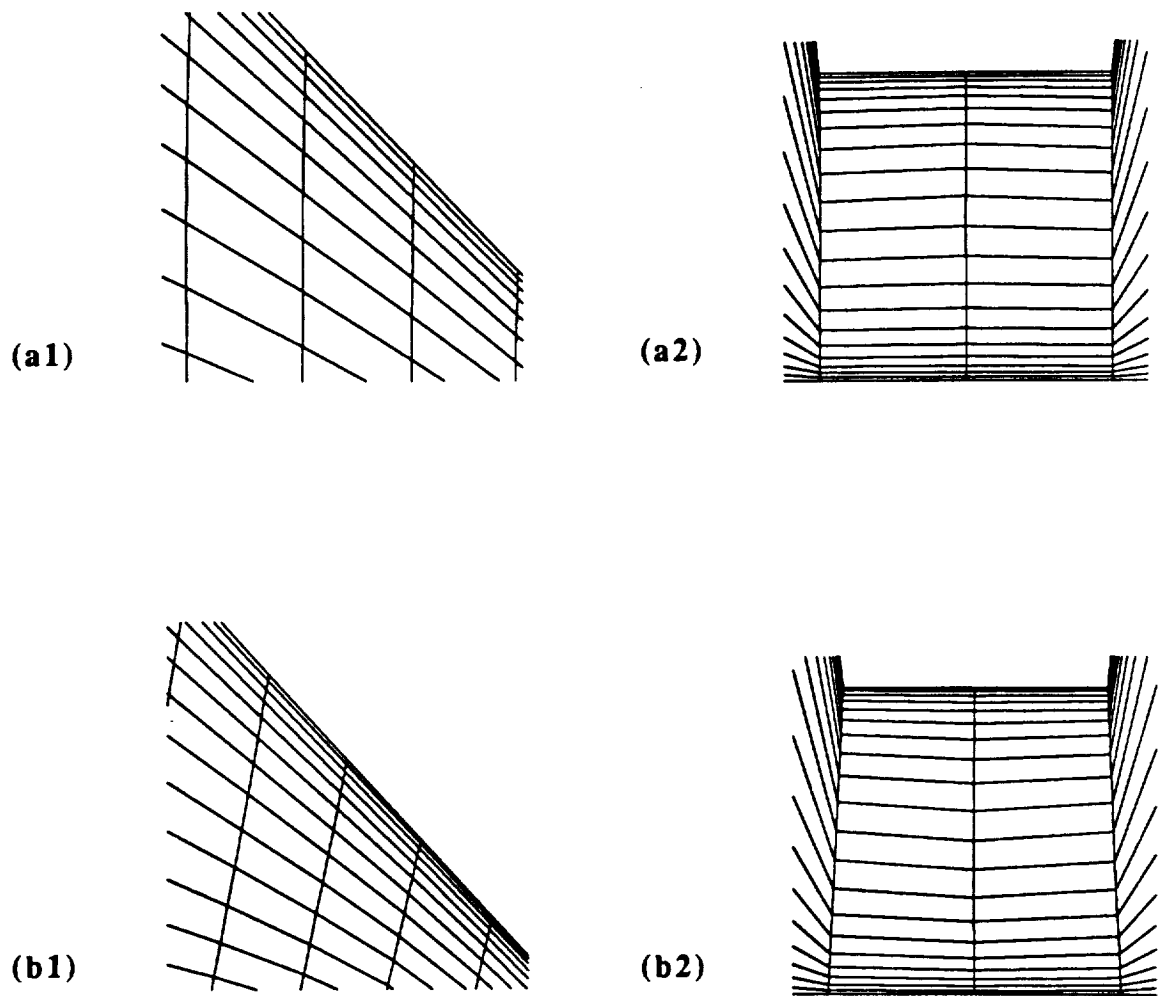


Figure 4.9 Magnified view of Poisson grid distributions for an arcjet thruster geometry ((1) upstream nozzle wall, (2) nozzle throat) with, (a) same point distributions, (b) different point distributions, on top and bottom boundaries

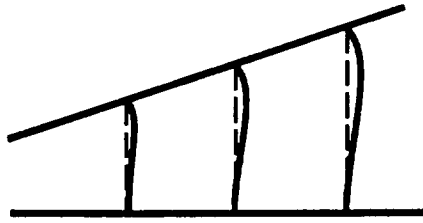


Figure 4.10 Expected orthogonal boundary grid distribution for an unclustered boundary grid pt. distribution

On the other hand if we specify the top boundary point distribution to be clustered tighter than the bottom boundary distribution we should expect to see vertical grid lines such as those drawn in Fig. 4.11.

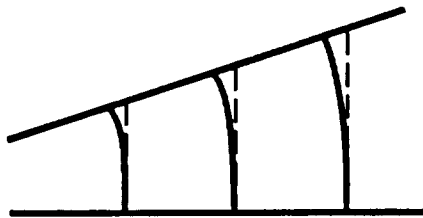


Figure 4.11 Expected orthogonal boundary grid distribution for a clustered boundary grid pt. distribution

Thus, to improve orthogonality throughout the interior of the region it is advantageous to cluster the top and bottom boundaries differently and eliminate the "S" shaped grid that can be expected to be produced by an algorithm ensuring orthogonality at the boundary.

4.2 Wall Orthogonality Modifications

Because the numerical algorithm is not designed to ensure that the grid is locally orthogonal at the boundary another method was needed to improve the approach used. Note that P' and Q' , as calculated above on the boundaries, do not require any information from the interior of the region. Examination of Eqs. (4.11) and (4.12) reveals ϕ and ψ only require information along their respective boundaries, e.g., ϕ is calculated on a line of constant η and is centrally differenced using the surrounding values of x and y in the ξ direction and ψ is calculated on a line of constant ξ and is centrally differenced using the surrounding values of x and y in the η direction. The control functions contain no information from the interior region and are unable to produce orthogonal grid near a

boundary unless a fortuitous choice for the boundary grid point distribution is made.

Thompson [45, 46] has derived source terms from the same governing equations used above but which require interior grid point information. As will be shown these source terms produce a grid which is locally orthogonal and maintains the boundary point distribution in the interior region.

Table 4.1 contains a summary of the notation differences between the work by Thomas & Middlecoff [44], the current research, and Thompson [45, 46]. Using the Thompson notation we can rewrite Eq. (4.5) as

$$\begin{aligned} |r_\eta|^2 (x_{\xi\xi} + P x_\xi) - 2 \vec{r}_\xi \cdot \vec{r}_\eta x_{\xi\eta} + |r_\xi|^2 (x_{\eta\eta} + Q x_\eta) &= 0 \\ |r_\eta|^2 (y_{\xi\xi} + P y_\xi) - 2 \vec{r}_\xi \cdot \vec{r}_\eta y_{\xi\eta} + |r_\xi|^2 (y_{\eta\eta} + Q y_\eta) &= 0 \end{aligned} \quad (4.13)$$

Similarly the orthogonality boundary condition, Eq. (4.9) can be written as

$$\vec{r}_\xi \cdot \vec{r}_\eta = 0 \quad (4.14)$$

Multiplying the first of Eqs. (4.13) by \hat{i} and the second by \hat{j} and adding yields

$$|r_\eta|^2 (\hat{r}_{\xi\xi} + P \hat{r}_\xi) - 2 \vec{r}_\xi \cdot \vec{r}_\eta \hat{r}_{\xi\eta} + |r_\xi|^2 (\hat{r}_{\eta\eta} + Q \hat{r}_\eta) = 0 \quad (4.15)$$

The orthogonality condition, Eq. (4.14), is imposed next on Eq. (4.15) to obtain an equation for P and Q valid on the boundary

$$|r_\eta|^2 (\hat{r}_{\xi\xi} + P \hat{r}_\xi) + |r_\xi|^2 (\hat{r}_{\eta\eta} + Q \hat{r}_\eta) = 0 \quad (4.16)$$

We now find $\frac{\vec{r}_\xi \cdot \vec{r}_\xi}{|r_\eta|^2}$ and $\frac{\vec{r}_\eta \cdot \vec{r}_\eta}{|r_\xi|^2}$ of Eq. (4.16) and obtain the following expressions for P and Q

$$P = - \frac{\vec{r}_\xi \cdot \vec{r}_{\xi\xi}}{|r_\xi|^2} - \frac{\vec{r}_\xi \cdot \vec{r}_{\eta\eta}}{|r_\eta|^2} = \phi - \frac{\vec{r}_\xi \cdot \vec{r}_{\eta\eta}}{|r_\eta|^2} \quad (4.17)$$

$$Q = - \frac{\vec{r}_\eta \cdot \vec{r}_{\eta\eta}}{|r_\eta|^2} - \frac{\vec{r}_\eta \cdot \vec{r}_{\xi\xi}}{|r_\xi|^2} = \psi - \frac{\vec{r}_\eta \cdot \vec{r}_{\xi\xi}}{|r_\xi|^2} \quad (4.18)$$

Table 4.1 Grid Generation Notation (Rosetta Stone)

Thomas & Middlecoff	Current Research	Thompson
$\frac{\phi(\xi,\eta)\alpha}{J^2}$	P'	$\frac{P(\xi,\eta) r_\eta ^2}{J^2}$
$\frac{\psi(\xi,\eta)\gamma}{J^2}$	Q'	$\frac{Q(\xi,\eta) r_\xi ^2}{J^2}$
α	$x_\eta^2 + y_\eta^2$	$ r_\eta ^2$
γ	$x_\xi^2 + y_\xi^2$	$ r_\xi ^2$
β	$x_\xi x_\eta + y_\xi y_\eta$	$\vec{r}_\xi \cdot \vec{r}_\eta$
$x_\xi y_\eta - x_\eta y_\xi$	J	$x_\xi y_\eta - x_\eta y_\xi$
$\frac{-(x_\xi x_{\xi\xi} + y_\xi y_{\xi\xi})}{(x_\xi^2 + y_\xi^2)}$	ϕ	$\frac{-\vec{r}_\xi \cdot \vec{r}_{\xi\xi}}{ r_\xi ^2}$
$\frac{-(x_\eta x_{\eta\eta} + y_\eta y_{\eta\eta})}{(x_\eta^2 + y_\eta^2)}$	ψ	$\frac{-\vec{r}_\eta \cdot \vec{r}_{\eta\eta}}{ r_\eta ^2}$

Thus the control functions derived by Thompson, P and Q, contain the control functions used in the Thomas and Middlecoff approach, ϕ and ψ , as well as additional terms. These additional terms are related to the radius of curvature of the boundary [47] and are evaluated using the interior point distribution.

For example, in P the second term is

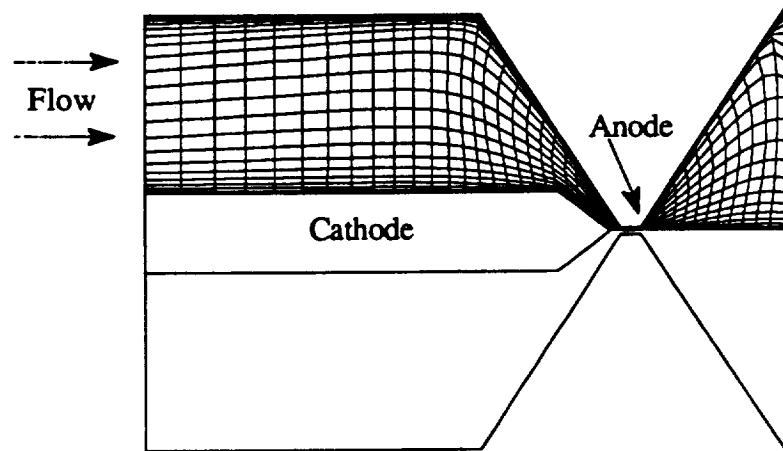
$$\frac{\vec{r}_\xi \cdot \vec{r}_{\eta\eta}}{|\vec{r}_\eta|^2} = \frac{x_\xi x_{\eta\eta} + y_\xi y_{\eta\eta}}{(x_\eta^2 + y_\eta^2)}$$

P is evaluated along two boundary lines of constant η corresponding to the outer wall, and the cathode surface/centerline of the arcjet. x varies along this line of constant η . Hence, as discussed previously for ϕ and ψ , the derivatives x_ξ and y_ξ can be directly evaluated from the given boundary point distribution using central differences. The derivatives in the η direction are evaluated along a line of constant ξ using one-sided differences into the interior of the region.

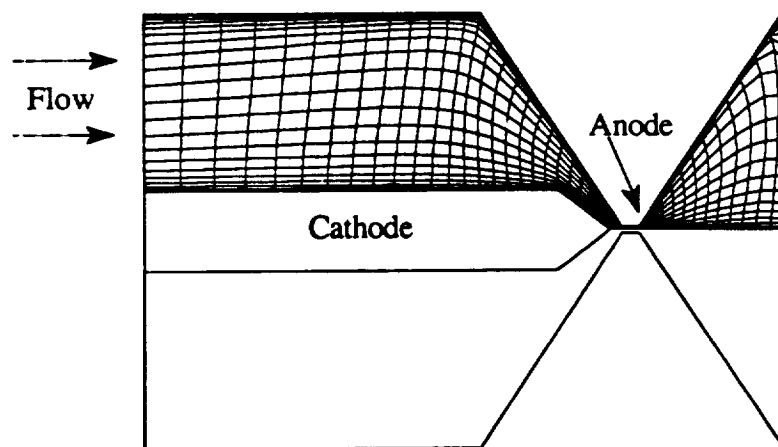
The grid generation algorithm was modified to include the source terms shown in Eqs. (4.17) and (4.18). P and Q are calculated on the boundary using an initial interior point distribution based on the boundary point distribution. Interpolation from the boundary values of P and Q are used to obtain P and Q in the interior. Equations (4.13) (as were Eqs. (4.5)) are then solved for x and y using Gauss-Seidel iteration with Successive Over Relaxation (SOR). If the solution for x and y has not converged sufficiently then the interior point distribution just determined is used to again calculate P and Q on the boundary. The process is repeated until the smallest change between iterations for all values of x and y is below some threshold, e.g., 1.0×10^{-4} .

Figure 4.12 illustrates the results of the modified control functions, Eqs. (4.17) and (4.18), for two different cases of top and bottom boundary point distributions. The first case has the same point distribution on the top and bottom boundaries. The second has a top boundary point distribution that is clustered closer around the nozzle throat than the bottom boundary point distribution. The vertical grid lines in Fig. 4.12, lines of constant ξ , can be seen to be orthogonal along the top and bottom boundaries.

Figure 4.13 contains a magnified view of the upper boundary at positions upstream of the nozzle throat and near the nozzle exit. Comparison between Figures 4.9 and 4.13 demonstrate the improved orthogonality at the boundary upstream of the nozzle throat using the modified control functions. However, at the nozzle exit, along the top boundary, it can be seen that the grid points in the interior have clustered very closely to the wall. Because the spacing of the right vertical boundary has not been maintained adequately in the interior, the grid lines, lines of constant η , are unacceptably skewed. The close clustering near the wall was caused by the additional control function [46].



(a)



(b)

Figure 4.12 Modified control function grid distributions for an arcjet thruster geometry (a) same point distributions, (b) different point distributions, on top and bottom boundaries

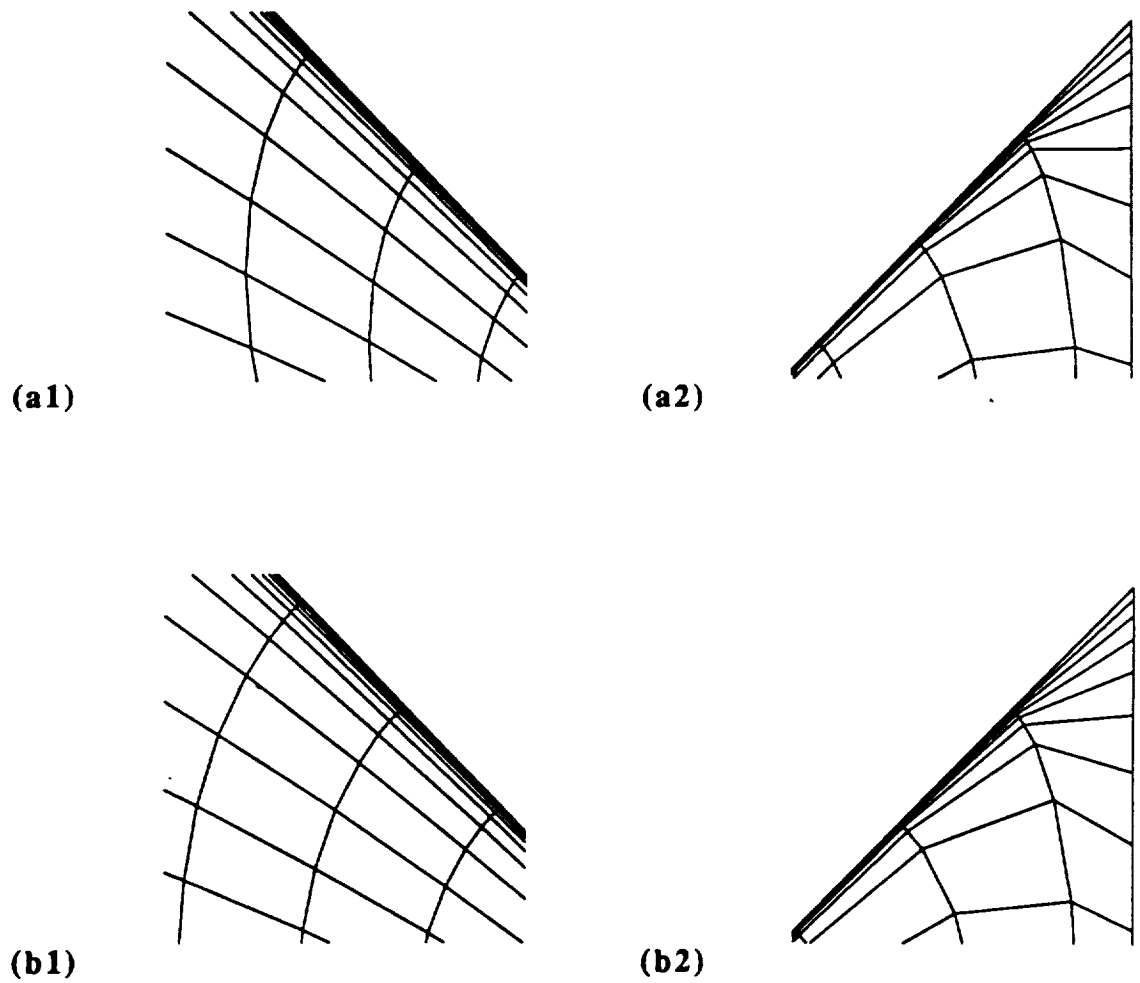


Figure 4.13 Magnified view of modified control function grid distributions for an arcjet thruster geometry ((1) upstream nozzle wall, (2) nozzle exit) with, (a) same point distributions, (b) different point distributions, on top and bottom boundaries

To eliminate the skewed grid lines at the nozzle exit the spacing of the first grid point from the top and bottom boundaries was specified by Sorenson [48]. The spacing between the first grid point and the boundary on a vertical boundary line was multiplied by the ratio between the height of the vertical boundary and the spacing between the top and bottom boundaries on a line of constant ξ . The left boundary spacing was used for points upstream of the throat exit and the right boundary spacing was used for points downstream of the throat exit.

In addition, a limit was imposed on the change per iteration of the additional control functions shown in Eqs. (4.17) and (4.18). Sorenson's [48] limiting function was modified to

$$Z_{\text{curv}}^{n+1} = Z_{\text{curv}}^n + \text{SIGN}\left\{\min\left[\omega_p \cdot |Z_{\text{curv}} - Z_{\text{curv}}^n|, p_{\text{lim}} \cdot \max(|Z_{\text{curv}}|, 0.1)\right], Z_{\text{curv}} - Z_{\text{curv}}^n\right\} \quad (4.19)$$

where $Z_{\text{curv}} = - \frac{\vec{r}_\xi \cdot \vec{r}_{\eta\eta}}{|\vec{r}_\eta|^2}$ on the top and bottom boundaries and

where $Z_{\text{curv}} = - \frac{\vec{r}_\eta \cdot \vec{r}_{\xi\xi}}{|\vec{r}_\xi|^2}$ on the left and right boundaries.

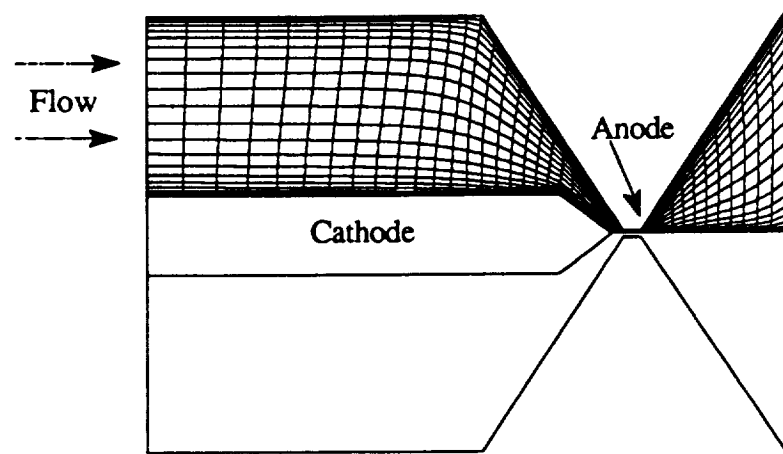
Z_{curv}^n is the value of the curvature term from the previous, or nth iteration and Z_{curv} is the currently calculated value. Thus, the value of the curvature term to be used during the current iteration, Z_{curv}^{n+1} , is damped by a combination of under-relaxing and limiting changes to a fraction of their currently calculated value. The SIGN function returns the magnitude of the first argument with the sign of the second argument. Values of $\omega_p = 0.3$ and $p_{\text{lim}} = 0.01$ were used to obtain the results which follow.

The grid generation algorithm was modified to allow the spacing of the first grid point away from the top and bottom boundaries to be fixed *a priori*. In addition, the limiting function, discussed above, was included to damp oscillations in the early stages of the solution. To aid in obtaining orthogonal grid in the interior of the region as well as at the boundary, only grids with a tighter top boundary point clustering were examined for use.

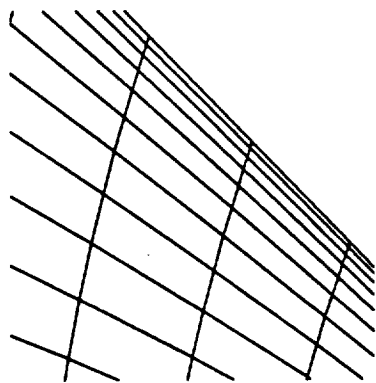
Figure 4.14 contains the results for a top boundary point distribution more tightly clustered around the nozzle than the bottom boundary point distribution. The skewed grid was eliminated in the nozzle exit by including spacing control for the first grid point near the boundary. In addition, near orthogonality was maintained at the boundary throughout the region.

Numerical grids used in the following computations are of three types. The most common grid is generated using the Poisson equation with the Thomas and Middlecoff

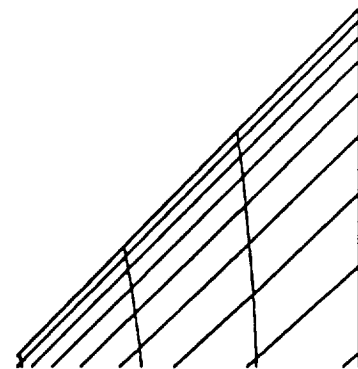
control functions and does not produce a grid orthogonal to the boundary. Comparison grids used to evaluate the effect of the numerical grid on the solution accuracy are generated using the Poisson equation with the Thompson control functions (with or without spacing control) and do produce a grid orthogonal to the boundary. Either the grid used will be displayed or the method used to generate the grid will be mentioned.



(a)



(b)



(c)

Figure 4.14 Modified control functions with spacing control grid distributions for an arcjet thruster geometry, different point distributions on top and bottom boundaries, (a) entire thruster, magnified views of (b) upstream nozzle wall and (c) nozzle exit

Results and Discussion

5.1 Introduction

In this chapter the algorithm used to solve the Thin Layer Navier-Stokes equations in transformed coordinates will be validated by comparing numerical predictions with experimental data. Available experimental results include Mach contours, wall static pressure ratios, centerline Mach number distributions, and integral parameters.

Predicted results will illustrate the effects of geometry, viscosity, and swirl on the nozzle performance. The important geometries that must be accurately modeled include large area ratio nozzles (both inlet-to-throat and exit-to-throat area ratios) and nozzles with centerbodies. Combining these geometric effects with viscosity and swirl will enable swirling flow in arcjet thrusters to be examined.

Six nozzle geometries are examined. The first two nozzles were originally examined by Dutton [40, 41]. 1. *Dutton's initial nozzle* will illustrate the effects of viscosity and inlet swirl velocity profiles (Fig. 5.1) on nozzle performance parameters and Mach contours. 2. *Dutton's experimental nozzle* will demonstrate the effect of viscosity and inlet total pressure and swirl velocity profiles on static wall pressures, Mach contours, and nozzle swirl velocity profiles. 3. *Back & Cuffel's nozzle* [49-51] clearly illustrates a reflected oblique shock caused by the wall geometry. 4. An *annular nozzle* will show the effect of a viscous boundary layer and highly swirled flow in a nozzle containing a centerbody. 5. A *100:1 area ratio nozzle* containing a thick boundary layer will then be examined. 6. A converging-diverging nozzle containing a centerbody will be used to illustrate viscous, swirling flow through an *arcjet thruster geometry*.

5.2 Previous Numerical Research

Early work in swirling flow was limited by the analysis approach chosen, quasi-one-dimensional [52] for example, or the use of a single level of swirl [53]. Later work examining swirling flow in annular nozzles [54, 55] showed the presence of swirl decreases the discharge coefficient, thrust, and vacuum specific impulse of a nozzle.

Dutton's [40, 41] work in inviscid swirling flow used an explicit finite difference technique. Converging, converging-diverging, and annular nozzles were examined. The effects of three different inlet swirl velocity profiles on integral parameters were

determined. The results showed the degradation in performance due to swirl. A series of experiments were also conducted to compare measured and numerically predicted wall static pressures in a second converging-diverging nozzle. The numerical results showed excellent agreement with the experiments except in a region just downstream of the throat. As will be demonstrated shortly (see Section 5.4.2 entitled *Dutton's experimental nozzle*) the discrepancy was caused by the absence of viscosity.

In all of the numerical investigations mentioned above, the flow was assumed to be inviscid. Chang [39, 42] was the first to examine viscous swirling flow in the three nozzle geometries used by Dutton. An implicit ADI technique was used in transonic regions. To eliminate numerical instabilities in the central-differenced ADI procedure in regions where the flowfield is predominantly supersonic, the procedure had to be modified. This modification was accomplished by retaining the central differencing in the cross-stream direction and flux-vector splitting in the streamwise direction.

In a low Reynolds number flow, such as those found in arcjets [7], viscous effects cannot be neglected because of the large growth of the boundary layer in the nozzle exit [56]. A robust and efficient numerical technique must be used to solve the resulting governing equations. The present study was conducted in order to develop an efficient method of assessing the effects of viscous swirling flow in these nozzles.

5.3 Nozzle Performance Parameters

Several integral parameters will be used in assessing the effect of swirl on nozzle flows. The discharge coefficient, C_D , defined as

$$C_D \equiv \frac{\dot{m}}{\dot{m}_{id}} = \frac{2 \int_{r_c}^{r_w} \rho u r dr}{(r_{wt}^2 - r_{ct}^2)(\rho^* u^*)_{id}} \quad (5.1)$$

is a measure of the decrease in mass flow rate due to flow geometry and swirl. The vacuum stream thrust efficiency, η_{vs} , is defined as

$$\eta_{vs} \equiv \frac{T}{T_{id}} = \frac{2 \int_{r_{ce}}^{r_{we}} (P + \rho u^2) r dr}{(r_{we}^2 - r_{ce}^2)(P_e + \rho_e u_e^2)_{id}} \quad (5.2)$$

the specific impulse efficiency, η_{SI} , is a combination of the above two parameters and is defined

$$\eta_{SI} \equiv \frac{(T/\dot{m})}{(T/\dot{m})_{id}} = \frac{\eta_{vs}}{C_D} \quad (5.3)$$

Finally the nozzle inlet swirl number, S_i , is defined as

$$S_i \equiv \frac{\int_{r_{ci}}^{r_{wi}} \rho u w r^2 dr}{r_{wi} \int_{r_{ci}}^{r_{wi}} \rho u^2 r dr} \quad (5.4)$$

and is the axial flux of angular momentum divided by the inlet wall radius times the axial flux of axial momentum. It is a direct measure of the level of swirl at the nozzle inlet.

The integral parameters defined above are non-dimensional by default. The values cited later for thrust and mass flow rate are also non-dimensional by virtue of being calculated with non-dimensional values of density, velocity, etc.

5.4 Computations and Comparisons for a Variety of Nozzles

A few words are needed regarding the conditions used to obtain the results in Sections 5.4.1-5.4.6. As discussed in Section 3.3.2.2, the inlet boundary conditions specified at the subsonic inlet include the ratio of swirling velocity to axial velocity, $\phi = w/u$, stagnation pressure, P_t , stagnation temperature, T_t , and the ratio of radial velocity to axial velocity, $\theta = v/u$. The radial velocity is always set equal to zero ($\theta = v/u = 0.0$) and unless otherwise stated the stagnation pressure and temperature are set equal to one. The remaining boundary condition for the swirl velocity component, w , is set equal to zero ($\phi = w/u = 0.0$) in the case of unswirled flow. The same inlet swirling velocity profiles used by Dutton, as shown in Fig. 5.1, are used for swirling flow cases here, except the swirl angle asymptotically approaches zero at the wall in all viscous calculations.

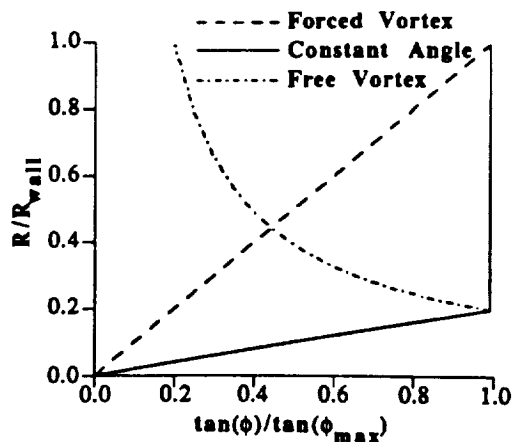


Figure 5.1 Inlet swirl velocity boundary condition profiles

A linear forced vortex profile has been assumed near the centerline for the constant angle and free vortex profiles to enforce the centerline boundary condition $w=0$. The non-dimensional radius ratio of $R/R_{\text{wall}}=0.2$ was chosen as the matching point by Dutton because it was typical of geometries he examined.

In all nozzles a constant specific heat of $\gamma_0=1.4$ was assumed and Sutherland's formula [27] was used for the viscosity (constants were for air).

5.4.1 Dutton's Initial Nozzle

The 35°-18.5° converging-diverging nozzle initially examined by Dutton [40, 41] has an exit-to-throat area ratio of 2.56. Two different numerical grids were used to examine the flowfield and are shown in Fig. 5.2. The grid used for the inviscid flow case had 45 equally spaced grid points in the axial and 30 equally spaced grid points in the radial direction. From here on this will be written 45 x 30 grid points (axial x radial). The grid used for the viscous flow case had substantial clustering near the wall and contained 45 x 40 grid points.

Figures 5.3 and 5.4 illustrate the inviscid and viscous ($Re=10,000$) Mach contours for both unswirled and swirling (30° constant angle profile) flows. The inviscid contours agree well with Dutton's results and the viscous contours agree well with Chang's results [42]. The main effect of swirl is to shift the centerline Mach contours upstream which in turn decreases the mass flow rate (see Table 5.1). A thin boundary layer can be seen along the wall in both viscous cases.

The increased swirling centerline Mach contour is due to an increase in the axial velocity near the centerline in swirling flow. The increase in axial velocity causes a decrease in the pressure (Bernoulli effect). The numerical results show the static temperature is essentially constant across the nozzle inlet for both unswirled and swirling flows and only drops a few percent in swirling flow. This combination of falling pressure and constant temperature lead to a drop in the gas density. The drop in density is significant across the nozzle inlet and leads to the decreased mass flow rate.

These effects are illustrated in Fig. 5.5 for the inviscid Mach contours shown in Fig. 5.3. The increase in axial velocity due to swirl is confined to a region less than 40% of the nozzle radius. However, the decrease in density due to swirl is much larger over a larger portion of the nozzle radius and hence leads to the decrease in mass flow rate shown in Table 5.1.

It should also be noted that the converged numerical solutions, in both unswirled and swirling flows, exhibit an inlet axial velocity decreasing with increasing radius as shown in Fig. 5.5. Thus, the swirl velocity component for a constant angle inlet swirl boundary condition will not be constant in the outer portions of the nozzle inlet but will decrease proportional to the inlet axial velocity.

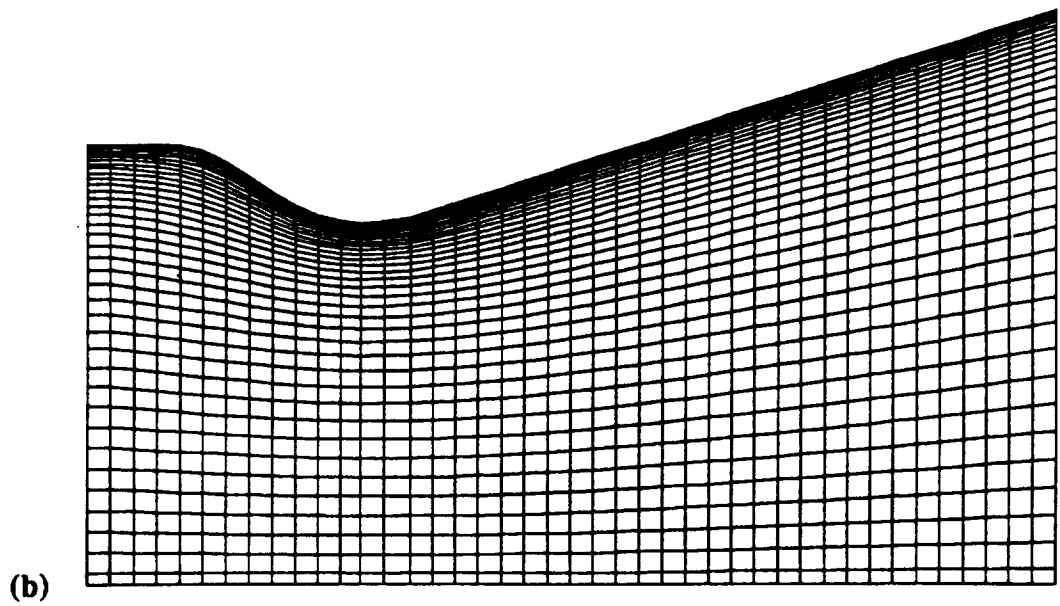
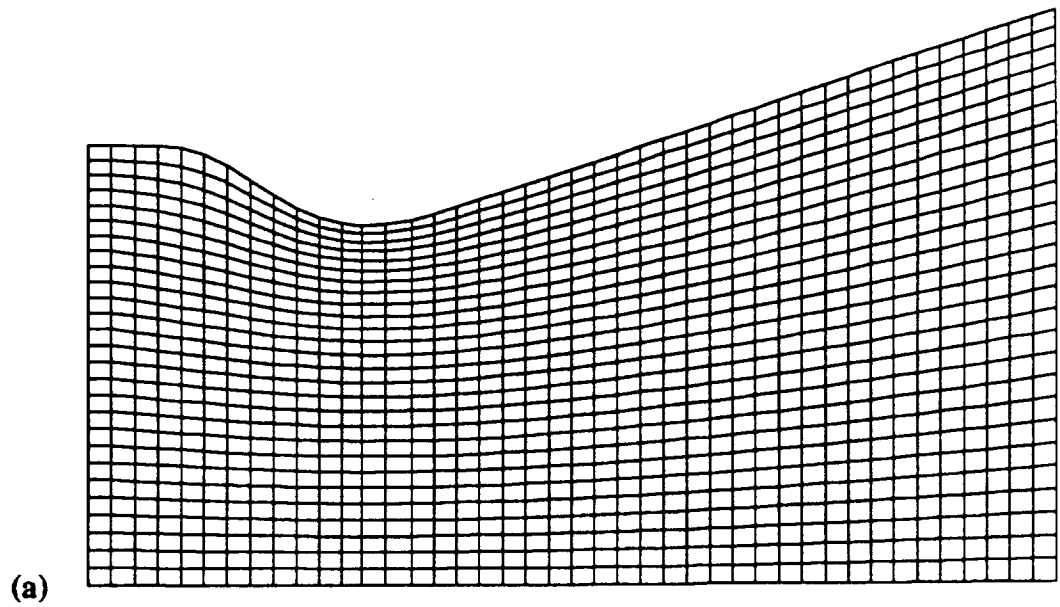
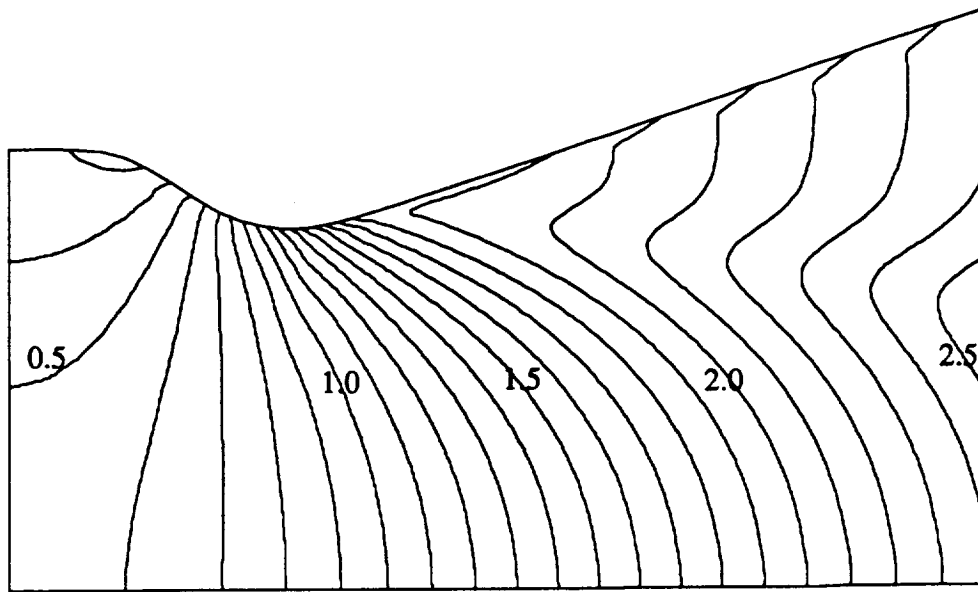
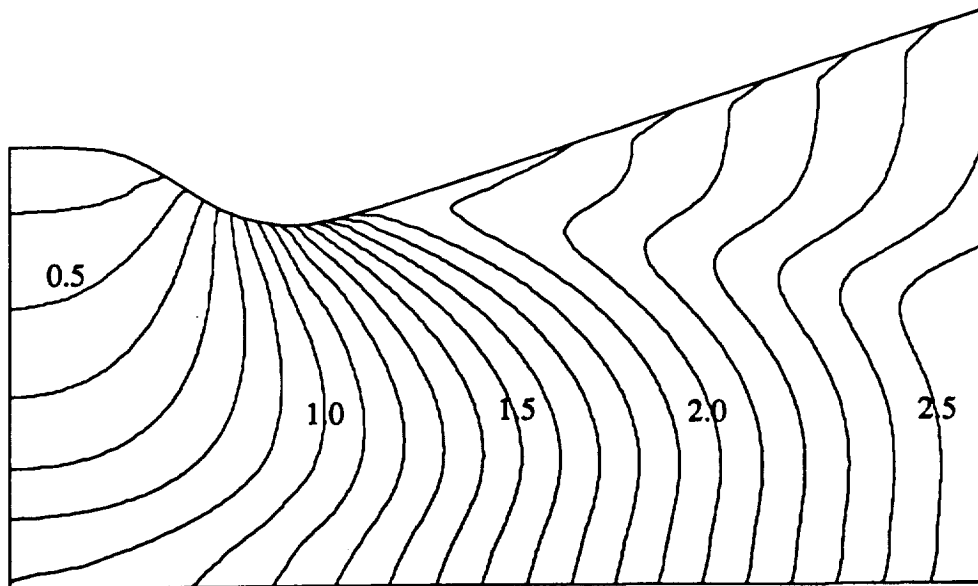


Figure 5.2 **Grid for Dutton's initial nozzle (DIN), (a) inviscid, 45 x 30, (b) viscous, 45 x 40**



(a)



(b)

Figure 5.3 Inviscid Mach contours in DIN, (a) unswirled flow, (b) 30° constant angle swirl boundary condition

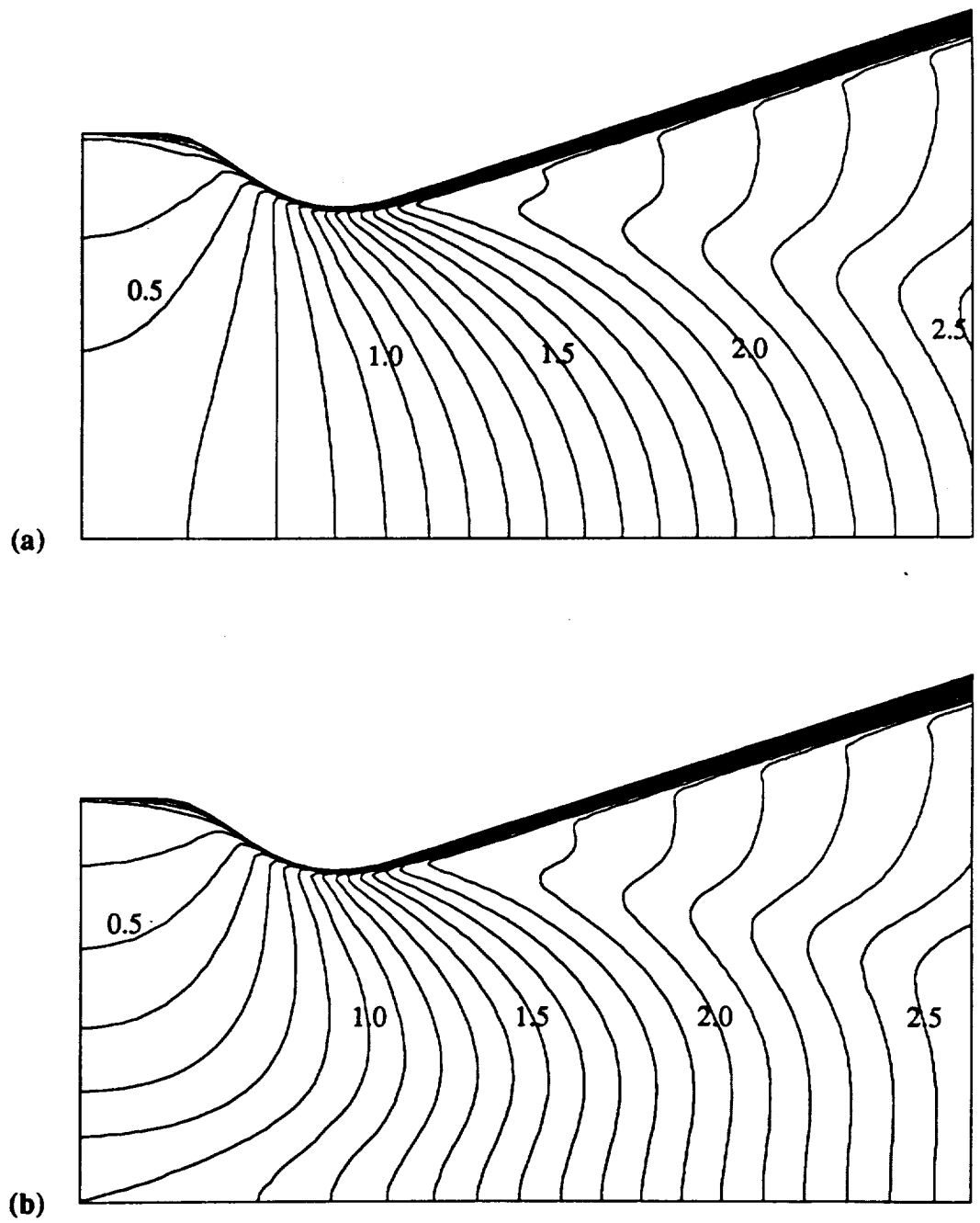


Figure 5.4 Viscous Mach contours in DIN ($Re = 10,000$),
(a) unswirled flow, (b) 30° constant angle swirl

**Table 5.1 Nozzle performance summary for Dutton's
initial nozzle**

Figure	Re	Grid	Swirl	C _D	η_{vs}	η_{SI}	S _i	Thrust	Mass Flow Rate
5.3a	∞	45 x 30	—	0.980	0.938	0.957	0.0	4.48	2.49
5.3b	∞	45 x 30	30° Cst Angle	0.942	0.901	0.957	0.320	4.31	2.39
—	∞	45 x 40	—	0.981	0.938	0.956	0.0	4.48	2.49
—	∞	45 x 40	30° Cst Angle	0.942	0.901	0.957	0.324	4.30	2.40
5.4a	10,000	45 x 40	—	0.969	0.925	0.955	0.0	4.42	2.46
5.4b	10,000	45 x 40	30° Cst Angle	0.931	0.889	0.955	0.321	4.25	2.37
5.6a	10,000	45 x 40	52.5° Forced Vortex	0.911	0.869	0.955	0.423	4.15	2.31
5.6b	10,000	45 x 40	40° Free Vortex	0.949	0.906	0.955	0.160	4.33	2.42

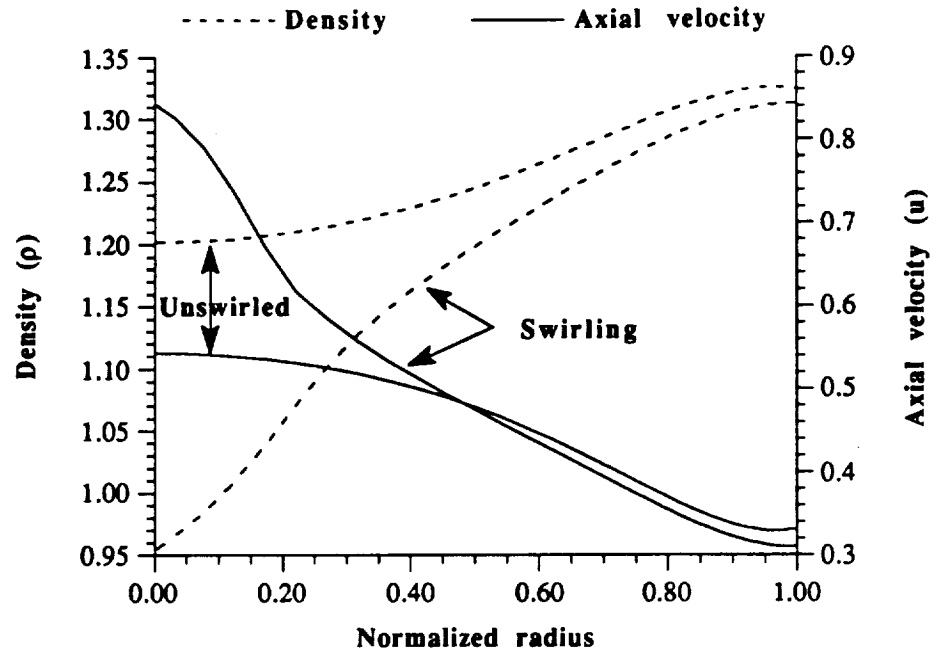


Figure 5.5 Comparison of inviscid unswirled and swirling (30° constant angle) nozzle inlet density and axial velocity profiles in DIN

Two additional inlet swirl cases were also examined. The viscous ($Re = 10,000$) Mach contours for a 52.5° forced vortex and a 40° free vortex are shown in Fig. 5.6. Again the Mach contours, in the inviscid regions of the flow, agree well with Dutton's results (Chang did not show any results for these cases). The resulting discharge coefficients, mass flow rates, etc. are included in Table 5.1. Examination of Table 5.1 reveals viscous effects and swirl decrease the mass flow rate and hence the thrust in a converging-diverging nozzle. The C_D and η_{vs} also are smaller for the viscous and swirling flow cases while η_{SI} remains constant. Dutton observed the same trends for inviscid, swirling flow.

The swirl velocity profiles at the inlet, throat, and exit planes for the constant angle, forced vortex, and free vortex inlet swirl flows are shown in Figs. 5.7-5.8. The maximum throat swirl velocity for each case was used to normalize the swirl velocity. The form of the inlet swirl profile is clearly maintained throughout the nozzles. The decay of the swirl velocity in the boundary layer is also evident near the wall in the viscous cases.

A constant angle inlet swirl profile produces the largest amount of swirl at the inlet for a given maximum swirl angle, i.e., ϕ_{\max} , (see Figure 5.9). Consequently, the largest reduction in mass flow rate, which occurs for the highest amount of swirl, occurs for a constant angle inlet profile. Figure 5.10 illustrates the reduction in mass flow rate for a given ϕ_{\max} , by non-dimensionalizing all mass flow rates with the unswirled, viscous mass flow rate from Table 5.1. The free and forced vortex inlet swirl velocity profiles would require a much larger ϕ_{\max} to have as noticeable an effect as the constant angle profile. At a ϕ_{\max} of 30 degrees the constant angle inlet profile mass flow rate decreases 4% compared to the unswirled case. The free and forced vortex profiles cause approximately a 1% decrease in mass flow rate at a ϕ_{\max} of 30 degrees. Therefore, when other nozzles are examined later in this study, only the effects of constant angle inlet swirl profiles will be illustrated.

Figure 5.11 compares C_D and η_{vs} using Dutton's inviscid results and the present viscous results. At a Reynolds number of 10,000 C_D decreases 1% and η_{vs} decreases approximately 2% from the inviscid result. Dutton observed a constant value of $\eta_{SI}=0.971$. The present results also showed η_{SI} to be constant with values of 0.957 and 0.955 for inviscid and viscous ($Re=10,000$) flows, respectively.

Figure 5.12 illustrates the effect of viscosity on C_D and η_{vs} for unswirled and swirling flow. As the Reynolds number increases and viscosity decreases C_D and η_{vs} approach their inviscid limits.

Convergence histories are displayed in Fig. 5.13 which were obtained as a function of viscosity and the inlet swirl condition using the inviscid and viscous grids shown in Fig. 5.2. The norm of the residual is defined as $\sum_{ii,i} \left(\delta \vec{Q} / \vec{Q} \right)$ where ii represents the five conserved quantities shown in Eq. (2.49). Grid density slows the convergence rate the most. Including viscous effects in the computations slows the convergence rate by a smaller amount. Swirl has little or no effect on the convergence rate.

Mass conservation through the nozzle, corresponding to the 300th iteration of the convergence history cases just discussed, is shown in Fig. 5.14. Mass conservation is almost identical in all six cases and has a maximum error of approximately $\pm 0.6\%$. In all of the nozzles examined in this study mass flow, being an integral parameter, typically reached its steady-state value by the time the residual had dropped approximately four orders of magnitude. Contours of nozzle properties are virtually unchanged after the four order drop in residual has occurred with changes in properties occurring in the third or fourth significant figure. Thus, these mass conservation trends are typical for the nozzles examined in this study.

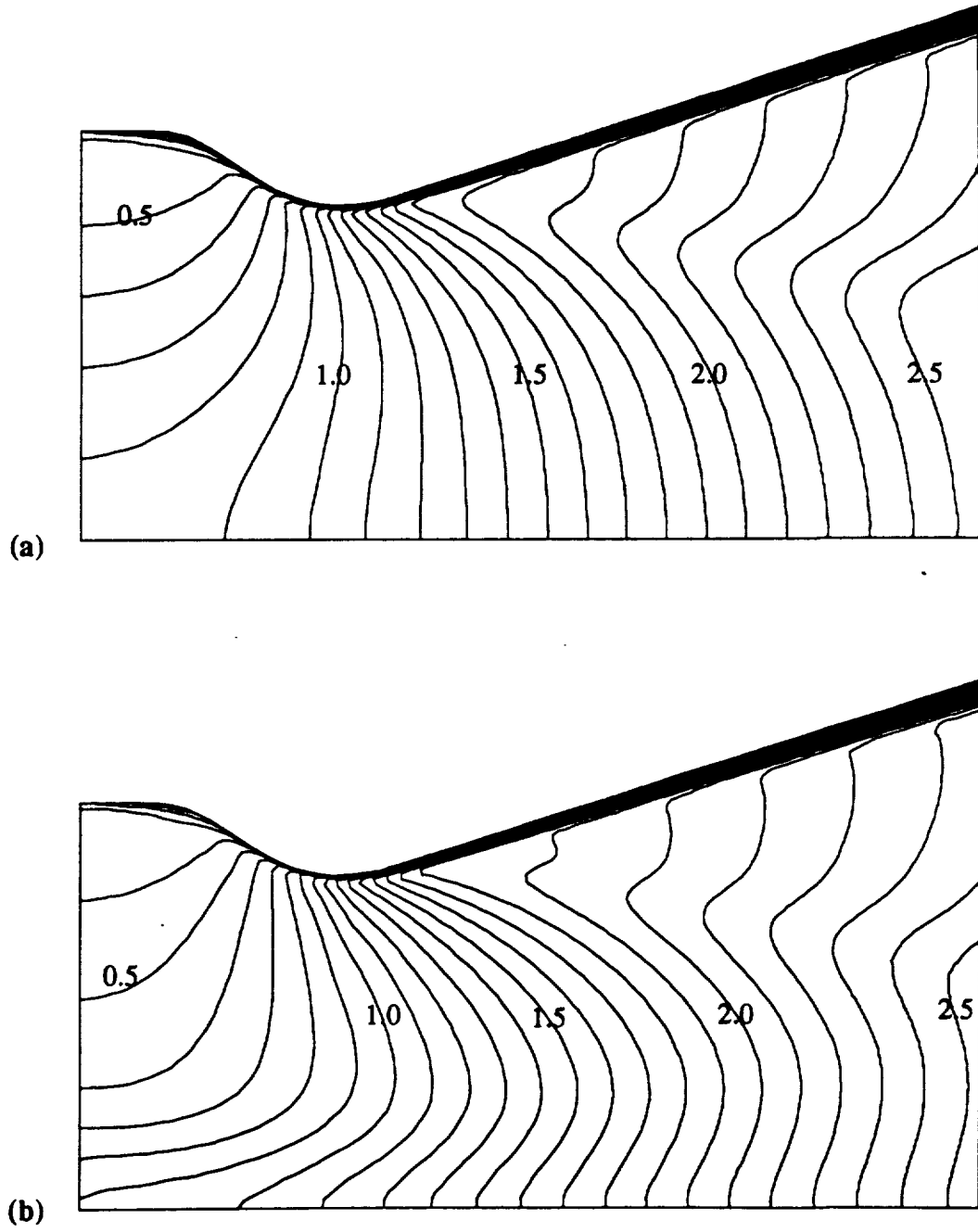
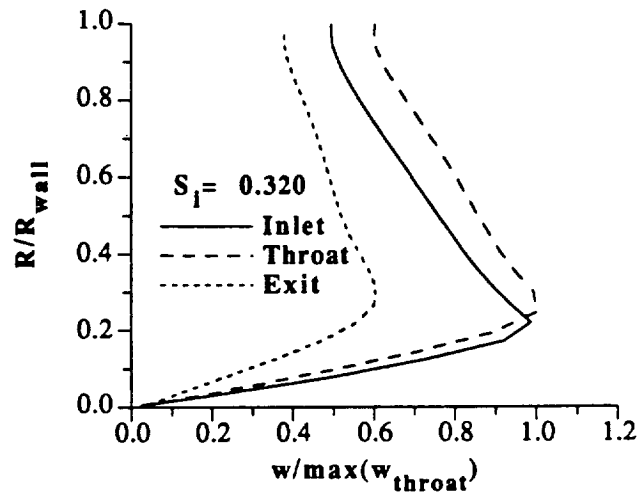
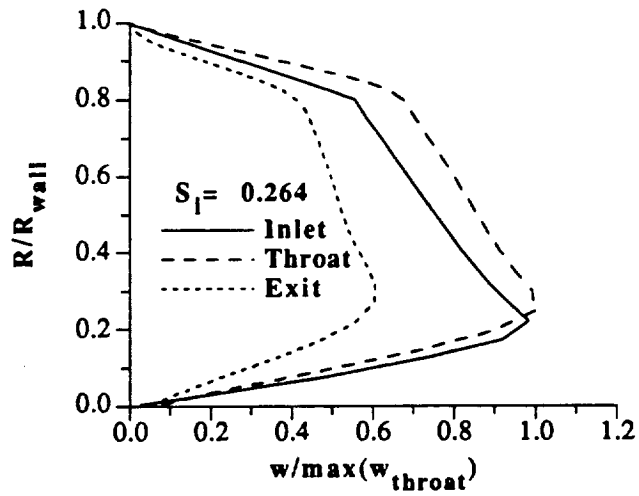


Figure 5.6 Viscous Mach contours in DIN ($Re = 10,000$),
(a) 52.5° forced vortex, (b) 40° free vortex

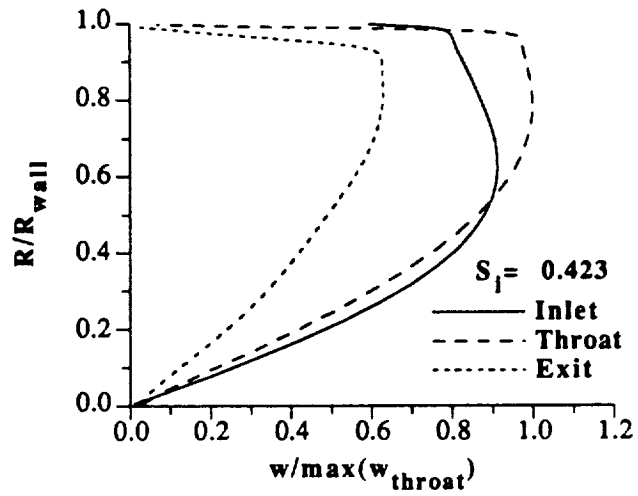


(a)

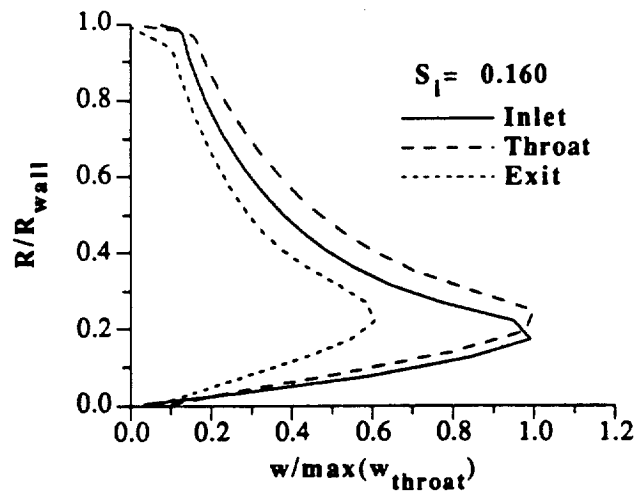


(b)

Figure 5.7 Swirl velocity profiles at the inlet, throat, and exit for a 30° constant angle inlet profile in DIN, (a) inviscid, (b) viscous ($Re = 10,000$) flow



(a)



(b)

Figure 5.8

Swirl velocity profiles at the inlet, throat, and exit in DIN for a (a) 52.5° forced vortex, (b) 40° free vortex inlet profile in viscous flow ($Re = 10,000$)

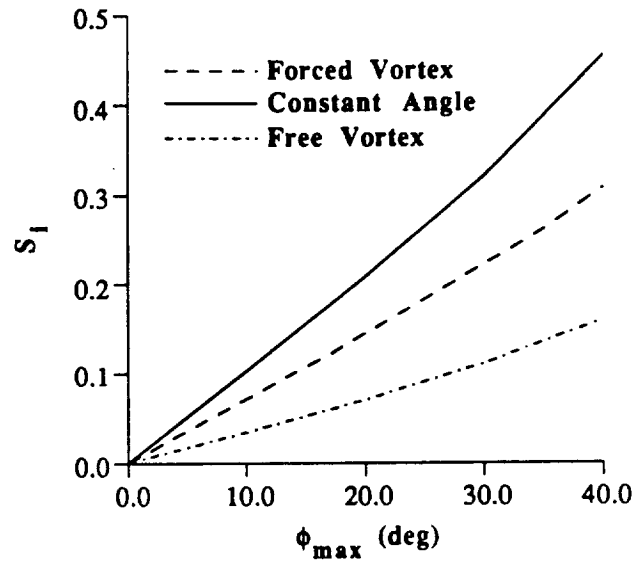


Figure 5.9 Dependence of inlet swirl number in DIN on inlet swirl profile and maximum inlet swirl angle in viscous flow ($Re= 10,000$)

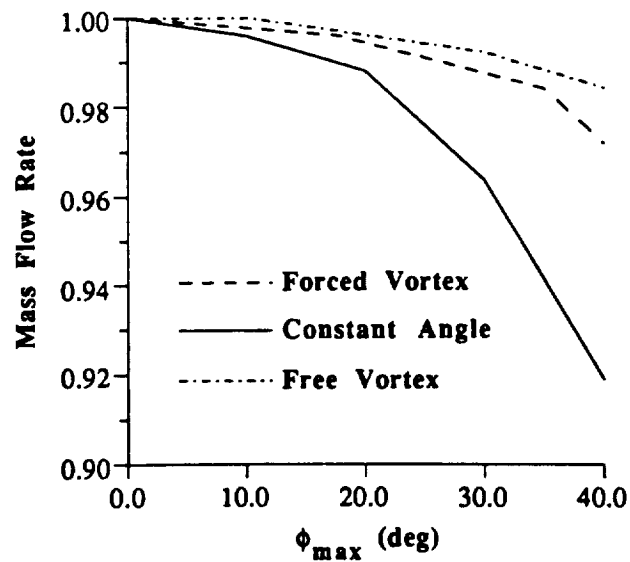


Figure 5.10 Non-dimensionalized mass flow rate in DIN for a given inlet swirl profile and maximum inlet swirl angle in viscous flow ($Re= 10,000$)

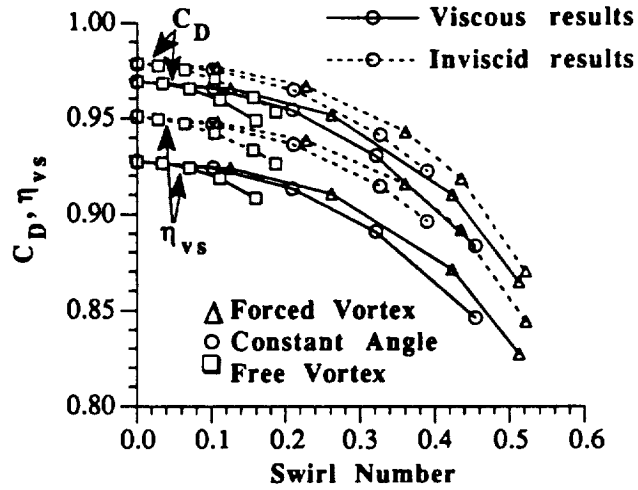


Figure 5.11 Dependence of nozzle performance in DIN on inlet swirl number and viscosity ($Re= 10,000$)

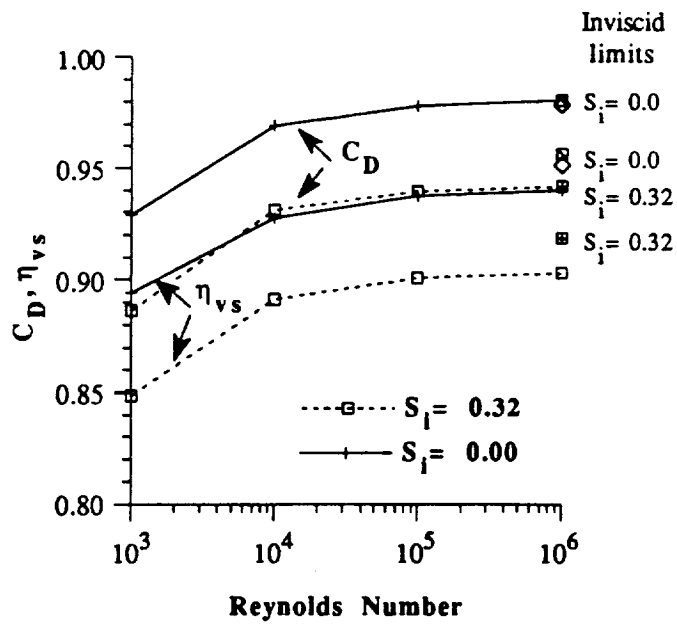


Figure 5.12 Dependence of nozzle performance in DIN on inlet swirl number and Reynolds number (30° constant angle)

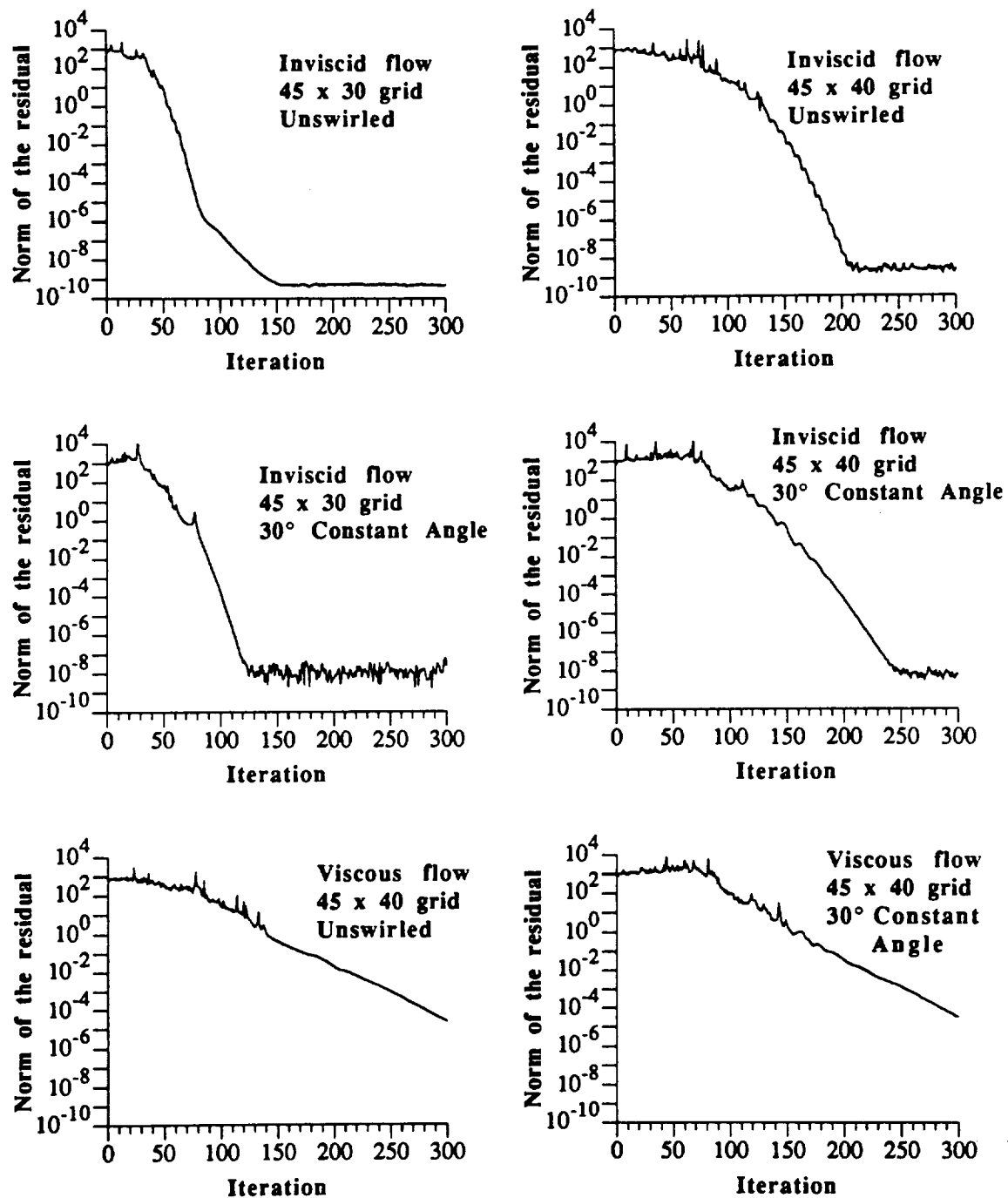


Figure 5.13 Convergence in DIN as a function of viscosity, grid size, and swirl ($Re = 10,000$ in viscous flow)

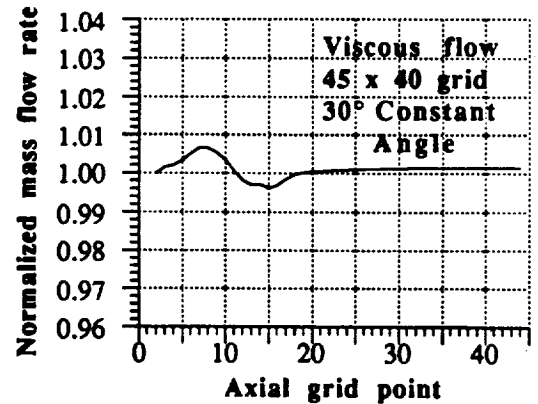
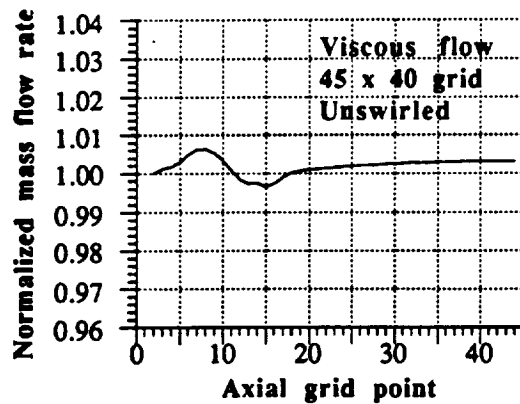
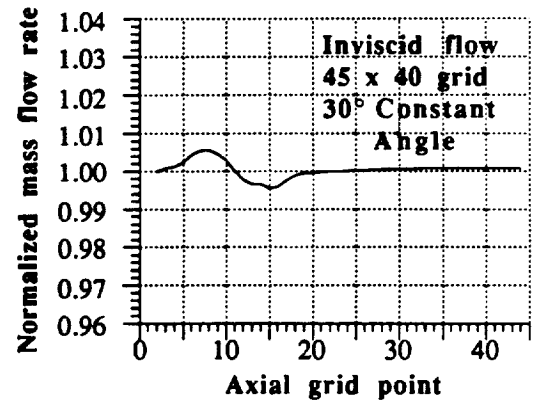
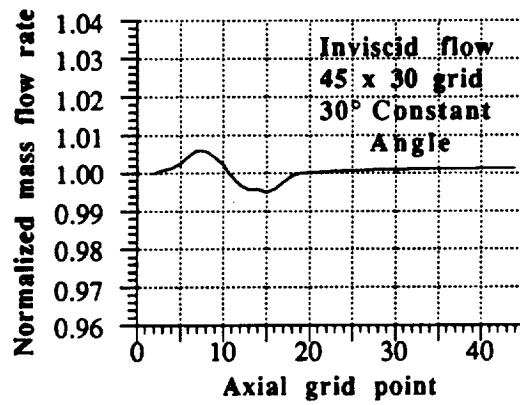
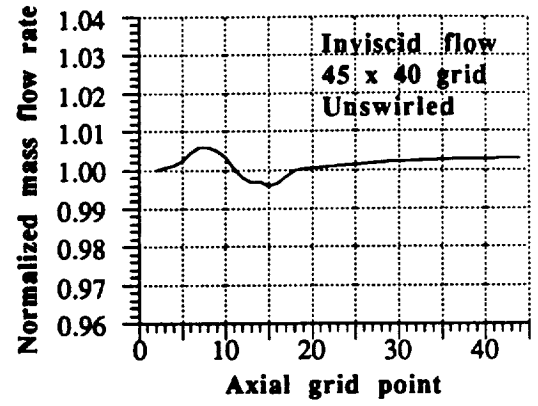
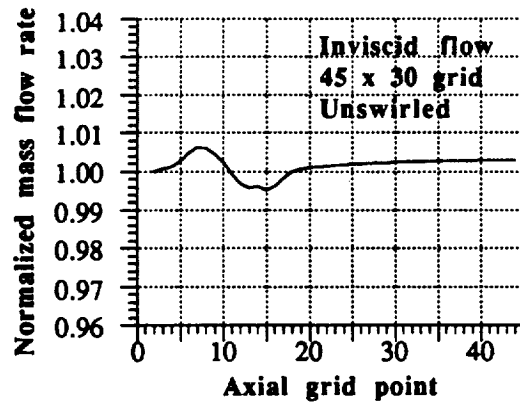


Figure 5.14 Mass conservation in DIN (axial mass flow rate divided by inlet mass flow rate, $Re = 10,000$ if viscous flow)

5.4.2 Dutton's experimental nozzle

Dutton [40,41] also examined a second converging-diverging nozzle both experimentally and numerically. The 35°-18.5° nozzle has an exit-to-throat area ratio of 2.56. A 50 x 40 grid, see Fig. 5.15a, clustered near the wall was used in the present study to obtain the following viscous results. Dutton's measurements included inlet stagnation pressures, swirl velocity profiles as well as static wall pressures. The measured distribution of stagnation pressure (see Fig. 5.15b) and closest fit to the forced vortex, constant angle, or free vortex swirl profiles described previously were used as inlet boundary conditions. Mass flow errors in the present study were less than 1% and the total residual dropped four orders of magnitude in 250 steps.

Shown in Fig. 5.16a are the Mach contours for unswirled viscous flow. Figure 5.16b compares the experimental static wall pressure data for unswirled flow with the predicted inviscid and viscous ($Re = 10,000$) results. The present inviscid results are essentially the same as Dutton's inviscid results, which show a slight dip in the predicted static wall pressure downstream of the throat. However, the beginning of the viscous boundary layer just downstream of the throat causes the viscous static wall pressure to almost exactly follow the experimental data.

Figures 5.17 and 5.18 contain the Mach contours and static wall pressure distributions for two viscous ($Re = 10,000$) swirling flow cases. The inlet swirl velocity profile for Fig. 5.17 which most closely matched Dutton's experimental inlet swirl data was a 40° forced vortex profile. A 50° constant angle profile was used in Fig. 5.18 to match Dutton's second set of inlet swirl data. The swirl velocity profiles at the inlet, throat, and exit planes for the forced vortex and constant angle inlet profiles are shown in Fig. 5.19. The maximum throat swirl velocity for each case was used to normalize the swirl velocity. The form of the inlet swirl profile is maintained throughout the nozzle and the decay of the velocity is clear in the boundary layer.

In both swirling flow cases the inviscid results may be seen to underpredict the static wall pressure distributions downstream of the throat while the viscous result shows excellent agreement with the data. It should be noted that downstream of an axial location of approximately $z = -0.5$, the measured static wall pressure distributions for all three flow cases are essentially identical. Thus, the measured inlet stagnation pressure distribution has a large effect only in the inlet region where the swirl velocity is highest.

The values of C_D , η_{vs} , and η_{SI} shown in Table 5.2 are 1-2% lower than Dutton's reported values, exhibiting the degradation of performance due to viscosity.

Comparing Tables 5.1 and 5.2 one sees the values of S_i for the forced vortex and constant angle cases are of the same order of magnitude for Dutton's initial and experimental nozzles. However, the Mach contours (Figs. 5.6a, 5.17a and Figs. 5.4b, 5.18a, respectively) are much different in the inlet portions of the nozzle. The nozzles have

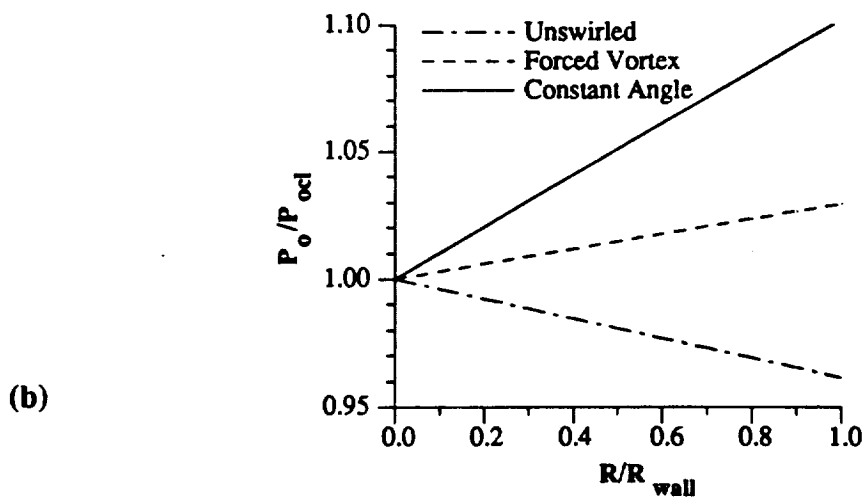
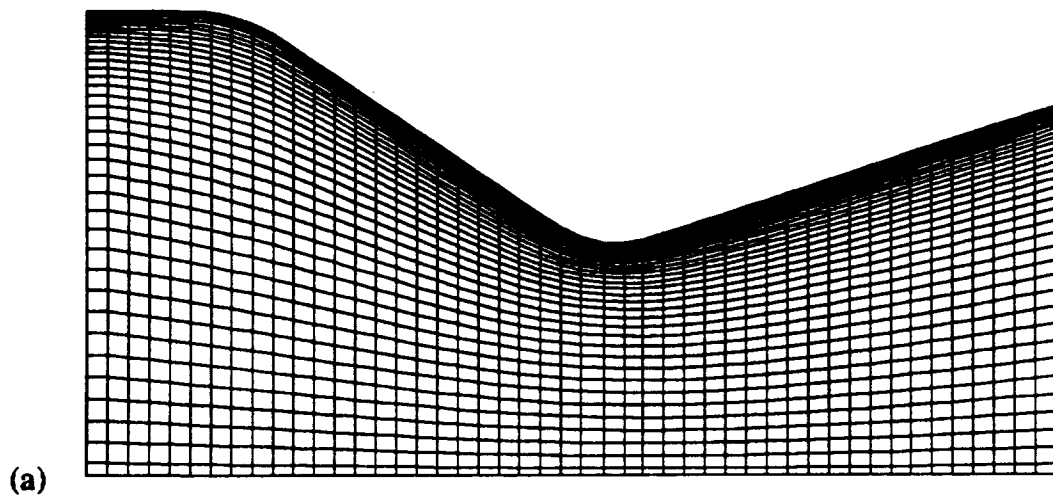


Figure 5.15

(a) Viscous grid in Dutton's experimental nozzle (DEN) (50 x 40) and (b) inlet stagnation pressure profiles for Dutton's experimental nozzle

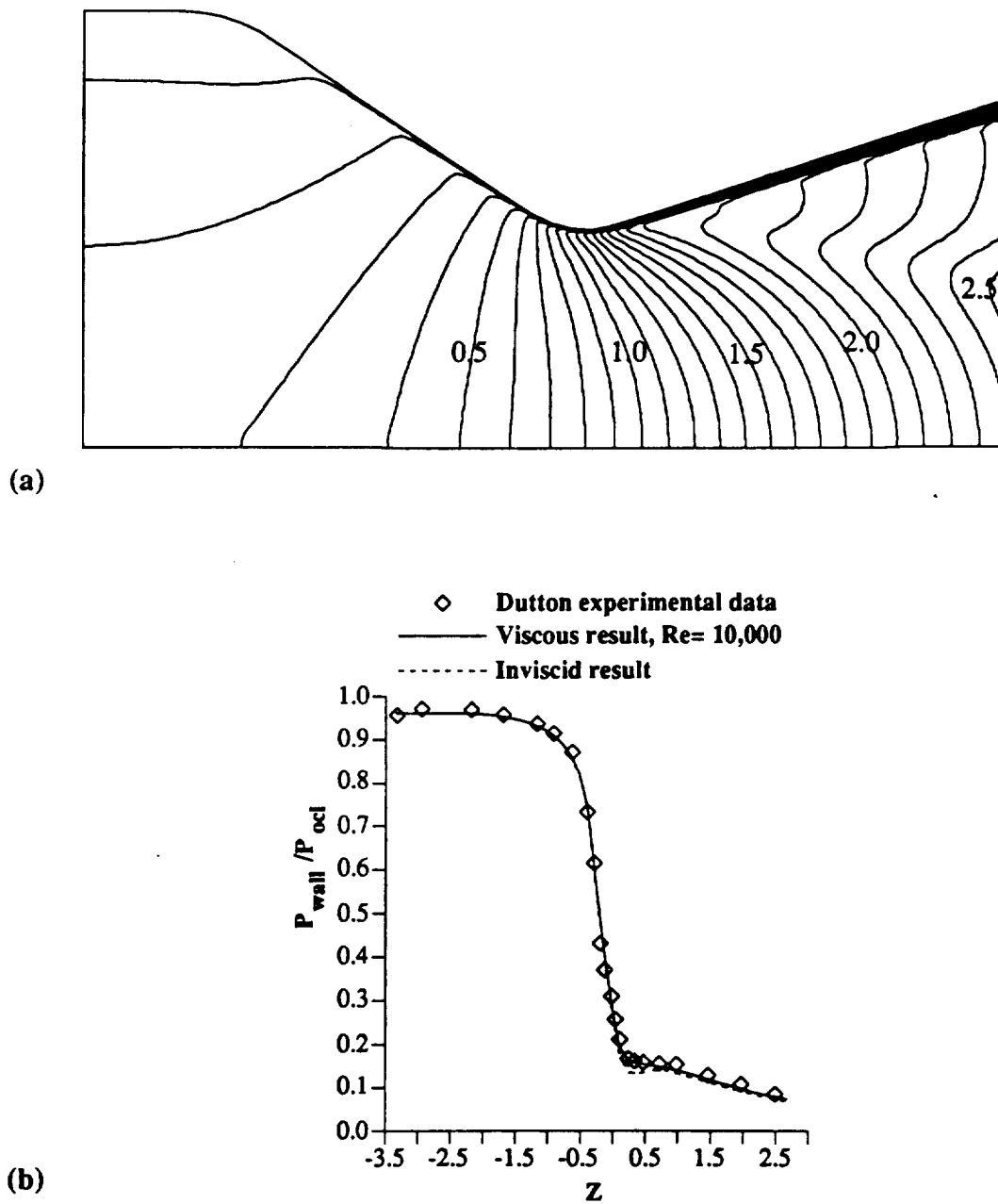


Figure 5.16

Viscous results for a 40° forced vortex inlet swirl profile in DEN, (a) Mach contours, (b) comparison of experimental and numerical static wall pressure distributions ($Re = 10,000$)

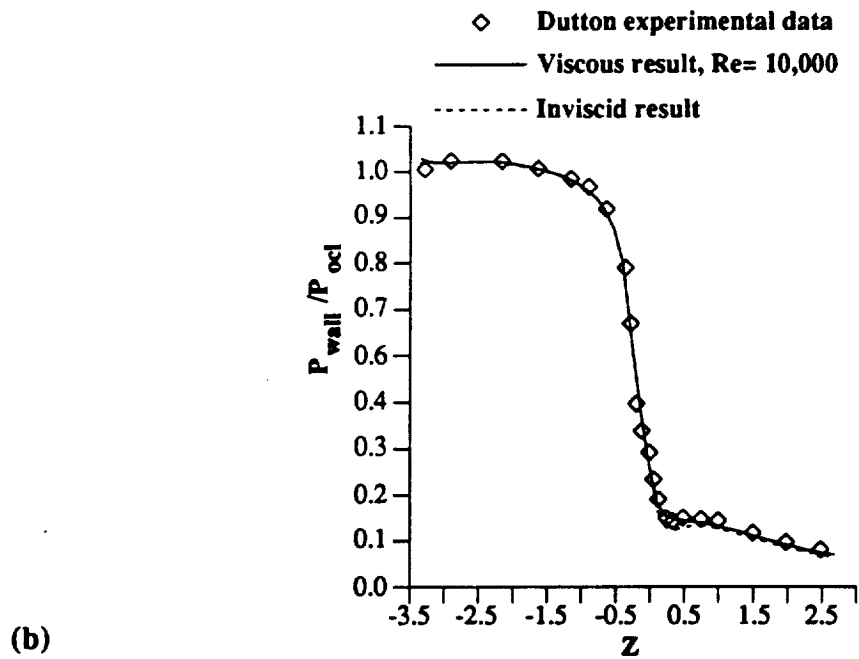
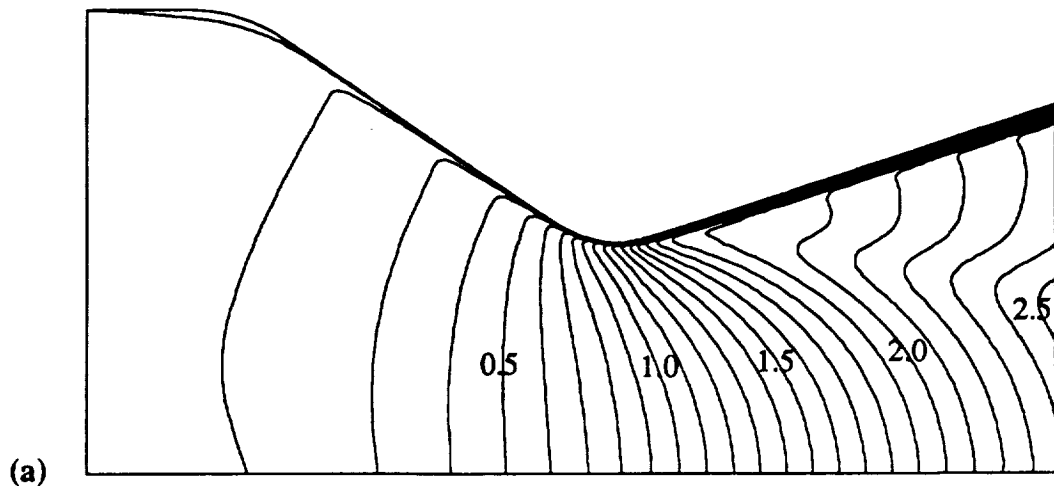


Figure 5.17

Viscous results for a 50° constant angle inlet swirl profile in DEN, (a) Mach contours, (b) comparison of experimental and numerical static wall pressure distributions ($Re = 10,000$)

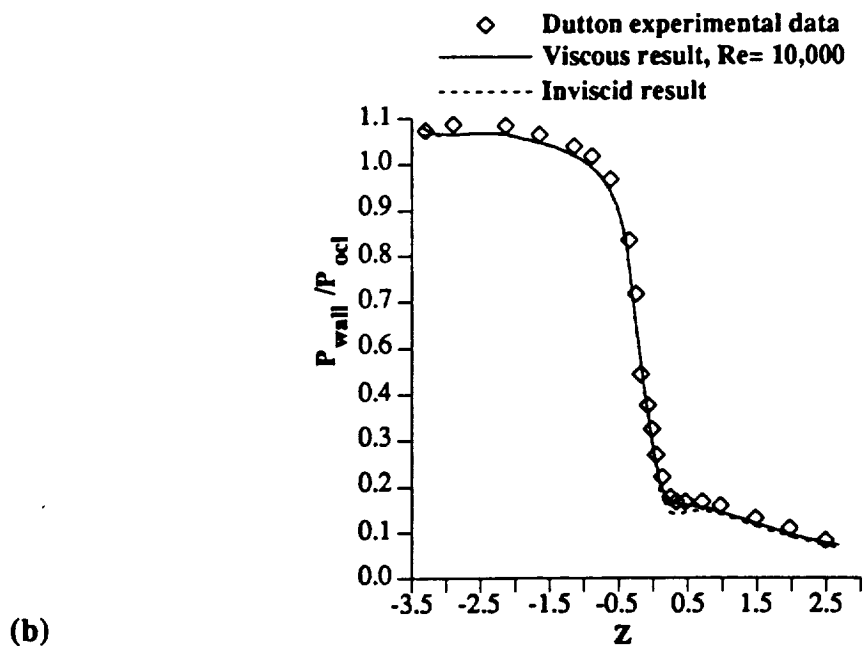
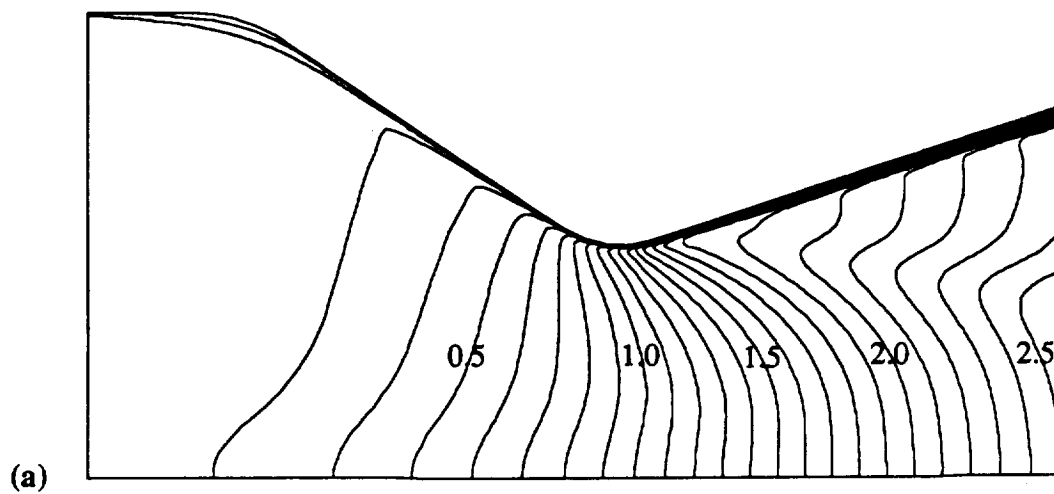
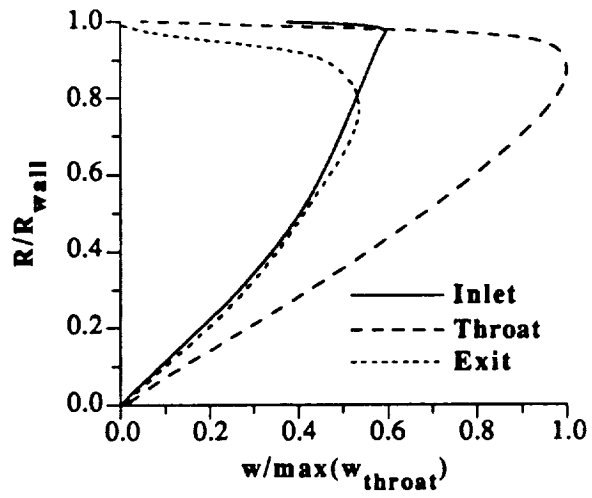


Figure 5.18 Viscous results for a 40° forced vortex inlet swirl profile in DEN, (a) Mach contours, (b) comparison of experimental and numerical static wall pressure distributions (Re= 10,000)



(a)

(b)

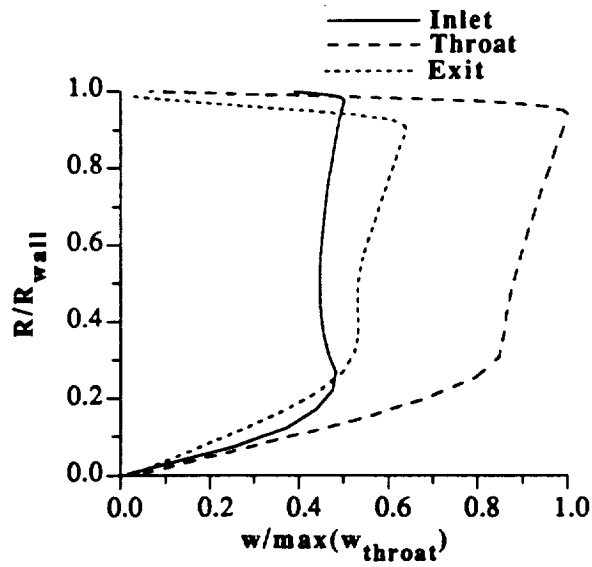


Figure 5.19 Swirl velocity profiles at the inlet, throat, and exit in DEN for a (a) 40° forced vortex, (b) 50° constant angle inlet profile in viscous flow ($Re=10,000$)

Table 5.2 **Nozzle performance summary for Dutton's experimental nozzle**

Figure	Re	Grid	Swirl	C_D	η_{vs}	η_{SI}	S_i	Thrust	Mass Flow Rate
5.16	10,000	50 x 40	—	0.966	0.918	0.950	0.0	4.32	2.40
5.17	10,000	50 x 40	40° Forced Vortex	0.957	0.910	0.951	0.355	4.44	2.47
5.18	10,000	50 x 40	50° Cst Angle	0.935	0.888	0.950	0.766	4.48	2.49

the same exit-to-throat area ratios of 2.56 but vastly different inlet-to-throat area ratios: initial nozzle= 1.5 and experimental nozzle= 4.0. In a large inlet-to-throat area ratio nozzle the inlet axial velocity will be low, approaching stagnation conditions, making it easy to achieve a high ratio of swirl to axial velocity, w/u , and hence a large inlet swirl value, S_i . While the ratio may be high the absolute magnitude of w is small causing little effect on the centerline axial velocity distribution or Mach contours in the inlet region.

Comparing the Mach contours between the two nozzle geometries downstream of the throat reveals few differences. Since the throat area is much smaller than the inlet area the throat axial velocity is very high as the flow accelerates in the converging portion of the nozzle. Due to the exit boundary conditions the flow continues to accelerate in the diverging portion of the nozzle where the axial velocity component dwarfs the swirling velocity component. Due to conservation of angular momentum, the swirl velocity component is highest at the throat (smallest area) and lower as the area increases (see Figs. 5.7 and 5.19). Thus, the swirl velocity in the diverging portion of the nozzle has a much lower magnitude than the axial velocity and consequently has a small effect of the Mach contours.

Also worth noting in Table 5.2 is the increase in mass flow rate in the two swirled cases over the unswirled case. Typically swirl decreases the mass flow rate. However, the measured inlet stagnation pressure profiles, Fig. 5.15b, were used as boundary conditions for the unswirled and swirled cases. The swirled inlet stagnation pressures were higher than the unswirled case and more than offset the decrease in mass flow rate due to swirl for an overall increase in mass flow rate.

5.4.3 Back and Cuffel nozzle

Back and Cuffel [49-51] performed a detailed series of measurements on a variety of converging-diverging nozzles. In one of the nozzles, the exit length was of sufficient length for an oblique shock to coalesce and reflect from the nozzle centerline. A 60×40 grid (Fig. 5.20a) clustered near the wall was used to obtain the following viscous results for this nozzle (hereafter referred to as the B&C nozzle). The nozzle exit-to-throat and inlet-to-throat area ratios are 9.75 and 6.55, respectively.

Figure 5.20b shows the Mach contours for a viscous flow with a Reynolds number of 10,000. These results were obtained for the nozzle examined experimentally by B&C. A growing boundary layer is visible along the wall in the diverging portion of the nozzle. Also visible is an oblique shock which forms downstream of the throat.

The oblique shock is due to a discontinuity in the wall curvature. The wall geometry in this region is represented by a circular arc throat and a conical divergent wall. While the slope of the wall is continuous the wall curvature is discontinuous, leading to a compression of the flow downstream of this point. The beginning of the formation of an oblique shock can also be seen in the nozzles examined in Sections 5.4.1- 5.4.2. However, the divergent portion of the nozzles are too short for the shock to reflect from the centerline.

Figure 5.20c contains the predicted and measured centerline Mach number distributions. The intersection of the shock at the centerline is predicted well and can be better resolved if more grid is used in the axial direction.

Mach contours and centerline Mach number distribution for the present work are in good agreement with the inviscid results shown in Loth et al. [57] and Serra [58]. Loth used a finite element method with an adaptive grid scheme employing 4,990 elements to improve the shock capturing ability, while Serra employed a Lax-Wendroff procedure.

Figure 5.21a illustrates the effect of a 60° constant angle inlet swirl profile on the viscous Mach contours. Identical contour levels (starting at $M = 0.1$ with 0.1 intervals) are shown in Figs. 5.20b and 5.21a. Again, as seen previously, swirl causes an upstream shifting of the Mach contours. It was found that swirl ($S_i = 0.568$) causes C_D to drop 3.2% from 0.967 to 0.936, while the mass flow rate dropped 2.4% from 2.45 to 2.39. Thrust is similarly decreased by 3.3% from 4.80 to 4.64. As in the previously examined geometries η_{SI} is again constant with a value of 0.944.

Comparing the axial distribution of Mach number between the unswirled and swirled cases, Fig. 5.21b, shows a significant difference only in the inlet portion of the nozzle. As discussed previously, the large inlet-to-throat area ratio results in a large swirl number but relatively low absolute value of swirl velocity magnitude. Conservation of angular momentum results in a low swirl velocity in the divergent portion of the nozzle in comparison to the rapidly accelerating axial velocity. Hence, little change is observed in the Mach number distribution downstream of the throat.

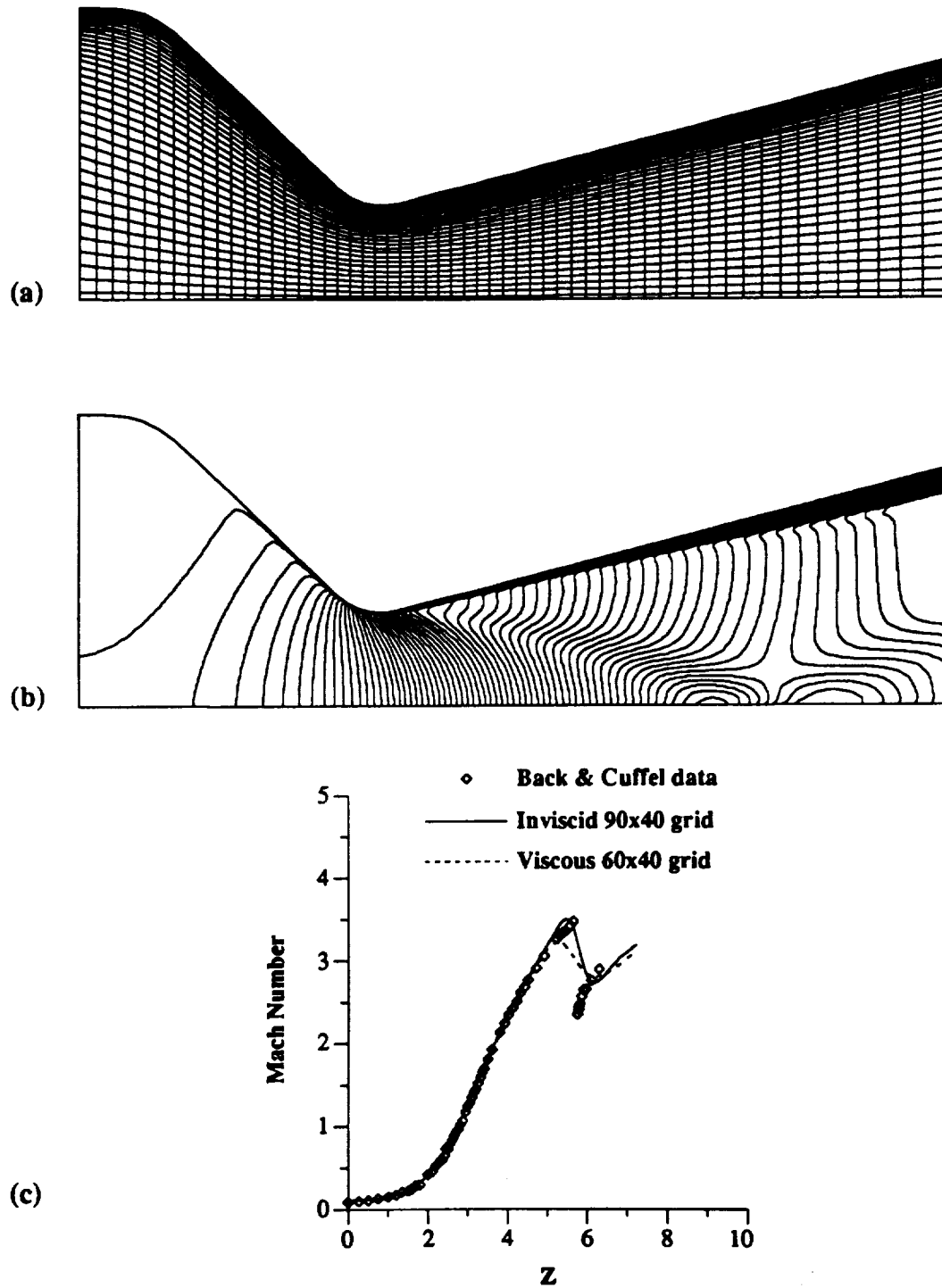


Figure 5.20

Viscous results for Back & Cuffel (B&C) nozzle in unswirled flow, (a) 60 x 40 grid, (b) Mach contours, (c) comparison of experimental and numerical static wall pressure distributions ($Re = 10,0002$)

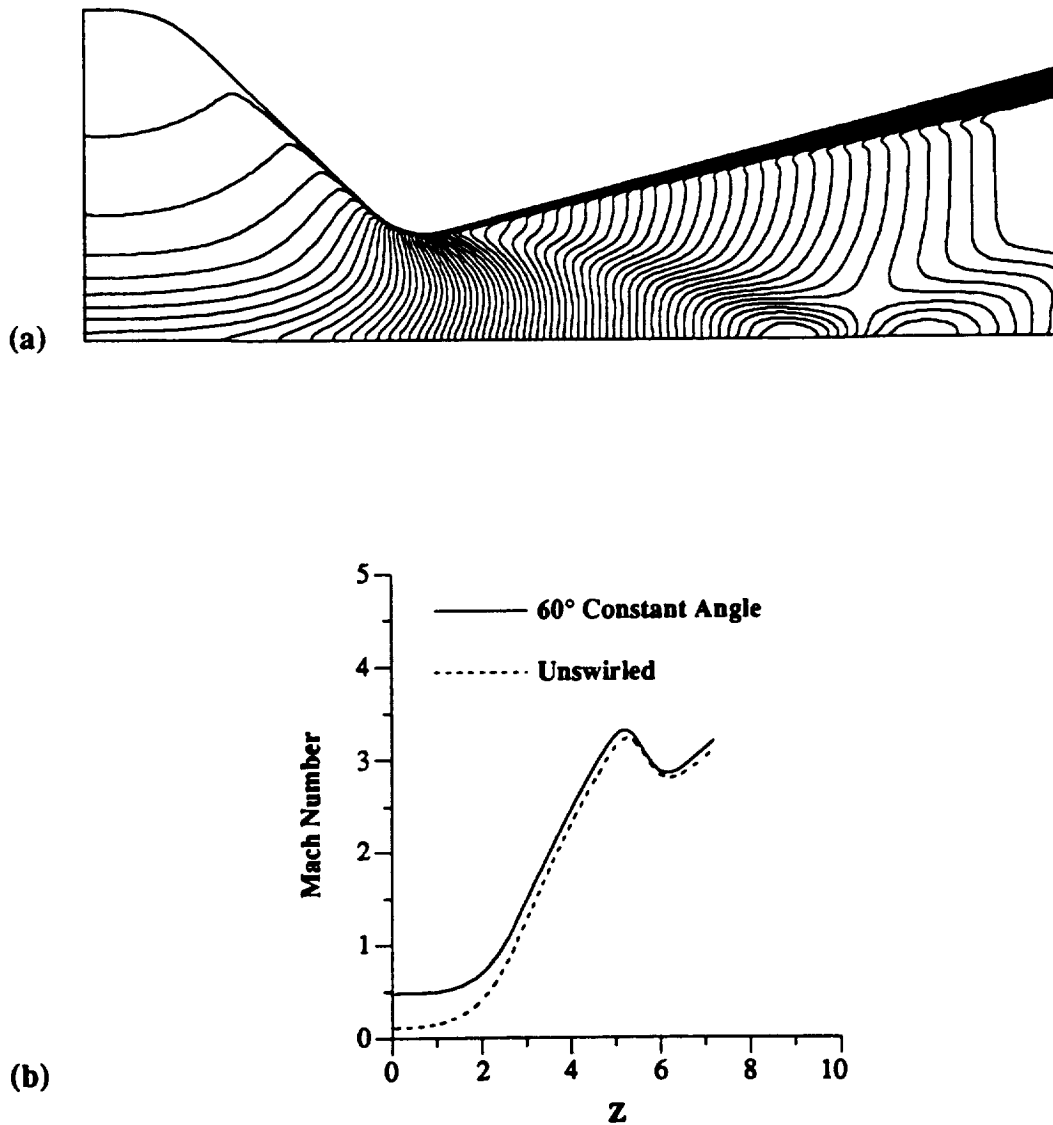


Figure 5.21 Viscous results for Back & Cuffel nozzle, (a) Swirling Mach contours, 60° constant angle, $S_f = 0.568$, (b) swirled and unswirled centerline Mach number distributions ($Re = 10,000$)

The swirl velocity profiles at the inlet, throat, and exit planes for the 60° constant angle inlet swirl profile are shown in Fig. 5.22. The classic constant angle profile shape is clearly visible in the inlet and throat profiles and to a lesser degree in the exit profile. The large inlet-to-throat area ratio combined with conservation of angular momentum causes the magnitude of the throat profile to be the largest.

The residual for the unswirled case dropped six orders of magnitude in 500 iterations while the residual in the swirled case only dropped four orders of magnitude in 750 iterations. Clearly swirl has a significant effect on the convergence rate. This is contrary to the finding for Dutton's initial geometry. The reason for the decrease in convergence rate is two-fold.

First, the inlet-to-throat area ratio for the B&C nozzle is 6.55 while it was only 1.5 for Dutton's initial geometry. A quasi one-dimensional approximation is used as the initial flowfield profile. Clearly, small inlet-to-throat area ratio nozzles have converged solutions which deviate little from this initial guess because the flow is almost one-dimensional. As the inlet-to-throat area ratio increases the final converged solution for the flowfield is highly two-dimensional. Thus, a highly two-dimensional flowfield requires more iterations to reach a converged solution than does a flowfield approaching a one-dimensional approximation.

The second reason the convergence rate is decreased is because the large increase in inlet area occurs in a region of subsonic flow. Information can propagate both upstream and downstream in a subsonic flowfield. Thus, the inlet region of the nozzle requires many iterations to reach a steady-state solution. The supersonic portion of the nozzle can only reach convergence after the subsonic portion converges because the flow of information in a supersonic flowfield is only in the downstream direction.

Checking conservation of mass revealed a maximum error of 1.9% just upstream of the throat for the 60 x 40 grid (for both unswirled and swirled flow cases). A grid refinement study was undertaken to examine the effects of the number of grid points on the converged swirling solution. Running successively coarser grids of 45 x 30 and 30 x 20 increased the maximum mass flow error to 3.1% and 4.6%, respectively. The intersection of the oblique shock on the centerline moved downstream with decreasing grid density. Finally, a 90 x 40 grid was run resulting in a maximum mass flow rate error of less than 1% and a centerline/oblique shock location very slightly upstream of the 60 x 40 location. Thus, the solution approaches an asymptotic limit as the number of grid points increase.

A 60 x 40 grid with the cross-stream mesh lines orthogonal to the nozzle wall (Fig. 5.23) was also run. Integral parameters varied less than 2% from the results obtained with the conventional grid shown in Fig. 5.20a and the Mach contours are essentially unchanged from the results shown in Fig. 5.21b. The strong conservation form of the governing equations adequately represents the flowfield irregardless of the numerical mesh providing a sufficient number of grid points is used.

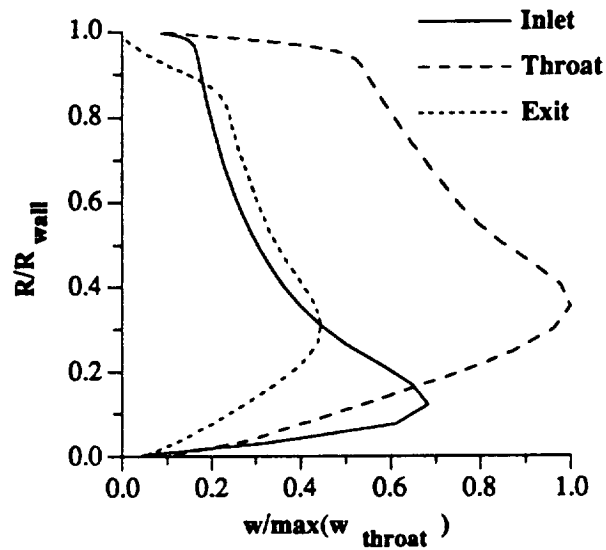


Figure 5.22 Swirl velocity profiles at the inlet, throat, and exit in B&C nozzle for a 60° constant angle inlet profile in viscous flow ($Re = 10,000$)

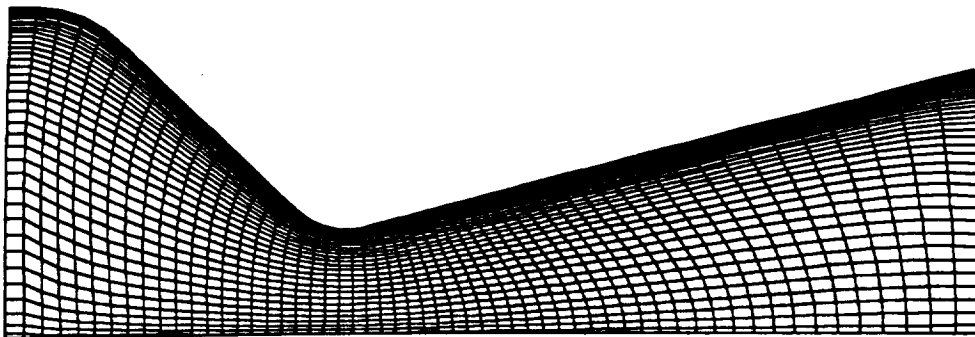


Figure 5.23 Viscous grid in B&C nozzle, 60 x 40, with cross-stream mesh lines orthogonal to nozzle boundaries

5.4.4 Annular Nozzle

An annular nozzle, also examined numerically by Dutton [40, 41] and Chang [39, 42], was examined in order to investigate nozzles with centerbodies. The upper surface is a constant radius wall. The lower surface has a cylindrical inlet with a circular arc transition to a circular arc throat and 10° conical wall. A 50×40 grid (Fig. 5.24a) clustered near the upper and lower surfaces was used to compare to Dutton's inviscid results. The unswirled viscous Mach contours ($Re = 10,000$) are shown in Fig. 5.24b. The inviscid portion of the unswirled flowfield agrees well with Dutton's inviscid result, but significant boundary layers are evident on both surfaces. The present viscous, unswirled results agree almost identically with Chang's work.

A 70° constant angle inlet swirl profile (maximum swirl velocity, w , is $\approx 2.75u$, thus the inlet flow is primarily tangential!) was used to obtain the swirling results shown in Fig. 5.25a. As observed previously swirl causes the Mach contours to shift upstream. The resulting inlet Mach contours are much different than Dutton's inviscid result because of the developing boundary layer on the lower surface. However the viscous, swirling Mach contours are again in almost identical agreement with Chang's results.

Swirl ($S_i = 1.85$) causes C_D and the mass flow rate to drop 9.9% from 0.923 to 0.832, and from 0.973 to 0.875, respectively. Thrust is similarly decreased by 11.0% from 1.63 to 1.45. In addition, η_{SI} is not constant as in the earlier geometries but decreases 1.5% from 0.989 to 0.974 in swirled flow. These decreases in nozzle performance were the largest calculated in this study.

It should also be noted that an extremely large swirl angle was needed as an inlet boundary condition because of the large inlet-to-throat area ratio of 3.06 (the exit-to-throat area ratio is 1.37). The resulting axial velocity component is low at the inlet because of the large area. Inlet swirl angles less than 30° produced values of S_i less than ≈ 1.0 and the resulting flowfield is hardly altered from the unswirled case. Hence, a very large inlet swirl angle is required to produce a noticeable effect on the Mach contours since a large value of w/u is easy to achieve given the small inlet value of u .

The swirl velocity profiles at the inlet, throat, and exit are shown in Fig. 5.25b. These profiles follow a much different trend than observed earlier in the converging-diverging nozzles without centerbodies. In the inviscid core portion of the flowfield, i.e., outside the viscous wall layers, the profiles mirror Dutton's results. A constant angle profile is only apparent in the inlet profile, while the throat and exit profiles are essentially flat outside of the boundary layer. Apparently the reduction in area coupled with a relatively small radius change across the throat and exit planes of the nozzle causes the angular momentum to be essentially constant across the cross-section of the nozzle. Angular momentum appears to be preserved since the relative magnitudes of the swirl velocity are inversely proportional to the centerbody radius at the inlet (smallest), throat (largest), and

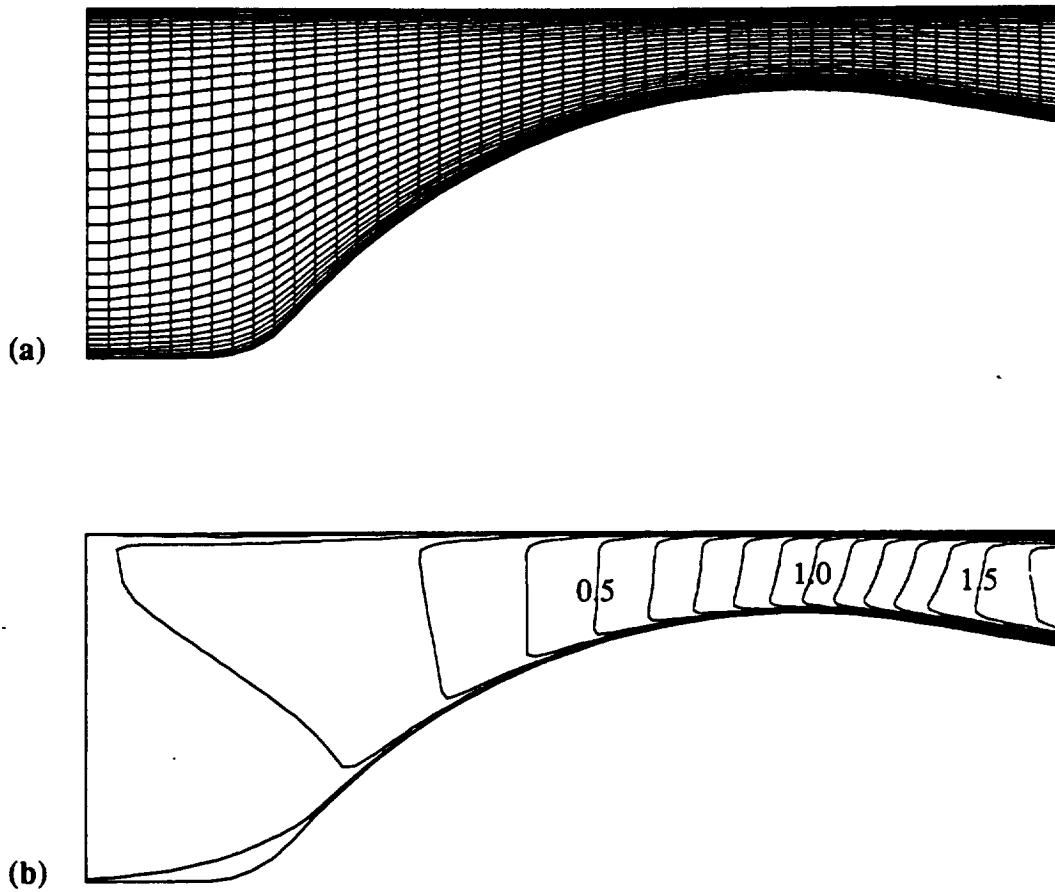


Figure 5.24 Viscous results for an annular nozzle (a) 50 x 40 grid, (b) unswirled Mach contours ($Re= 10,000$)

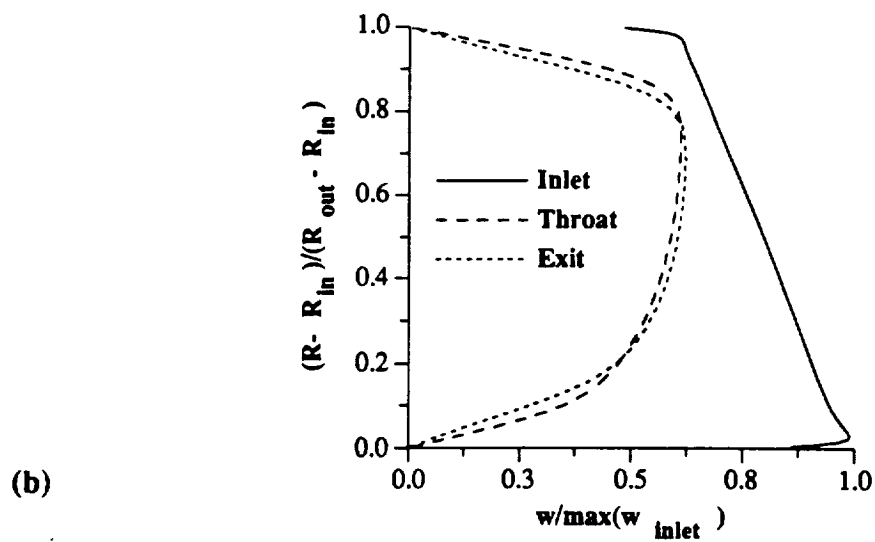
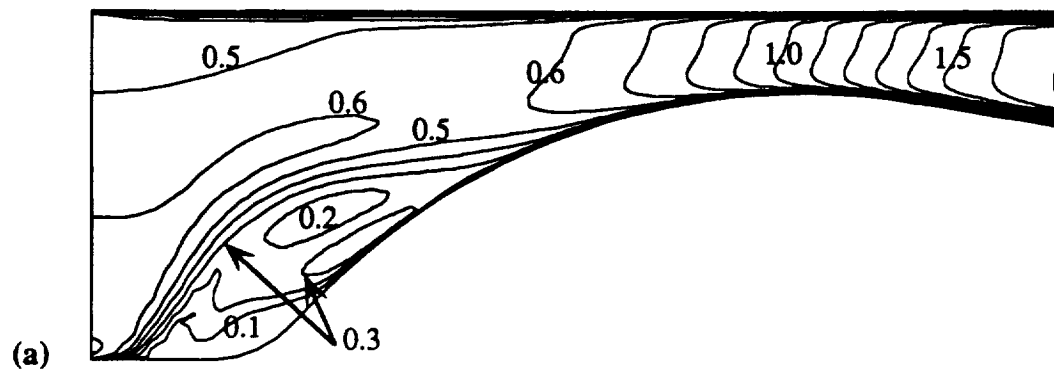


Figure 5.25

Viscous results for an annular nozzle, (a) swirling Mach contours, 70° constant angle ($Si = 1.85$), (b) swirl velocity profiles at the inlet, throat, and exit ($Re = 10,000$)

exit (intermediate). These results could not be contrasted to Chang as he did not present any results for the swirl velocity components.

An exact value of the swirl or axial velocity cannot be specified at the inlet, only the ratio of swirl/axial. As stated earlier, in viscous, swirling flow cases the inlet swirl angle is modified to asymptotically approach zero at the wall. This modification to the constant angle inlet swirl profile was enforced at the upper surface of the annular nozzle (Fig. 5.25). It was realized that this modification should also be enforced at the surface of a centerbody also. It is clear from Fig. 5.25b that the axial velocity does not approach zero as the centerbody surface is approached since the normalized swirl velocity component is ≈ 0.9 .

Figure 5.26 ($S_i = 0.987$) illustrates the drastic modification to the flowfield when the inlet swirl angle is modified to asymptotically approach zero at both the upper and lower solid surfaces. The Mach contours are not shifted as far upstream as in Fig. 5.25a and the growth of the boundary layer occurs quickly but with a smoother transition above the centerbody. The swirl velocity profiles (Fig. 5.26b) show the same general trends in the inviscid region as for the prior case (Fig. 5.25b) but the boundary layer development is now much clearer on both surfaces as the swirl velocity approaches zero at a solid surface. Apparently Chang only used an asymptotic swirl velocity profile at the upper solid surface since Fig. 5.25a almost identically matches his viscous swirling flow results.

Values of C_D , mass flow rate, thrust, and η_{SI} are 0.882, 0.928, 1.54, and 0.974, respectively, for the asymptotic inlet swirl case at both upper and lower solid surface. Table 5.3 contains a summary for the annular nozzle cases discussed in this section.

Examination of mass conservation revealed there was a maximum error of 0.3% based on the inlet mass flow rate in the three cases discussed above. The residual dropped four orders of magnitude in 500 iterations for the unswirled case and only two orders of magnitude in 500 iterations and three orders of magnitude in 750 iterations for the swirled cases. However, there was less than 1% change in the swirl case integral parameters between 500 and 750 iterations and the Mach contours showed only slight changes. For qualitative purposes the solution had converged in 500 iterations, but, if detailed flowfield information was desired, the swirled cases would need to run longer until the residual had dropped at least four orders of magnitude.

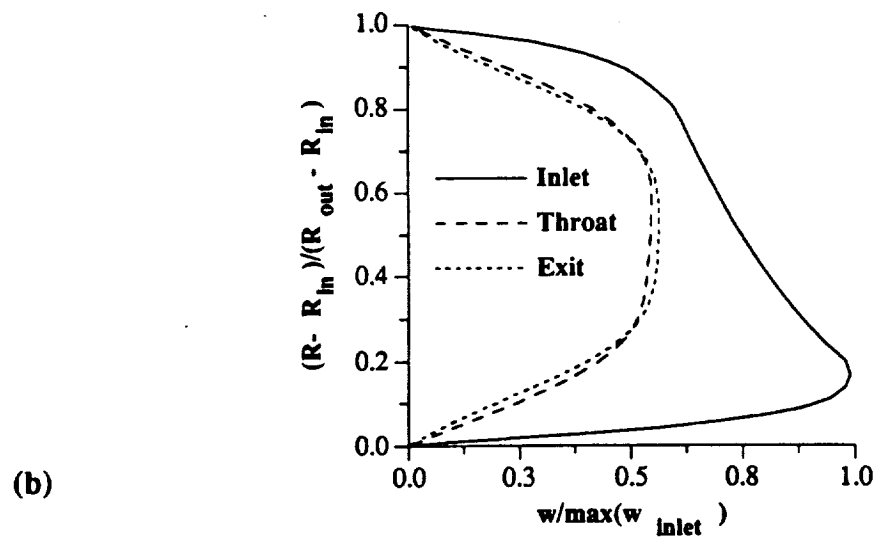
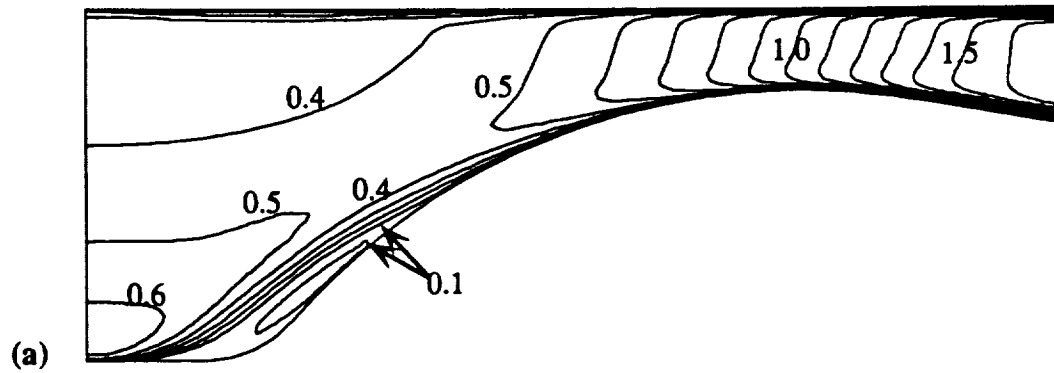


Figure 5.26

Viscous results for an annular nozzle with a modified asymptotic inlet swirl profile, (a) swirling Mach contours, 70° constant angle ($Si = 0.987$), (b) swirl velocity profiles at the inlet, throat, and exit ($Re = 10,000$)

Table 5.3 **Nozzle performance summary for the annular nozzle**

Figure	Re	Grid	Swirl	C_D	η_{vs}	η_{SI}	S_i	Thrust	Mass Flow Rate
5.24	10,000	50 x 40	—	0.923	0.912	0.989	0.0	1.63	0.973
5.25	10,000	50 x 40	70° Cst Angle	0.832	0.810	0.974	1.85	1.45	0.875
5.26	10,000	50 x 40	70° Cst Angle	0.882	0.864	0.980	0.987	1.54	0.928

5.4.5 100:1 Area Ratio Nozzle

The largest area ratio nozzle examined to present using the methodologies developed in this work is a 100:1 exit-to-throat nozzle used in experimental resistojet studies at NASA Lewis Research Center [59]. The experimental inlet stagnation pressure and temperature were 6,400 Pa and 699 K, respectively, with a throat Reynolds number of 850. A 60 x 45 grid with clustering near the wall was used to obtain the numerical results for the 45°-20° nozzle shown in Fig. 5.27a. Also included in the figure, at the same scale, is the numerical grid from the experimental converging-diverging nozzle (50 x 40 grid) examined earlier.

Figure 5.27b,c contain the viscous Mach contours for unswirled and swirling viscous ($Re = 850$) flows, respectively. In both cases the boundary layer occupies a large portion of the diverging section of the nozzle. It should be noted that the exit plane centerline Mach number is approximately 5.0 in each flow. Figure 5.28 contains the Mach contours for an unswirled viscous flow at $Re = 5,000$. Except for a thinner boundary layer and a slight shift downstream of the oblique shock/centerline intersection point the flowfield looks much the same as the unswirled, $Re = 850$ case.

Figure 5.29 compares measured and predicted exit plane pitot pressures. The predicted result at $Re = 850$ is in good agreement with measurements near the centerline but differs with the experimental data as the radius increases. The pitot pressure profile for the swirling flow case at a $Re = 850$ was essentially the same as the unswirled result. Several reasons for the disparity between the predicted and experimental results may be offered.

One possible reason is inadequate grid density. As may be concluded from examination of Fig. 5.27a, a 60 x 45 grid is probably the minimum size needed to obtain adequate resolution of the flowfield for this large area ratio nozzle. But as seen in the oblique shock nozzle case discussed earlier, inadequate grid density leads to mass conservation errors. The residual for the unswirled case dropped 4 orders of magnitude in 1,300 iterations, indicating the flowfield would change little from the current values, but had a maximum mass flow rate error (based on the inlet mass flow rate value) of 16% in the subsonic region and a constant 10% error downstream of the throat. Thus a converged solution with poor mass conservation points to inadequate grid density (see the B&C nozzle discussion).

The probability that inadequate grid density in the subsonic portion of the nozzle leads to mass conservation errors is large when one compares the inlet-to-throat ratios of the two nozzles in Fig. 5.27a. The inlet area ratios of the Back & Cuffel/oblique shock nozzle and the 100:1 area ratio nozzles are 9.75 and 48.4, respectively. The nozzles have roughly the same number of grid points in the radial direction (40 and 45 respectively). The B&C nozzle required 60 grid points in the axial direction to reduce the mass conservation error to less than 1%. Approximately 20 grid points were in the subsonic portion of the

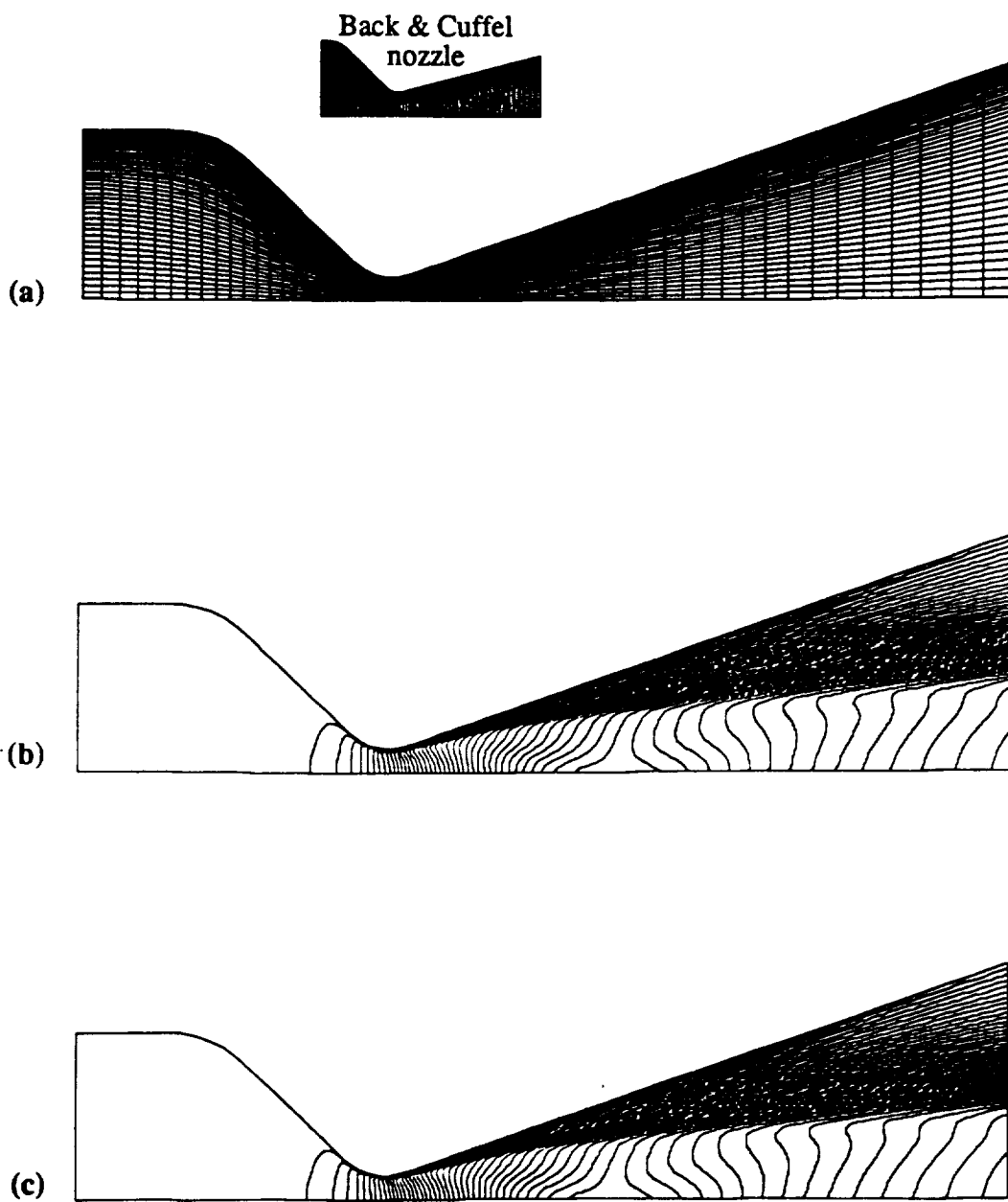


Figure 5.27 Viscous results for a 100:1 area ratio nozzle (a) 60 x 45 grid, (b) unswirled Mach contours, (c) swirling Mach contours, 30° constant angle ($Re = 850$)

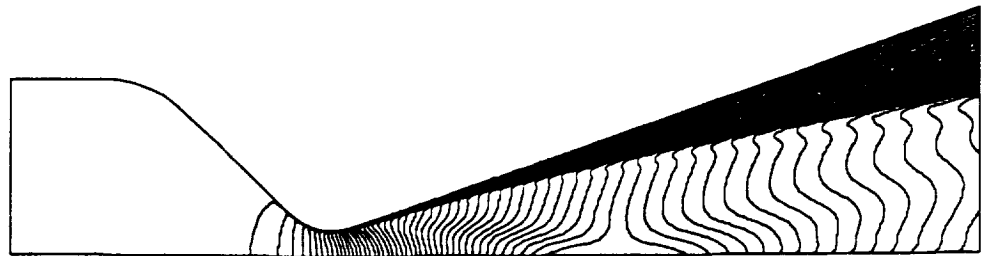


Figure 5.28 Unswirled Mach contours for a 100:1 area ratio nozzle ($Re = 5,000$)

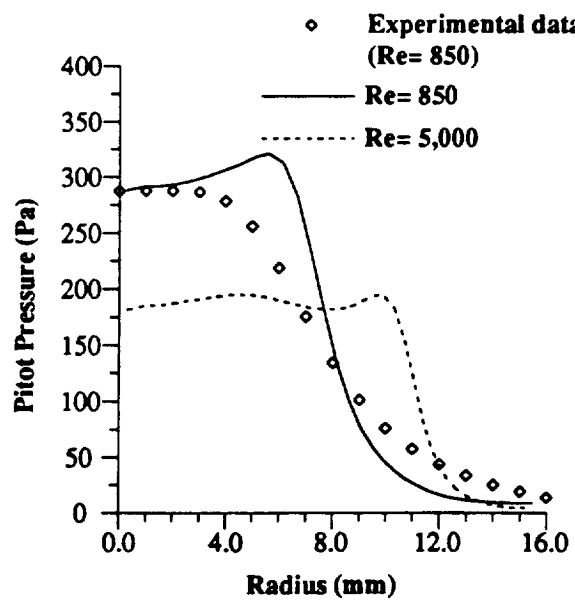


Figure 5.29 Comparison of measured and predicted exit plane pitot pressure distribution in 100:1 area ratio nozzle

nozzle. The 100:1 area ratio nozzle employs approximately 25 grid points in the axial subsonic portion of the nozzle. Thus roughly the same number of grid points were used to represent areas a factor of five different.

Another source for error is an insufficient number of iterations. The residual for the swirled flowfield had only dropped one order of magnitude in 1,300 iterations. Checking the subsonic flowfield revealed the inlet plane had converged at 1,300 iterations but the remainder of the subsonic portion of the nozzle was still evolving. The mass flow rate was again constant in the diverging portion of the nozzle, indicating the supersonic portion of the flowfield was converged and changing as the upstream conditions evolved. Examination of the swirl profiles showed the swirl velocity at the throat and exit planes was still developing.

Thus a combination of inadequate grid density and an insufficient number of iterations undoubtedly contributed to the poor exit plane pitot pressure prediction.

Another possibility of error related to inadequate grid density lies with the oblique shock representation. The hump in the numerical pitot pressure prediction coincides with the position of the oblique shock reflecting downstream from the centerline to the exit plane. The reflected oblique shock could be inadequately represented because of the relatively sparse grid in the diverging portion of the nozzle.

A final source for the error in the pressure discrepancy lies with the nozzle geometry. The throat radius of this nozzle was 0.0625" (0.0159 mm). However because of the machining process used and the extremely small dimensions of the nozzle the actual throat geometry, i.e. throat radius, radius of curvature of the nozzle walls, was not available at the time this study was performed.

When an adequate model of the nozzle throat geometry is determined grid refinement studies will be conducted to obtain converged solutions with mass conservation errors of less than 1%. Then a comparison between predicted and experimental results can be made and the effects of swirl on the flowfield can be determined.

5.4.6 Arcjet thruster nozzle

An arcjet thruster geometry combines all of the difficult geometrical features examined in the previous sections into one geometry. A typical arcjet geometry contains a centerbody, representing the cathode, that partially extends into a large area ratio converging-diverging nozzle. A geometry representative of arcjets [25] was formed by placing a centerbody with a 45° tip angle in the subsonic portion of a 35° - 18.5° converging-diverging nozzle. The C-D nozzle wall contour is the same geometry used in Dutton's experimental nozzle examined earlier. The inlet and exit to-throat area ratios are 3.6 and 4.0, respectively.

A 60×45 grid shown in Fig. 5.30a was clustered at both surfaces and was used to resolve the boundary layers on the centerbody and nozzle wall. Figure 5.30b shows the resulting Mach contours for viscous flow at a $Re = 850$. As could be expected from the previous results a thick boundary layer forms on the nozzle wall because of the very low Reynolds number. Viscosity obviously plays an extremely important role in flow. The flow rapidly accelerates downstream of the cathode tip along the nozzle centerline. However, the sonic line extends far downstream of the nozzle wall sonic line location. Comparing the location of the centerline sonic point with the result for Dutton's experimental nozzle shows the centerbody has pushed the sonic line further downstream. Although this is not a surprising result, it demonstrates the highly two-dimensional nature of the flow.

A 30° constant angle inlet swirl profile modified to asymptotically approach zero at both surfaces (see Section 5.3. Annular nozzle for a discussion of the modification) was used to introduce swirl into the flowfield. The resulting viscous Mach contours are shown in Fig. 5.31a for a Reynolds number of 850. As observed previously the Mach contours are shifted upstream slightly as a consequence of the swirling velocity component. The resulting swirl number, $S_i = 0.320$, indicates a low level of swirl. Using a maximum swirl angle greater than 30° would have had a greater effect on the flowfield.

Examining the integral parameters illustrates the small changes caused by swirl. The C_D decreased 1.2% from 0.896 to 0.885 while the mass flow rate decreased 1.3% from 2.27 to 2.24. Thrust decreased 1.2% from 4.06 to 4.01 and η_{SI} was constant at 0.946.

The swirl velocity profiles at the inlet, throat, and exit are shown in Fig. 5.31b. The constant angle profile is visible in the inlet profile becomes distorted as the flow travels downstream from the inlet and is first compressed as it nears the cathode tip, expands over the cathode tip, and continues to expand in the diverging portion of the nozzle. Qualitatively, conservation of angular momentum is satisfied by noting the magnitude of the largest swirl velocity component occurs at the throat because the throat corresponds to the smallest area with the smallest mean radius. The exit-to-throat area ratio of 4.0 is approximately the same as the inlet-to-throat area ratio of 3.6. However, the mean radius of the inlet is larger than the mean radius of the exit plane. Thus the swirl magnitude is

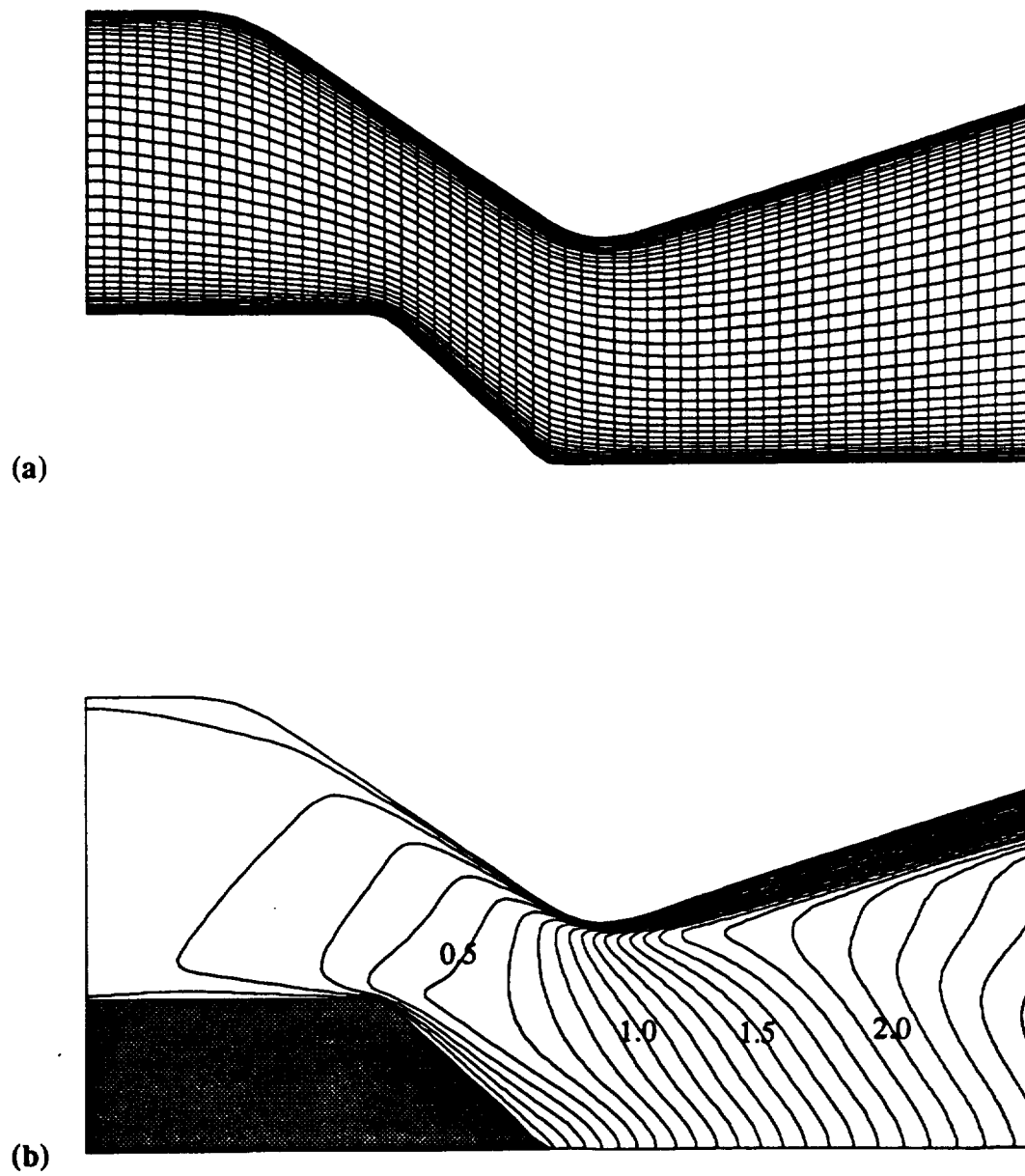


Figure 5.30 Viscous results for an arcjet thruster nozzle (a) 60 x 45 grid, (b) unswirled Mach contours ($Re= 850$)

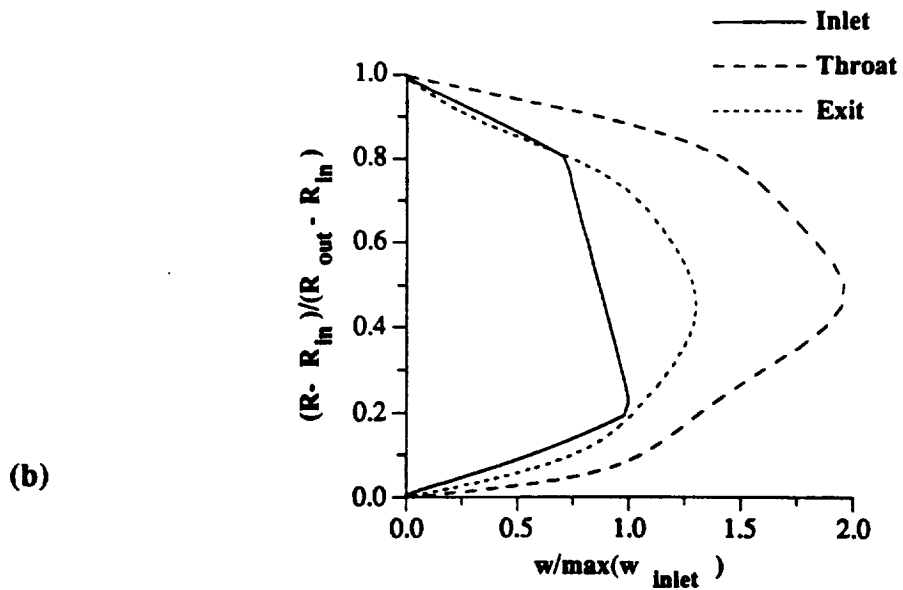
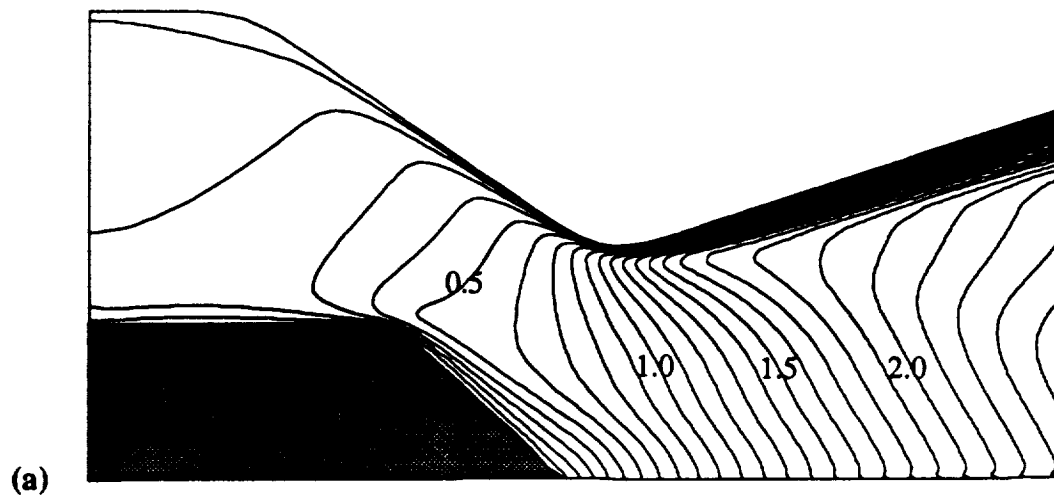


Figure 5.31

Viscous results for an arcjet thruster nozzle, (a) swirling Mach contours, 30° constant angle ($Si = 0.320$), (b) swirl velocity profiles at the inlet, throat, and exit ($Re = 850$)

observed to be smaller at the inlet than at the exit plane.

The maximum mass conservation error, based on the inlet value of mass flow rate, was less than 0.6% in both the unswirled and swirled cases. The residual for the unswirled case dropped five orders of magnitude in 1300 iterations, while the residual for the unswirled case only dropped three orders of magnitude in 1300 iterations. Thus, as observed earlier, swirl does affect the convergence rate in highly two-dimensional flowfields.

Comparing the B&C and arcjet nozzles shows vastly different convergence rates for grids containing approximately the same number of grid points ($\approx 60 \times 40$). In unswirled flow computations, the residual in the B&C nozzle case dropped six orders of magnitude while the residual in the arcjet case only dropped three orders of magnitude. The reason for the discrepancy is because the arcjet grid was clustered at both upper and lower surfaces while the grid used in the B&C nozzle was only clustered along the upper surface. Grid clustering causes a large decrease in the convergence rate.

5.4 Computational requirements

The data processing rate (DPR) for the viscous flow results using the implicit algorithm was 1.06×10^{-3} seconds/(grid point*iteration) on a Cray XMP 2/8 using default vectorization. A fully vectorized three-dimensional version employing MacCormack's algorithm reported [33] a DPR of 3.1×10^{-4} on a Cray-2 single processor. Since the Cray 2 is on the order of two times faster than a Cray XMP and little work has been done to vectorize the present code; it was felt that the DPR for this algorithm is acceptable. Recent use of Cray Research Inc. vectorization software indicates the DPR can be reduced by a factor of two with some minor modifications to the block-tridiagonal solver subroutines used in the code.

As discussed in Section 3.3.1 for a grid described as 60×45 , the computational domain actually contains 58×43 grid points for a total of 2,494 grid points. Thus, a solution for the arcjet nozzle requiring 1300 iterations would take $\approx 3,400$ seconds of CPU time.

The time step definition used by MacCormack [20] was modified for the non-dimensional form of the governing equations used in this study. The resulting definition for the time step based on a given CFL (Courant-Friedrichs-Lewy) number is

$$\frac{CFL}{\Delta t} = \left\{ (|u| d_a + |v| d_b) J + \sqrt{\frac{\gamma T}{\gamma_0} (d_a^2 + d_b^2) J^2} + \frac{2 \mu}{\rho Re} (d_a^2 + 2 d_a d_b + d_b^2) J^2 \right\}$$

The majority of computations in this study were run with an initial CFL value of 0.25 incrementing to 25.0 by 0.25 increments/iteration. When the residual had dropped to one-tenth of the initial value, the CFL was incremented again by 0.5 increments/iteration until a maximum CFL value of 80.0 was reached and remained constant for the remainder of the computation. The swirled arcjet thruster geometry case was run with a maximum CFL of 50.0. Higher maximum CFL numbers resulted in growing instabilities occurring at the nozzle centerline upstream of the exit plane. The instabilities were not seen in any of the other cases examined.

Summary & Recommendations

6.1 Summary

In this dissertation a method has been presented for modeling swirling flow through a constricted arcjet thruster geometry. The method allows the effects of swirl and viscosity to be determined in an axisymmetric nozzle (with or without a centerbody). The numerical method is stable for large time steps allowing steady-state solutions to be achieved in a small number of iterations.

An order of magnitude analysis was used to examine all of the terms contained in the equations governing the fluid mechanics and electromagnetic fields in an arcjet thruster. Retaining the significant terms revealed that the remaining fluid mechanics and combined electromagnetic field equations are uncoupled. The only link between the two equation sets is through the electrical conductivity of the gaseous propellant, which is a function of the pressure and temperature.

Experimental results have shown a swirling velocity component stabilizes the constricted arc. Thus, a circumferential or swirl velocity component as well as the axial and radial velocity components were needed in the analysis. Since a typical nozzle geometry is symmetric about the centerline, a two-dimensional axisymmetric formulation was utilized.

An algorithm was developed to solve the governing fluid mechanics equations, the axisymmetric Thin-Layer Navier Stokes equations. Based on MacCormack's [20] algorithm, the technique is fully implicit, second-order accurate in space and flux-split. By employing an implicit algorithm large time-steps could be used to reach the desired steady-state solution. Second-order spatial accuracy is required to obtain solutions valid throughout flowfields with complex geometries. Flux-splitting the inviscid fluxes accurately represents the physics of the flow by allowing information to travel in the appropriate direction. Thus, subsonic and supersonic regions are represented without the use of artificial damping. Since the method does not employ approximate factorization no additional terms are introduced into the finite-volume representation of the governing equations.

An implicit boundary condition technique was successfully adapted for use at the inlet and exit nozzle planes. The method can be used to specify the appropriate number of conditions for subsonic or supersonic flows. The effects of three different inlet swirl velocity profiles were investigated by specifying different inlet plane ratios of swirl velocity

to axial velocity. Each inlet swirl profile produced a different effect on the flowfield and degraded the nozzle performance by varying degrees.

A numerical grid generator was written to provide the mesh to represent the nozzles examined. The grid generator can produce mesh with the cross-stream grid lines non-orthogonal to the upper and lower surfaces, i.e., vertical, or with cross-stream grid lines orthogonal to the upper and lower surfaces. Since the governing equations were formulated in a strong conservation form, grid orthogonality should not affect the conservation of mass, momentum, and energy of the algorithm, but this could not be determined *a priori*. Grid orthogonality was found to have little effect on the converged steady-state solution.

Since typical arcjets employ large area ratio converging-diverging nozzles containing centerbodies, a wide variety of nozzle geometries were needed to validate the algorithm. These included conventional converging-diverging nozzles with exit-to-throat area ratios as large as 100 (with inlet-to-throat area ratios as large as 48) and an annular nozzle with a full-length centerbody. Computed Mach number distributions, static wall pressures, and oblique shock structures were in excellent agreement with experimental data and previous numerical results. The degradation of nozzle performance due to swirl and viscosity was also clearly illustrated. Finally, a typical arcjet thruster geometry was examined. The effects of swirl on nozzle performance and of geometry on the swirl profiles throughout the nozzle were demonstrated.

6.2 Conclusions

The numerical algorithm provides an accurate method of calculating the viscous, swirling flowfields through converging-diverging nozzles. In both unswirled and swirling flows, comparisons with experimental data and other numerical calculations were in excellent agreement for quantities such as Mach contours, static pressure distributions and oblique shock structures including reflected oblique shocks.

Viscosity was shown to play an important role in the wall pressure recovery downstream of the nozzle throat. Viscous effects were also shown to be important in large area ratio nozzles where the Re is on the order of 1,000. The boundary layer occupies a significant portion of the diverging portion of the nozzle in low Reynolds number/high area ratio nozzles. Viscous effects were also evident in nozzles containing centerbodies. The mass flow rate was also shown to decrease when viscous effects were included and compared with inviscid results.

Swirl was shown to cause a decrease in the mass flow rate, and a resultant decrease in the thrust, through a rise in the centerline axial velocity distribution and a concomitant decrease in the density. This effect is observable through the marked upstream shifting of the Mach contours in highly swirled flows. The decreased mass flow rate can be offset by an increase in the throat radius or inlet stagnation pressure. Since the assumed inlet swirl

profile and maximum swirl angle greatly affects the resulting flowfield both need to be measured experimentally in order to obtain an accurate representation of the flowfield.

The swirl velocity magnitude at a cross-section of a nozzle varies inversely to the area and mean radius of the cross-section (in comparison to the inlet area and inlet mean radius). As the flow accelerates through a nozzle throat into the diverging exit the ratio of swirl/axial velocity decrease due to the increase in area and axial velocity magnitude. Thus, the effects of swirl are most strongly felt in the subsonic portion of the nozzle. For instance very high inlet swirl levels would be needed to shift a centerline/oblique shock intersection point upstream in the diverging portion of a nozzle.

Cross-sectional area magnitudes also strongly influence the convergence rate, especially in the subsonic regions of swirling flows. As the inlet-to-throat ratio increases the subsonic flowfield requires a longer time to converge to a highly two-dimensional flowfield from the one-dimensional approximation used as the initial guess. Since the initial guess assumes the swirling velocity component is zero the algorithm must determine the value throughout the flowfield. In highly swirled flow with a large inlet-to throat area ratio the change in the swirling velocity magnitude through the flowfield will be large. Because information propagates in all directions in the subsonic regime, convergence is rapidly slowed as the area ratio and level of swirl increases.

Mass conservation is also affected by large inlet-to-throat area ratio nozzles. As the area ratio increases, a larger number of grid points is required to maintain mass flow rate errors less than 1%. With but one exception, the nozzles examined in this research had mass conservation errors, based on the inlet mass flow rate, of less than 0.6%. The exception was the 100:1 exit-to-throat area ratio nozzle which had an unconverged mass flow rate error of 16% in the subsonic inlet (inlet-to-throat area ratio of 48.4). More grid points and more iterations are required to achieve mass flow rate errors of less than 1% in the subsonic portions of large inlet-to-throat area ratio nozzles.

A double penalty in convergence rate is paid to resolve the flowfield gradients in a large inlet-to-throat area ratio nozzles with swirl. More grid points are needed to resolve the large gradients but as the number of grid points increases the convergence rate decreases for any nozzle configuration. And as the inlet-to-throat area ratio increases the more the final converged swirling flowfield will differ from the initial assumed state of zero swirl, thus slowing the convergence rate.

Convergence is not only affected by the number of grid points but by the location of the grid points. Clustering the grid points near a wall causes large decrease in the convergence rate for instance. Thus as the grid density increases the convergence rate decreases. Brief studies of grid orthogonality at the upper and lower boundaries indicated little change in the final solution but did decrease the increase the convergence rate slightly.

The DPR of 1.06×10^{-3} seconds/(grid point*iteration) is adequate but leaves room for improvement. As more realistic arcjet geometries are examined a faster processing rate becomes more important since the inlet- and exit-to-throat area ratios of arcjets are large. As

discussed above the convergence rate decreases as the area ratio increases.

6.3 Recommendations for Future Research

The formulation presented in this dissertation showed the fluid mechanics and electromagnetic (Emag) field equations were decoupled, allowing the research to be conducted in two phases. The first phase has been completed by developing an algorithm to solve the governing fluid mechanics equations. The second phase would be to include the Emag field effects in an operational arcjet. This can be accomplished by developing an algorithm for the Emag field governing equation presented in Chapter 2. A solution for a running arcjet would be obtained by solving the fluid mechanics and Emag algorithms iteratively until a converged solution is reached.

An alternative method for the second phase would be to reformulate the fluid mechanics algorithm to include the Emag field equation and solve the combined set of six governing equations simultaneously.

At the present time a far reaching extension of the modeling efforts would be to not make an assumption of LTE. The resulting two temperature plasma model would include electron temperatures as well as ion and neutral particle temperatures. Thus, the model would be valid in regions near the cathode and anode surfaces where the single fluid plasma model of this research is not valid.

Computational studies need to be conducted to resolve the mass conservation errors in the large inlet- and exit-to-throat area ratio nozzles. Obvious avenues of investigation including adding more grid points and/or running for more iterations. Partitioning the flowfield into sub and supersonic portions would be another approach. First, a converged solution should be obtained in the subsonic portion of the nozzle. The supersonic portion of the nozzle could then be solved using the subsonic portion as an inlet boundary condition. In this way computational time is not wasted on the supersonic portion of the nozzle when the subsonic portion, i.e., inlet condition, of the flowfield is still evolving.

Another point needing resolution is the discrepancy in the exit plane pitot pressure distribution for the 100:1 area ratio nozzle. A more accurate nozzle geometry needs to be determined and combined with the computational studies above to provide a converged solution with mass conservation errors of less than 1%.

Parametric studies could be conducted to determine the effects of nozzle shape on thruster performance. Alternatively, the fluid mechanics algorithm could become a portion of an algorithm to compute the optimum nozzle shape based on design parameters such as thrust, mass flow rate, and geometry.

Other extensions to the algorithm would be to include an adaptive grid scheme to provide automatic resolution of high gradient regions or to include all of the viscous terms in the explicit portion of the algorithm, resulting in the full Navier-Stokes equations.

Any large programming project will take twice as long as you estimate, even if you include that eventuality in your estimate.

***Babbage's Law
in honor of Charles Babbage (1792-1871),
pioneer computer scientist***

References

- [1] Shaeffer, J. F., "Swirl Arc: A Model for Swirling, Turbulent, Radiative Arc Heater Flowfields," *AIAA Journal*, Vol. 16, No. 10, October 1968, p. 1068.
- [2] Wallner, L. E. and Czika, J., "Arc-jet Thrustor for Space Propulsion," NASA TN-D2868, NASA Lewis Research Center, Cleveland, Ohio, 1965.
- [3] Brewer, G. R. *Ion Propulsion; Technology and Applications*, Gordon and Breach, New York, 1970.
- [4] Camac, M., "Plasma Propulsion Devices," *Advances in Space Science*, Ed. Fredrick I. Ordway, III, Vol. 2, New York, Academic Press, 1960.
- [5] Jahn, R. G. *Physics of Electric Propulsion*, Chapter 6, Reference No. 18 McGraw Hill, New York, 1968.
- [6] Curran, F., "An Experimental Study of Energy Loss Mechanisms and Efficiency Considerations in the Low Power dc Arcjet," NASA TM-87123, NASA Lewis Research Center, Cleveland, Ohio, 1985. (AIAA Paper 85-2017) .
- [7] Stone, J.R. and Huston, E.S., "The NASA/USAF Arcjet Research and Technology Program," NASA TM- 100112, NASA Lewis Research Center, Cleveland, Ohio, 1987. (AIAA Paper 87-1946) .
- [8] Stine, H.A. and Watson, V.R., "The Theoretical Enthalpy Distribution of Air in Steady Flow Along the Axis of a Direct-Current Electric Arc," NASA TN D-1331, NASA Ames Research Center, Moffett Field, California, August 1962.
- [9] Watson V.R. and Pegot E.B., "Numerical Calculations for the Characteristics of a Gas Flowing Axially Through a Constricted Arc," NASA TN D-4042, NASA Ames Research Center, Moffett Field, California, June 1967.
- [10] Neuberger, A. W., "Thermo-Gasdynamical and Electrical Behavior of the Wall-and Vortex Stabilized Arc," Translation of DLR-FB-75-38, European Space Agency, ESA-TT-220, December 1975.
- [11] Neuberger, A. W., "Heat Transfer in Swirling Compressible Flows," AIAA Paper 75-706, 1975.
- [12] Gupta, A. K., and Lilley, D. G., *Flowfield Modeling and Diagnostics*, Tunbridge Wells, England, Abacus Press, 1983.
- [13] Nishida, M., Kaita, K., and Tanaka, K., "Numerical Studies of the Flow Field in a DC Arcjet Thruster," DGLR/AIAA/JSASS 20th International Electric Propulsion Conference, October 3-6, 1988, Garmisch-Partenkirchen, W. Germany (Paper#88-105) .
- [14] Auweter-Kurtz, M., Kurtz, H. L., Schrade, O. H., and Slezione, P. C., "Numerical Modeling of the Flow Discharge in MPD Thrusters," *Journal of Propulsion and Power*, Vol. 5, No. 1, Jan.-Feb. 1989, pp. 49-55. Presented

- as Paper 87-1091 at the DGLR/AIAA/JSASS 19th International Electric Propulsion Conference, Colorado Springs, CO, May 11-13, 1987.
- [15] Auweter-Kurtz, M., Glaser, S. F., Kurtz, H. L., Schrade, O. H., and Sleziona, P. C., "An Improved Code for Nozzle Type Steady State MPD Thrusters," DGLR/AIAA/JSASS 20th International Electric Propulsion Conf., October 3-6, 1988, Garmisch-Partenkirchen, W. Germany (Paper No. 88-040) .
 - [16] Liu, C. F., "Numerical Analysis of the Anode Region of High Intensity Arcs," Ph.D. Dissertation, University of Minnesota, 1977.
 - [17] Chen, D. M., "Analytical Modeling of Two-Temperature Argon Arc Plasmas," Ph.D. Dissertation, University of Minnesota, 1980.
 - [18] Chen, D. M. and Pfender, E., "Modeling of the Anode Contraction Region of High Intensity Arcs," *IEEE Trans. Plasma Sci*, Vol. PS-8, Sep. 1980, pp. 252-259.
 - [19] Wilhelmi, H., Wimmer, W., and Pfender, E., "Modeling of the Transport Phenomena in the Anode Region of High Current Arcs," *Numerical Heat Transfer*, Vol. 8, 1985, pp. 731-749.
 - [20] MacCormack, R. W., "Current Status of Numerical Solutions of the Navier-Stokes Equations," AIAA Paper No. 85-0032, 1985.
 - [21] Bird, R. B., Stewart, W. E., and Lightfoot, E. N., *Transport Phenomena*, John Wiley and Sons, Inc., 1960.
 - [22] Sutton, G. W., and Sherman, A. S., *Engineering Magnetohydrodynamics*, McGraw-Hill Book Co., 1965.
 - [23] Bittencourt, J. A., *Fundamentals of Plasma Physics*, Pergamon Press, 1986.
 - [24] Carney, L., "An Experimental Investigation of an Arcjet Thruster Exhaust using Langmuir Probes," M.S. Thesis, University of Toledo, Toledo, Ohio, 1987.
 - [25] Curran, F. and Nakanishi, S., "Low Power dc Arcjet Operation with Hydrogen/Nitrogen Propellant Mixtures," NASA TM-87279, NASA Lewis Research Center, Cleveland, Ohio, 1987. (AIAA Paper 86-1505) .
 - [26] Sarmiento, C., personal communication, NASA Lewis Research Center, Cleveland, Ohio, August 31, 1988.
 - [27] Anderson, D. A., Tannehill, J. C., and Pletcher, R. H., *Computational Fluid Mechanics and Heat Transfer*, Hemisphere Publishing Corp., 1984.
 - [28] Steger, J. L., and Warming, R. F., "Flux Vector Splitting of the Inviscid Gasdynamic Equations with Application to Finite-Difference Methods," *J. of Computational Physics*, Vol. 40, 1981, pp. 263-293.
 - [29] Candler, G. V., "The Computation of Weakly Ionized Hypersonic Flows in Thermo-chemical Nonequilibrium," Ph.D. Dissertation, Stanford University, June 1988.
 - [30] MacCormack, R. W., and Candler, G. V., "The Solution of the Navier-Stokes

- Equations using Gauss-Seidel Line Relaxation," *Computers & Fluids*, Vol. 17, No. 1, 1989, pp. 135-150.
- [31] Gaitonde, D., and Shang, J. L., and "A Numerical Study of Viscous Shock-On-Shock Hypersonic Flows with a Modified Steger-Warming Flux Split Scheme," AIAA Paper No. 90-1941, 1990.
 - [32] Imlay, S.T., "Numerical Solution of 2-D Thrust Reversing and Thrust Vectoring Nozzle Flowfields," AIAA Paper No. 86-0203, 1986.
 - [33] McMaster, D. L., Shang, J. L., and Gaitonde, D., "A Vectorized Gauss-Seidel Line Relaxation Scheme for Solving 3D Navier-Stokes Equations," AIAA Paper No. 89-1948CP, 1989.
 - [34] Candler, G. V., and McCormack, R. W., "Hypersonic Flow Past 3-D Configurations," AIAA Paper No. 87-0480, 1987.
 - [35] Rai, M. M. and Chaussee, D. S., "New Implicit Boundary Procedures: Theory and Applications," *AIAA Journal*, Vol. 22, No. 8, August 1984, pp. 1094-1100.
 - [36] Chakravarthy, S. R., "Euler Equation-Implicit Schemes and Implicit Boundary Conditions," *AIAA Journal*, Vol. 21, No. 5, May 1983, pp. 699-706.
 - [37] Molvik, G. A., Choi, D., and Merkle, C. L., "A Two-dimensional Analysis of Laser Heat Addition in a Constant Absorptivity Gas," *AIAA Journal*, Vol. 23, No. 7, July 1985, pp. 1053-1060.
 - [38] Merkle, C. L. and Choi, Y.-H., "Computation of Low-Speed Flow with Heat Addition," *AIAA Journal*, Vol. 25, No. 6, June 1987, pp. 831-838.
 - [39] Chang, C. L., "Time-Iterative Solutions of Viscous Supersonic Flow," Ph.D. Dissertation, The Pennsylvania State University, 1988.
 - [40] Dutton, J. C., "Swirling Supersonic Nozzle Flow," *J. Propulsion and Power*, Vol. 3, No. 4, July-August 1987, pp. 342-349.
 - [41] Dutton, J. C., "Analysis of Swirling Nozzle Flow by a Time-Dependent Finite Difference Technique," Mechanical Engineering Department, Texas A&M University, College Station, Rept. TEES-TR-4990-84-01, Dec. 1984.
 - [42] Chang, C.-L. and Merkle, C. L., "Viscous Swirling Nozzle Flow," AIAA Paper 89-0280, January 1989.
 - [43] Thompson, Joe F., Thames, Frank C., and Mastin, C. Wayne, "Automatic Numerical Generation of Body -Fitted Curvilinear Coordinate System of Field Containing Any Number of Arbitrary Two-Dimensional Bodies," *J. of Computational Physics*, 15, 299-319 (1974).
 - [44] Thomas, P. D. and Middlecoff, J. F., "Direct Control of the Grid Point Distribution in Meshes Generated by Elliptic Equations," *AIAA Journal*, Vol. 18, No. 6, June 1980, p. 652.
 - [45] Thompson, Joe F.(Ed.) *Numerical Grid Generation*, Elsevier Science Publishing Co., 1982.
 - [46] Thompson, Joe F., Warsi, Z. U. A., and Mastin, C. Wayne, *Numerical Grid*

Generation, Elsevier Science Publishing Co., 1985.

- [47] Thompson, Joe F., "Grid Generation" Chapter 21 in *Handbook of Numerical Heat Transfer*, Minkowycz, W. J., et. al., Ed., Wiley, New York, 1988.
- [48] Sorenson, R. L., "A Computer Program to Generate Two-Dimensional Grids About Airfoils and Other Shapes by the Use of Poisson's Equations," NASA TM-81198, NASA Ames Research Center, 1980.
- [49] Cuffel, R. F., Back, L. H., and Massier, P.F., "Transonic Flow Field in a Supersonic Nozzle with Small Throat Radius of Curvature," *AIAA Journal*, Vol. 7, No. 7, July 1969, pp. 1364-1366.
- [50] Back, L. H., and Cuffel, R. F., "Detection of Oblique Shocks in a Conical Nozzle with a Circular-Arc Throat," *AIAA Journal*, Vol. 4, No. 12, December 1966, pp. 2219-2221.
- [51] Back, L. H., Massier, P.F., and Gier, H. L., "Comparison of Measured and Predicted Flows Through Conical Supersonic Nozzles with Emphasis on the Transonic Region," *AIAA Journal*, Vol. 3, No. 9, Sept. 1965.
- [52] Carpenter, P.W. and Johannesen, N.H., "An Extension of One-Dimensional Theory to Inviscid Swirling Flow through Choked Nozzles," *Aeronautical Quarterly*, Vol. 26, May 1975, pp. 71-87.
- [53] Pandolfi, M., "Transonic Swirling Flow in Axisymmetric Nozzles," *Meccanica*, Vol. 11, Sept. 1976, pp. 157-161.
- [54] Hoffman, J.D., Thompson, H.D., and Marcum, D.L., "An Analytical Investigation of the Effects of Swirler Design on the Performance of Annular Nozzles", AIAA Paper 86-0567, 1986.
- [55] Kornblum, B.T., Thompson, H.D., and Hoffman, J.D., "An Analytical Investigation of Swirl in Annular Propulsive Nozzles," *J. Propulsion and Power*, Vol. 2, No. 4, March-April 1986, pp. 155-160.
- [56] Kushida, R., Hermel, J., Apfel, S., and Zydowicz, M., "Performance of High-Area-Ratio Nozzle for a Small Rocket Thruster" *J. Propulsion and Power*, Vol. 3, No. 4, 1987, pp. 329-333.
- [57] Loth, E., Baum, J., and Lohner, R., "Formation of Shocks Within Axisymmetric Nozzles," AIAA Paper No. 90-1655, 1990.
- [58] Serra, R.A., "Determination of Internal Gas Flows by a Transient Numerical Technique," *AIAA Journal*, Vol. 10, No. 5, May, 1972, pp. 603-611.
- [59] Penko, P. F., Boyd, I. D., Meissner, D. L., and DeWitt, K. J., "Pressure Measurements in a Low-Density Nozzle Plume for Code Verification," AIAA Paper 91-2110, AIAA 27th Thermophysics Conference, June 24-26, 1991.
- [60] Grossman, B. and Walters, R. W., "Flux-split algorithms for the Multi-dimensional Euler Equations with Real Gases," *Computers & Fluids*, Vol. 17, No. 1, pp.99-112, 1989.

Appendix A

Derivation of Quasi-neutrality Condition

The justification for assuming a plasma is quasi-neutral arises from an examination of one of Maxwell's Equations:

$$\hat{\nabla} \cdot \hat{\mathbf{E}} = \hat{\rho}_e / \hat{\epsilon}_0 \quad (\text{A1})$$

where: $\hat{}$ indicates a dimensional quantity
 ρ_e is the net space charge density (coul/m³)
and ϵ_0 is the permittivity of vacuum (farad/m)
 $= 8.85 \times 10^{-12}$ coul² sec² / (kg m³)

The following non-dimensional quantities are defined :

$$\hat{\nabla} = \frac{\nabla}{r_{th}}$$

$$\hat{\rho}_e = \rho_e (e \cdot n_e)$$

where e is the electron charge
 $= 1.60207 \times 10^{-19}$ coul / electron

n_e is the number of electrons / m³

and

$$\hat{\mathbf{E}} = \vec{\mathbf{E}} (k_B T / e r_{th})$$

k_B is Boltzmann's Constant
 $= 1.381 \times 10^{-23}$ (kg m²) / (sec² K)

The quantity $(k_B T / e r_{th})$ is the ratio of the thermal energy to the electric charge of an electron and is a measure of the ability of an electron to move away from an ion. If the

distance an electron is separated from an ion is small then the plasma is essentially neutral in comparison to the macroscopic length scale of the flow, r_{th} . The thermal energy (voltage potential) is not large enough for the electron to overcome its attraction to the ion and thus the flow is quasi-neutral over the macroscopic dimensions of the flow. However, the flow is not neutral on a length scale that has dimensions on the order of the electron-ion separation distance.

Substituting the non-dimensional quantities into Eq. (A1) yields:

$$\nabla \cdot \vec{E} = \rho_e \frac{r_{th}^2}{\left(\frac{\epsilon_0 k_B T}{n_e e^2} \right)} \quad (A2)$$

Recalling that the Debye shielding length, λ_D , is the maximum distance over which an ionized gas may be non-neutral, on the average, depends on the number density of charge particles and their mean thermal speed and is defined as

$$\lambda_D \equiv \sqrt{\frac{\epsilon_0 k_B T}{n_e e^2}}$$

or

$$\lambda_D = 69 \sqrt{\frac{T}{n_e}} \text{ m} \quad (A3)$$

Substituting Eq. (A3) into (A2) and rearranging yields

$$\rho_e = \frac{\nabla \cdot \vec{E}}{\left(\frac{r_{th}}{\lambda_D} \right)^2} = \frac{\nabla \cdot \vec{E}}{\left(\frac{r_{th}^2}{69^2 T / n_e} \right)} \quad (A4)$$

For $r_{th} = 2.0 \times 10^{-4}$ m, $T = 10,000$ K, and $n_e = 2 \times 10^{21}$ electrons/m³ [26] we find:

$$\rho_e = (6.0 \times 10^{-7}) \nabla \cdot \vec{E} \approx 0$$

and

$$\lambda_D = 1.54 \times 10^{-7} \text{ m}$$

where λ_D is the maximum distance over which an ionized gas may be considered non-neutral. Compared to the macroscopic length scale of the thruster, r_{th} , λ_D is 10^3 smaller. Consequently, ρ_e , which is a measure of the net spatial charge of the plasma, is approximately zero and an assumption the plasma is quasi-neutral is justified. Thus,

$$\nabla \cdot \vec{E} \approx 0.$$

Appendix B

Coordinate Transformation and Derivation of the Transformed Governing Equations

Consider the transformation from the physical domain (z,r) to the computational domain (ξ,η) where

$$\xi = \xi(z,r)$$

and

$$\eta = \eta(z,r)$$

Applying the chain rule of partial differentiation to this pair yields

$$\frac{\partial}{\partial z} = \frac{\partial \xi}{\partial z} \frac{\partial}{\partial \xi} + \frac{\partial \eta}{\partial z} \frac{\partial}{\partial \eta}$$

$$\frac{\partial}{\partial r} = \frac{\partial \xi}{\partial r} \frac{\partial}{\partial \xi} + \frac{\partial \eta}{\partial r} \frac{\partial}{\partial \eta}$$

and

$$d\xi = \xi_z dz + \xi_r dr$$

$$d\eta = \eta_z dz + \eta_r dr$$

So

$$\begin{bmatrix} d\xi \\ d\eta \end{bmatrix} = \begin{bmatrix} \xi_z & \xi_r \\ \eta_z & \eta_r \end{bmatrix} \begin{bmatrix} dz \\ dr \end{bmatrix}$$

Similarly,

$$\begin{bmatrix} dz \\ dr \end{bmatrix} = \begin{bmatrix} z_\xi & z_\eta \\ r_\xi & r_\eta \end{bmatrix} \begin{bmatrix} d\xi \\ d\eta \end{bmatrix}$$

Therefore,

$$\begin{bmatrix} \xi_z & \xi_r \\ \eta_z & \eta_r \end{bmatrix} = \begin{bmatrix} z_\xi & z_\eta \\ r_\xi & r_\eta \end{bmatrix}^{-1}$$

Taking the inverse yields

$$\begin{bmatrix} \xi_z & \xi_r \\ \eta_z & \eta_r \end{bmatrix} = J \begin{bmatrix} r_\eta & -z_\eta \\ -r_\xi & z_\xi \end{bmatrix}$$

where J is the Jacobian of the transformation given by

$$\begin{aligned} J &= \xi_z \eta_r - \xi_r \eta_z \\ &= 1 / (z_\xi r_\eta - z_\eta r_\xi) \\ &= 1 / V_{ij} = 1 / (\text{cell volume}) \end{aligned}$$

and the metrics are

$$\begin{aligned} \xi_z &= J r_\eta & \xi_r &= -J z_\eta \\ \eta_z &= -J r_\xi & \eta_r &= J z_\xi \end{aligned}$$

By defining the normalized metrics

$$\begin{aligned} s_{iz} &= \frac{\xi_z}{\sqrt{\xi_z^2 + \xi_r^2}} = \frac{r_\eta}{\sqrt{z_\eta^2 + r_\eta^2}} & s_{ir} &= \frac{\xi_r}{\sqrt{\xi_z^2 + \xi_r^2}} = \frac{-z_\eta}{\sqrt{z_\eta^2 + r_\eta^2}} \\ s_{jz} &= \frac{\eta_z}{\sqrt{\eta_z^2 + \eta_r^2}} = \frac{-r_\xi}{\sqrt{z_\xi^2 + r_\xi^2}} & s_{jr} &= \frac{\eta_r}{\sqrt{\eta_z^2 + \eta_r^2}} = \frac{z_\xi}{\sqrt{z_\xi^2 + r_\xi^2}} \end{aligned}$$

the normal and tangential velocity components (see Fig. B.1) to surfaces of constant ξ and η can be defined [46 and/or 47].

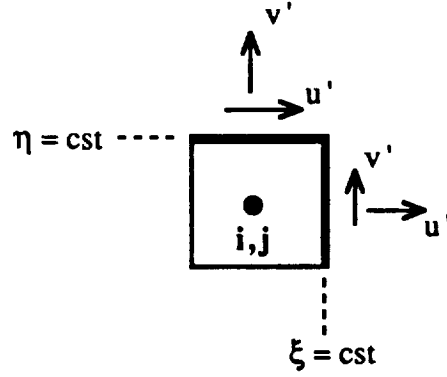


Figure B.1 Normal and Tangential Velocity Components at Surfaces of Constant η and ξ

The velocity components normal and tangential to a surface of $\xi = \text{cst.}$ located on the surface at $(i + 1/2, j)$ are

$$\begin{aligned} u' &= s_{iz} u + s_{ir} v \\ &= \frac{r_\eta u + (-z_\eta) v}{d_A} \end{aligned} \quad \begin{aligned} v' &= -s_{ir} u + s_{iz} v \\ &= \frac{-(-z_\eta) u + r_\eta v}{d_A} \end{aligned}$$

where

$$d_A = \sqrt{r_\eta^2 + z_\eta^2}$$

The velocity components normal and tangential to a surface of $\eta = \text{cst.}$ located on the surface at $(i, j + 1/2)$ are

$$\begin{aligned} v' &= s_{jz} u + s_{jr} v \\ &= \frac{-r_\xi u + z_\xi v}{d_B} \end{aligned} \quad \begin{aligned} u' &= s_{jr} u - s_{jz} v \\ &= \frac{z_\xi u - (-r_\xi) v}{d_B} \end{aligned}$$

where

$$d_B = \sqrt{r_\xi^2 + z_\xi^2}$$

Alternatively, the contravariant velocity components can be defined as

$$U = \xi_z u + \xi_r v \quad V = \eta_z u + \eta_r v$$

Therefore, $\frac{U}{J} = u' d_A \quad \frac{V}{J} = v' d_B$

Applying this transformation to the governing equations

$$\frac{\partial \vec{Q}}{\partial t} + \frac{\partial \vec{F}'}{\partial z} + \frac{\partial \vec{G}'}{\partial r} + \vec{H}' = 0 \quad (\text{B1})$$

yields

$$\vec{Q}_t + \xi_z \vec{F}'_\xi + \eta_z \vec{F}'_\eta + \xi_r \vec{G}'_\xi + \eta_r \vec{G}'_\eta + \vec{H}' = 0 \quad (\text{B2})$$

Dividing by the Jacobian and adding and subtracting like terms [27] yields

$$\begin{aligned} \left(\frac{\vec{Q}}{J} \right)_t + \left(\frac{\xi_z \vec{F}' + \xi_r \vec{G}'}{J} \right)_\xi + \left(\frac{\eta_z \vec{F}' + \eta_r \vec{G}'}{J} \right)_\eta + \frac{\vec{H}'}{J} \\ - \vec{F}' \left(\left(\frac{\xi_z}{J} \right)_\xi + \left(\frac{\eta_z}{J} \right)_\eta \right) - \vec{G}' \left(\left(\frac{\xi_r}{J} \right)_\xi + \left(\frac{\eta_r}{J} \right)_\eta \right) = 0 \end{aligned} \quad (\text{B3})$$

Substituting the metrics into the last two terms of Eq. (B3) and performing the indicated differentiation (switching the order of differentiation first) shows these terms sum to zero. Defining the quantities

$$\begin{aligned} \hat{Q} &= \frac{\vec{Q}}{J} \\ \hat{F}' &= \frac{\xi_z \vec{F}' + \xi_r \vec{G}'}{J} \\ \hat{G}' &= \frac{\eta_z \vec{F}' + \eta_r \vec{G}'}{J} \\ \hat{H}' &= \frac{\vec{H}'}{J} \end{aligned} \quad (\text{B4})$$

and using the definition of the contravariant velocity components, the governing equations in the transformed coordinate system may be written

$$\frac{\partial \hat{Q}}{\partial t} + \frac{\partial \hat{F}'}{\partial \xi} + \frac{\partial \hat{G}'}{\partial \eta} + \hat{H}' = 0 \quad (\text{B5})$$

where the vectors $\hat{Q}, \hat{F}', \hat{G}', \hat{H}'$ are the $\vec{Q}, \vec{F}', \vec{G}', \vec{H}'$ vectors in the transformed coordinate system. Splitting the \hat{F}', \hat{G}' , and \hat{H}' vectors into inviscid and viscous components yields

$$\frac{\partial \hat{Q}}{\partial t} + \frac{\partial \hat{F}}{\partial \xi} + \frac{\partial \hat{F}_v}{\partial \xi} + \frac{\partial \hat{G}}{\partial \eta} + \frac{\partial \hat{G}_v}{\partial \eta} + \hat{H} + \hat{H}_v = 0 \quad (\text{B6})$$

where

$$\hat{Q} = \frac{1}{J} \begin{bmatrix} \rho \\ \rho u \\ \rho v \\ \rho w \\ E_t \end{bmatrix}$$

$$\hat{F} = \frac{1}{J} \begin{bmatrix} \rho U \\ \rho u U + \xi_z P \\ \rho v U + \xi_r P \\ \rho w U \\ \{E_t + P\} U \end{bmatrix}$$

$$\hat{F}_v = \frac{1}{J} \begin{bmatrix} 0 \\ \xi_z \frac{\widehat{\tau_{zz}}}{Re} + \xi_r \frac{\widehat{\tau_{rz}}}{Re} \\ \xi_z \frac{\widehat{\tau_{rz}}}{Re} + \xi_r \frac{\widehat{\tau_{rr}}}{Re} \\ \xi_z \frac{\widehat{\tau_{\theta z}}}{Re} + \xi_r \frac{\widehat{\tau_{r\theta}}}{Re} \\ - \frac{1}{Re Pr (\gamma_0 - 1)} \left(\xi_z k \frac{\partial T}{\partial z} + \xi_r k \frac{\partial T}{\partial r} \right) \end{bmatrix}$$

$$\hat{G} = \frac{1}{J} \begin{bmatrix} \rho V \\ \rho u V + \eta_z P \\ \rho v V + \eta_r P \\ \rho w V \\ \{E_t + P\} V \end{bmatrix}$$

$$\hat{G}_v = \frac{1}{J} \begin{bmatrix} 0 \\ \eta_z \frac{\widehat{\tau_{zz}}}{Re} + \eta_r \frac{\widehat{\tau_{rz}}}{Re} \\ \eta_z \frac{\widehat{\tau_{rz}}}{Re} + \eta_r \frac{\widehat{\tau_{rr}}}{Re} \\ \eta_z \frac{\widehat{\tau_{\theta z}}}{Re} + \eta_r \frac{\widehat{\tau_{r\theta}}}{Re} \\ - \frac{1}{Re Pr (\gamma_0 - 1)} \left(\eta_z k \frac{\partial T}{\partial z} + \eta_r k \frac{\partial T}{\partial r} \right) \end{bmatrix}$$

$$\hat{H} = \frac{1}{J} \begin{bmatrix} \frac{\rho v}{r} \\ \frac{\rho uv}{r} \\ \frac{\rho v^2}{r} - \frac{\rho w^2}{r} \\ \frac{2}{r} \rho vw \\ \left(E_t + P \right) \frac{v}{r} \end{bmatrix}$$

$$\hat{H}_v = \frac{1}{J} \begin{bmatrix} 0 \\ - \frac{P_M}{\gamma_0} j_r B_\theta + \frac{\widehat{\tau_{rz}}}{r Re} \\ \frac{P_M}{\gamma_0} j_z B_\theta + \frac{\widehat{\tau_{rr}}}{r Re} - \frac{\widehat{\tau_{\theta\theta}}}{r Re} \\ \frac{2 \widehat{\tau_{r\theta}}}{r Re} \\ - \frac{1}{r} \frac{1}{Re Pr (\gamma_0 - 1)} k \frac{\partial T}{\partial r} - \frac{R_L}{Re Pr (\gamma_0 - 1)} \frac{j^2}{\sigma} + \dots \\ \dots + \frac{R_S}{Re Pr (\gamma_0 - 1)} S_R - \frac{5}{2} \frac{R_C}{Re Pr (\gamma_0 - 1)} \left(\frac{\partial T}{\partial r} + \frac{\partial T}{\partial z} \right) \end{bmatrix}$$

Next the Thin Layer Approximation (TLA) is applied to the governing equations. This assumes viscous terms with streamwise derivatives are small compared to the viscous terms containing transverse derivatives, and causes terms containing

$$\frac{\partial}{\partial \xi}$$

to be neglected. Thus, the term

$$\frac{\partial \widehat{E}_v}{\partial \xi}$$

is neglected and the partial derivatives become

$$\frac{\partial}{\partial z} = \eta_z \frac{\partial}{\partial \eta} \quad \text{and} \quad \frac{\partial}{\partial r} = \eta_r \frac{\partial}{\partial \eta}$$

The shear stress and heat conduction terms become

$$\widehat{\tau}_{rr} = -\frac{2}{3} \mu \left[2 \eta_r \frac{\partial v}{\partial \eta} - \eta_z \frac{\partial u}{\partial \eta} \right] + \frac{2}{3} \mu \frac{v}{r}$$

$$\widehat{\tau}_{\theta\theta} = -\frac{2}{3} \mu \left[-\left(\eta_r \frac{\partial v}{\partial \eta} + \eta_z \frac{\partial u}{\partial \eta} \right) \right] - \frac{4}{3} \mu \frac{v}{r}$$

$$\widehat{\tau}_{zz} = -\frac{2}{3} \mu \left[2 \eta_z \frac{\partial u}{\partial \eta} - \eta_r \frac{\partial v}{\partial \eta} \right] + \frac{2}{3} \mu \frac{v}{r}$$

$$\widehat{\tau}_{r\theta} = -\mu \left[\eta_r \frac{\partial w}{\partial \eta} \right] + \mu \frac{w}{r}$$

$$\widehat{\tau}_{\theta z} = -\mu \left[\eta_z \frac{\partial w}{\partial \eta} \right]$$

$$\widehat{\tau}_{rz} = -\mu \left[\eta_r \frac{\partial u}{\partial \eta} + \eta_z \frac{\partial v}{\partial \eta} \right]$$

$$\frac{\partial T}{\partial z}, \frac{\partial T}{\partial r} \Rightarrow \xi_z \frac{\partial T}{\partial \eta}, \eta_r \frac{\partial T}{\partial \eta}$$

Using the rotated velocity components u' and v' the final set of governing equations and components are

$$\frac{1}{J} \frac{\partial \vec{Q}}{\partial t} + \frac{\partial \hat{F}}{\partial \xi} + \frac{\partial \hat{G}}{\partial \eta} + \frac{\partial \hat{G}_v}{\partial \eta} + \hat{H} + \hat{H}_v = 0 \quad (B8)$$

where

$$\vec{Q} = \begin{bmatrix} \rho \\ \rho u \\ \rho v \\ \rho w \\ E_t \end{bmatrix}$$

$$\hat{F} = d_A \begin{bmatrix} \rho u' \\ \rho u u' + \frac{1}{d_A} r_\eta P \\ \rho v u' + \frac{-1}{d_A} z_\eta P \\ \rho w u' \\ \{E_t + P\} u' \end{bmatrix}$$

$$\hat{G} = d_B \begin{bmatrix} \rho v' \\ \rho u v' + \frac{-1}{d_B} r_\xi P \\ \rho v v' + \frac{1}{d_B} z_\xi P \\ \rho w v' \\ \{E_t + P\} v' \end{bmatrix}$$

where u' and v' are the rotated velocity components normal to surfaces of constant ξ and η , respectively.

$$\hat{G}_v = \frac{1}{Re} \begin{bmatrix} 0 \\ J(\beta_4 u_\eta + \beta_2 v_\eta) - \frac{2\mu}{3r} r_\xi v \\ J(\beta_2 u_\eta + \beta_1 v_\eta) + \frac{2\mu}{3r} z_\xi v \\ J\beta_3 w_\eta + \frac{\mu}{r} z_\xi w \\ \frac{J}{Re Pr (\gamma_0 - 1)} \beta_5 \frac{\partial T}{\partial \eta} \end{bmatrix}$$

where

$$\beta_1 = -\mu \left(\frac{4}{3} z_\xi^2 + r_\xi^2 \right)$$

$$\beta_2 = \frac{1}{3} \mu z_\xi r_\xi$$

$$\beta_3 = -\mu (z_\xi^2 + r_\xi^2)$$

$$\beta_4 = -\mu \left(z_\xi^2 + \frac{4}{3} r_\xi^2 \right)$$

$$\beta_5 = -k (z_\xi^2 + r_\xi^2)$$

$$\hat{H} = \frac{1}{J} \begin{bmatrix} \frac{\rho v}{r} \\ \frac{\rho u v}{r} \\ \frac{\rho v^2}{r} - \frac{\rho w^2}{r} \\ \frac{2}{r} \rho v w \\ (E_t + P) \frac{v}{r} \end{bmatrix}$$

$$\hat{H}_v = \begin{bmatrix} 0 \\ -\frac{P_M}{J \gamma_0} j_r B_\theta - \frac{\mu}{r \text{Re}} (z_\xi u_\eta - r_\xi v_\eta) \\ \frac{P_M}{J \gamma_0} j_z B_\theta + \frac{2\mu}{r \text{Re}} \left(\frac{v}{J r} - z_\xi v_\eta \right) \\ \frac{2\mu}{r \text{Re}} \left(\frac{w}{J r} - z_\xi w_\eta \right) \\ -\frac{k z_\xi T_\eta}{r \text{Re Pr} (\gamma_0 - 1)} - \frac{R_L}{J \text{Re Pr} (\gamma_0 - 1)} \frac{j^2}{\sigma} + \dots \\ \dots + \frac{R_S}{J \text{Re Pr} (\gamma_0 - 1)} S_R - \frac{5}{2} \frac{R_C}{\text{Re Pr} (\gamma_0 - 1)} (z_\xi j_r - r_\xi j_z) T_\eta \end{bmatrix}$$

It should be noted that j_r, j_z, B_θ , represent the radial current component, axial current component, and circumferential magnetic field, respectively and are not the radial, axial, and circumferential derivatives. All other subscripts denote a derivative with respect to the subscripted variable.

Lastly, using the chain rule of partial differentiation, the coordinate transformation is applied to the equation governing the electromagnetic field to yield

$$\begin{aligned} & \eta_z \frac{\partial}{\partial \eta} \left(\frac{1}{\sigma} (\eta_z B_\eta + \xi_z B_\xi) \right) + \xi_z \frac{\partial}{\partial \xi} \left(\frac{1}{\sigma} (\eta_z B_\eta + \xi_z B_\xi) \right) \\ & + \eta_r \frac{\partial}{\partial \eta} \left(\frac{1}{\sigma} (\eta_r B_\eta + \xi_r B_\xi + \frac{B}{r}) \right) + \xi_r \frac{\partial}{\partial \xi} \left(\frac{1}{\sigma} (\eta_r B_\eta + \xi_r B_\xi + \frac{B}{r}) \right) = 0 \end{aligned} \quad (B9)$$

Appendix C

Derivation of the Inviscid Flux Vector Jacobians

Flux splitting of the rotated inviscid flux vectors, \hat{F} and \hat{G} , is achieved by decomposing the inviscid flux into two components. One component contains the eigenvalues traveling in the positive coordinate direction and the other component contains the eigenvalues traveling in the negative coordinate direction. The purpose of this appendix is to illustrate how the Jacobian matrices of \hat{F} and \hat{G} are diagonalized by the matrix of eigenvalues, λ .

The rotated inviscid flux vectors can be represented as the product of a rotated Jacobian matrix, A and B , respectively, and the solution vector \vec{Q}

$$\hat{F} = \frac{\partial \hat{F}}{\partial \vec{Q}} \vec{Q} = A \vec{Q} \quad \hat{G} = \frac{\partial \hat{G}}{\partial \vec{Q}} \vec{Q} = B \vec{Q} \quad (C1)$$

Recalling the definition of \hat{F} from Appendix B, for example

$$\hat{F} = d_A \begin{bmatrix} \rho u' \\ \rho u u' + \frac{1}{d_A} r_\eta P \\ \rho v u' + \frac{-1}{d_A} z_\eta P \\ \rho w u' \\ \{E_t + P\} u' \end{bmatrix}$$

and

$$u' = s_{iz}u + s_{ir}v$$

where u' is the velocity normal to a surface of $\xi = \text{cst}$ and s_{iz} and s_{ir} are the normalized metrics presented in Appendix B. The solution vector is given by

$$\vec{Q} = \begin{bmatrix} \rho \\ \rho u \\ \rho v \\ \rho w \\ E_t \end{bmatrix} = \begin{bmatrix} Q_1 \\ Q_2 \\ Q_3 \\ Q_4 \\ Q_5 \end{bmatrix}$$

The rotated Jacobian matrices can also be written in terms of the vector of primitive variables, \vec{V} ,

$$A = \frac{\partial \hat{F}}{\partial \vec{Q}} = \frac{\partial \vec{Q}}{\partial \vec{V}} \cdot \frac{\partial \vec{V}}{\partial \vec{Q}} \frac{\partial \hat{F}}{\partial \vec{V}} \cdot \frac{\partial \vec{V}}{\partial \vec{Q}} \quad (C1)$$

and

$$B = \frac{\partial \hat{G}}{\partial \vec{Q}} = \frac{\partial \vec{Q}}{\partial \vec{V}} \cdot \frac{\partial \vec{V}}{\partial \vec{Q}} \frac{\partial \hat{G}}{\partial \vec{V}} \cdot \frac{\partial \vec{V}}{\partial \vec{Q}}$$

where

$$\vec{V} = [\rho \ u \ v \ w \ P]^T = [V_1 \ V_2 \ V_3 \ V_4 \ V_5]^T$$

Define

$$S = \frac{\partial \vec{V}}{\partial \vec{Q}} \quad \text{and} \quad S^{-1} = \frac{\partial \vec{Q}}{\partial \vec{V}} \quad (C2)$$

and diagonalize the Jacobian $\frac{\partial \vec{V}}{\partial \vec{Q}} \frac{\partial \hat{F}}{\partial \vec{V}}$ (as opposed to $\frac{\partial \hat{F}}{\partial \vec{Q}}$, which is more difficult to diagonalize) as

$$\frac{\partial \vec{V}}{\partial \vec{Q}} \frac{\partial \hat{F}}{\partial \vec{V}} = C_A^{-1} \Lambda_A C_A$$

The rotation matrix, R_A , which contains the normalized metrics and which transforms the velocities between the Cartesian and the transformed coordinate system, can be defined [refer to 29, 60] so that $C_{A'} = C_A R_A$ and the Jacobian becomes

$$\frac{\partial \vec{V}}{\partial \vec{Q}} \frac{\partial \hat{F}}{\partial \vec{V}} = R_A^{-1} C_A^{-1} \Lambda_A C_A R_A \quad (C3)$$

where

$$R_A = \begin{bmatrix} 1 & 0 & 0 & 0 & 0 \\ 0 & s_{iz} & s_{ir} & 0 & 0 \\ 0 & -s_{ir} & s_{iz} & 0 & 0 \\ 0 & 0 & 0 & 1 & 0 \\ 0 & 0 & 0 & 0 & 1 \end{bmatrix}$$

Substituting Eqs. (C2) and (C3) into (C1) yields

$$A = S^{-1} R_A^{-1} C_A^{-1} \Lambda_A C_A R_A S$$

Similarly

$$B = S^{-1} R_B^{-1} C_B^{-1} \Lambda_B C_B R_B S$$

(C4)

The Jacobian S is found by first writing the vector of primitive variables, \vec{V} , in terms of the solution vector, \vec{Q} .

$$\vec{V} = \begin{bmatrix} V_1 \\ V_2 \\ V_3 \\ V_4 \\ V_5 \end{bmatrix} = \begin{bmatrix} Q_1 \\ \frac{Q_2}{Q_1} \\ \frac{Q_3}{Q_1} \\ \frac{Q_4}{Q_1} \\ \beta \left(Q_5 - \frac{1}{2 Q_1} (Q_2^2 + Q_3^2 + Q_4^2) \right) \end{bmatrix}$$

From which the following may be evaluated

$$S = \begin{bmatrix} \frac{\partial V_1}{\partial Q_1} & \frac{\partial V_1}{\partial Q_2} & \frac{\partial V_1}{\partial Q_3} & \frac{\partial V_1}{\partial Q_4} & \frac{\partial V_1}{\partial Q_5} \\ | & - & - & - & | \\ | & - & - & - & | \\ | & - & - & - & | \\ \frac{\partial V_5}{\partial Q_1} & - & - & - & \frac{\partial V_5}{\partial Q_5} \end{bmatrix}$$

Thus,

$$S = \begin{bmatrix} 1 & 0 & 0 & 0 & 0 \\ -u/\rho & 1/\rho & 0 & 0 & 0 \\ -v/\rho & 0 & 1/\rho & 0 & 0 \\ -w/\rho & 0 & 0 & 1/\rho & 0 \\ \beta \alpha & -\beta u & -\beta v & -\beta w & \beta \end{bmatrix}$$

where $\beta = (\gamma - 1)$ $\alpha = \frac{1}{2}(u^2 + v^2 + w^2)$

In a similar manner S^{-1} is found, by placing \vec{Q} in terms of \vec{V} and evaluating $S^{-1} = \frac{\partial \vec{Q}}{\partial \vec{V}}$, to be

$$S^{-1} = \begin{bmatrix} 1 & 0 & 0 & 0 & 0 \\ u & \rho & 0 & 0 & 0 \\ v & 0 & \rho & 0 & 0 \\ w & 0 & 0 & \rho & 0 \\ \alpha & \rho u & \rho v & \rho w & 1/\beta \end{bmatrix}$$

Examination of Eq. (C3) shows one unknown matrix on the left hand side of the expression, $\frac{\partial \hat{F}}{\partial \vec{V}}$, which can be evaluated, by writing \hat{F} in terms of \vec{V} , to be

$$\frac{\partial \hat{F}}{\partial \vec{V}} = \begin{bmatrix} u'd_A & \rho r_\eta & -\rho z_\eta & 0 & 0 \\ uu'd_A & \rho u r_\eta + \rho u' d_A & -\rho u z_\eta & 0 & r_\eta \\ vu'd_A & v r_\eta & \rho u' d_A - \rho v z_\eta & 0 & -z_\eta \\ wu'd_A & \rho w r_\eta & -\rho w z_\eta & \rho u' d_A & 0 \\ \alpha u'd_A & \rho uu'd_A + (E_t + P) r_\eta & \rho vu'd_A - (E_t + P) z_\eta & \rho wu'd_A & \frac{\gamma}{\beta} u'd_A \end{bmatrix}$$

Rearranging Eq. (C3) and using the definition of S we can write

$$C_A^{-1} \Lambda_A C_A = R_A S \frac{\partial \hat{F}}{\partial \vec{V}} R_A^{-1} \quad (C5)$$

All matrices on the right hand side of Eq. (C5) are known. Using MACSYMA (an interactive symbolic algebra program from Symbolics, Inc., Eleven Cambridge Center, Cambridge, MA 02142) the eigenvalue problem posed by Eq. (C5) was solved. C_A^{-1} is composed of columns of right eigenvectors and Λ_A is a diagonal matrix of eigenvalues. C_A , as opposed to C_A^{-1} , is given by

$$C_A^{-1} = \begin{bmatrix} 1 & 0 & 0 & 1 & 1 \\ 0 & 0 & 0 & c/\rho & -c/\rho \\ 0 & 1 & 0 & 0 & 0 \\ 0 & 0 & 1 & 0 & 0 \\ 0 & 0 & 0 & c^2 & c^2 \end{bmatrix}$$

$$\Lambda_A = \begin{bmatrix} d_A u' & & & & \\ & d_A u' & & & 0 \\ & & d_A u' & & \\ & 0 & & d_A(u' + c) & \\ & & & & d_A(u' - c) \end{bmatrix}$$

where

$$c^2 = \frac{\gamma P}{\rho}$$

The matrices diagonalizing B, R_B , C_B , and Λ_B , can be obtained directly by substituting

v' for u'

d_B for d_A

and

$s_{jr}, -s_{jz}$ for s_{iz}, s_{ir}

in R_A , C_A , and Λ_A .

Appendix D

Implicit Viscous and Source Term Matrices

The matrices M_a and M_b arise from the derivation of the implicit differencing of the viscous flux vector, $\delta \hat{G}_v$, where

$$\hat{G}_v = \frac{1}{Re} \begin{bmatrix} 0 \\ J(\beta_4 u_\eta + \beta_2 v_\eta) - \frac{2\mu}{3r} r_\xi v \\ J(\beta_2 u_\eta + \beta_1 v_\eta) + \frac{2\mu}{3r} z_\xi v \\ J\beta_3 w_\eta + \frac{\mu}{r} z_\xi w \\ \frac{J}{Re Pr (\gamma_0 - 1)} \beta_5 \frac{\partial T}{\partial \eta} \end{bmatrix}$$

By partitioning the vector into: 1) the terms common to both the cartesian and cylindrical formulations and 2) the additional terms arising from the cylindrical axisymmetric formulation (in \hat{G}_v shown above, the three terms containing $1/r$ are the additional terms arising from the cylindrical coordinate formulation) such that

$$\hat{G}_v = \hat{G}_{vcom} + \hat{G}_{vcyl}$$

Differentiating this expression with respect to time, multiplying by Δt and using the definition of $\delta \hat{F}_v$

$$\delta \hat{G}_v \equiv \hat{G}_v^{n+1} - \hat{G}_v^n = \Delta t \frac{\partial \hat{G}_v}{\partial t}$$

we can write

$$\delta \hat{G}_v = \delta \hat{G}_{vcom} + \delta \hat{G}_{vcyl}$$

Employing the vector of primitive variables, \vec{V}

$$\vec{V} = (\rho \ u \ v \ w \ T)^T$$

we can write
$$\delta \hat{G}_v = M_a \frac{\partial}{\partial \eta} \delta \vec{V} + \delta \hat{G}_{v \text{ cyl}}$$

because $\delta \hat{G}_v$ contains derivatives of the primitive variables with respect to η only. The quantity $\frac{\partial}{\partial \eta} \delta \vec{V}$ can be derived and then M_a found such that $M_a \frac{\partial}{\partial \eta} \delta \vec{V} = \delta \hat{G}_v$. M_a is found to be

$$M_a = \frac{1}{Re} \begin{bmatrix} 0 & 0 & 0 & 0 & 0 \\ 0 & \beta_4 & \beta_2 & 0 & 0 \\ 0 & \beta_2 & \beta_1 & 0 & 0 \\ 0 & 0 & 0 & \beta_3 & 0 \\ 0 & 0 & 0 & 0 & \frac{1}{Pr(\gamma_0-1)} \beta_5 \end{bmatrix}$$

with

$$\delta \vec{V} = (\delta \rho \ \delta u \ \delta v \ \delta w \ \delta T)^T$$

$$\beta_1 = -\mu \left(\frac{4}{3} z_\xi^2 + r_\xi^2 \right)$$

$$\beta_2 = \frac{1}{3} \mu z_\xi r_\xi$$

$$\beta_3 = -\mu (z_\xi^2 + r_\xi^2)$$

$$\beta_4 = -\mu \left(z_\xi^2 + \frac{4}{3} r_\xi^2 \right)$$

$$\beta_5 = -k (z_\xi^2 + r_\xi^2)$$

We can change variables from $\delta \vec{V}$ to $\delta \vec{Q}$ by defining the Jacobian N where $N = \frac{\partial \vec{V}}{\partial \vec{Q}}$ such that $\delta \vec{V} = N \delta \vec{Q}$. In addition, $\delta \hat{G}_{v \text{ cyl}}$ can be expressed in terms of $\delta \vec{Q}$ such that

$$\delta \hat{G}_v = M_a \frac{\partial N \delta \vec{Q}}{\partial \eta} + M_b \delta \vec{Q}$$

The Jacobian, N, is found to be

$$N = \frac{1}{\rho} \begin{bmatrix} 1 & 0 & 0 & 0 & 0 \\ -u & 1 & 0 & 0 & 0 \\ -v & 0 & 1 & 0 & 0 \\ -w & 0 & 0 & 1 & 0 \\ \varepsilon(2\alpha - e_t) & -\varepsilon u & -\varepsilon v & -\varepsilon w & \varepsilon \end{bmatrix}$$

where

$$\varepsilon = \gamma_0 (\gamma - 1)$$

$$\alpha = \frac{u^2 + v^2 + w^2}{2}$$

by evaluating

$$N = \begin{bmatrix} \frac{\partial V_1}{\partial Q_1} & \frac{\partial V_1}{\partial Q_2} & \frac{\partial V_1}{\partial Q_3} & \frac{\partial V_1}{\partial Q_4} & \frac{\partial V_1}{\partial Q_5} \\ | & - & - & - & | \\ | & - & - & - & | \\ | & - & - & - & | \\ \frac{\partial V_5}{\partial Q_1} & - & - & - & \frac{\partial V_5}{\partial Q_5} \end{bmatrix}$$

after placing V_1 - V_5 in terms of Q_1 - Q_5 . It should also be noted that in deriving the fifth row of N, γ was assumed to be locally independent of \vec{Q} .

In a similar manner $\hat{G}_{v \text{ cyl}}$ is expressed in terms of Q_1 - Q_5 and then M_b is obtained by evaluating

$$M_b = \frac{\partial \hat{G}_{v \text{ cyl}}}{\partial \vec{Q}}$$

$$M_b = \frac{\mu}{\rho r \text{ Re}} \begin{bmatrix} 0 & 0 & 0 & 0 & 0 \\ \frac{2}{3} r_\xi v & 0 & -\frac{2}{3} r_\xi & 0 & 0 \\ -\frac{2}{3} z_\xi v & 0 & \frac{2}{3} z_\xi & 0 & 0 \\ -z_\xi w & 0 & 0 & z_\xi & 0 \\ 0 & 0 & 0 & 0 & 0 \end{bmatrix}$$

The implicit inviscid source term, $\delta \hat{H}_{i,j}$, is placed in terms of $\delta \vec{Q}$ by writing

$$\delta \hat{H}_{i,j} = C_{li,j} \delta \vec{Q}_{i,j}$$

The inviscid source term matrix, C_I is found by rewriting \hat{H} ,

$$\hat{H} = \frac{1}{J} \begin{bmatrix} \frac{\rho v}{r} \\ \frac{\rho u v}{r} \\ \frac{\rho v^2}{r} - \frac{\rho w^2}{r} \\ \frac{2}{r} \rho v w \\ \left\{ E_t + P \right\} \frac{v}{r} \end{bmatrix}$$

in terms of Q_1 - Q_5 , and then evaluating $C_I = \frac{\partial \hat{H}}{\partial \vec{Q}}$ to obtain

$$C_I = \frac{1}{J r} \begin{bmatrix} 0 & 0 & 1 & 0 & 0 \\ -u v & v & u & 0 & 0 \\ w^2 - v^2 & 0 & 2 v & -2 w & 0 \\ -2 v w & 0 & 2 w & 2 v & 0 \\ C_{51} & C_{52} & C_{53} & C_{54} & \gamma v \end{bmatrix}$$

where

$$C_{51} = v (2 \alpha (\gamma - 1) - \gamma e_t)$$

$$C_{52} = -(\gamma - 1) u v$$

$$C_{53} = \gamma e_t - (\gamma - 1)(\alpha + v^2)$$

$$C_{54} = -(\gamma - 1) v w$$

with

$$\alpha = \frac{u^2 + v^2 + w^2}{2}$$

It should also be noted that in deriving the fifth row of C_I , as was done for N , γ was assumed to be locally independent of \vec{Q} .

Vita

Gary E. Pawlas was born on [REDACTED] in [REDACTED]. He received a B.S. degree in Mechanical Engineering from the University of Cincinnati in 1981. He was employed at the NASA Lewis Research Center in Cleveland, Ohio through a Cooperative Education Program while attending the University of Cincinnati. His M.S. degree, also in Mechanical Engineering, was obtained from the University of Colorado, Boulder in 1983.

After receiving his M.S. degree Gary was employed at A.T.&T. Bell Laboratories in Whippany, N.J. from February 1984, through August 1985. While employed at Bell Labs he was responsible for developing techniques to deployment fiber optic cable along the ocean floor. He has been employed as a Research Assistant at the University of Toledo since September 1985 in the Department of Mechanical Engineering.

Gary married Annette Arnone Pawlas in 1984 and their daughter, Lindsay, was born on June 20, 1990. They presently reside in Toledo, Ohio where Annette is a Speech-Language Pathologist at The Toledo Hospital and Gary is a Post-Doctoral Research Associate at NASA-Lewis and the University of Toledo.

REPORT DOCUMENTATION PAGE			Form Approved OMB No. 0704-0188	
Public reporting burden for this collection of information is estimated to average 1 hour per response, including the time for reviewing instructions, searching existing data sources, gathering and maintaining the data needed, and completing and reviewing the collection of information. Send comments regarding this burden estimate or any other aspect of this collection of information, including suggestions for reducing this burden, to Washington Headquarters Services, Directorate for Information Operations and Reports, 1215 Jefferson Davis Highway, Suite 1204, Arlington, VA 22202-4302, and to the Office of Management and Budget, Paperwork Reduction Project (0704-0188), Washington, DC 20503.				
1. AGENCY USE ONLY (Leave blank)	2. REPORT DATE November 1992	3. REPORT TYPE AND DATES COVERED Final Contractor Report		
4. TITLE AND SUBTITLE Numerical Modeling of a Vortex Stabilized Arcjet		5. FUNDING NUMBERS WU-506-42-31		
6. AUTHOR(S) Gary E. Pawlas				
7. PERFORMING ORGANIZATION NAME(S) AND ADDRESS(ES) University of Toledo Mechanical Engineering Department Toledo, Ohio 43606		8. PERFORMING ORGANIZATION REPORT NUMBER E-7419		
9. SPONSORING/MONITORING AGENCY NAME(S) AND ADDRESS(ES) National Aeronautics and Space Administration Lewis Research Center Cleveland, Ohio 44135-3191		10. SPONSORING/MONITORING AGENCY REPORT NUMBER NASA CR-190797		
11. SUPPLEMENTARY NOTES Project Manager, Paul F. Penko, (216) 977-7490.				
12a. DISTRIBUTION/AVAILABILITY STATEMENT Unclassified - Unlimited Subject Category 20			12b. DISTRIBUTION CODE	
13. ABSTRACT (Maximum 200 words) Arcjet thrusters are being actively considered for use in Earth orbit maneuvering applications. Satellite station-keeping is an example of a maneuvering application requiring the low thrust, high specific impulse of an arcjet. Experimental studies are currently the chief means of determining an optimal thruster configuration. Earlier numerical studies have failed to include all of the effects found in typical arcjets including complex geometries, viscosity and swirling flow. Arcjet geometries are large area ratio converging nozzles with centerbodies in the subsonic portion of the nozzle. The nozzle walls serve as the anode while the centerbody functions as the cathode. Viscous effects are important because the Reynolds number, based on the throat radius, is typically less than 1,000. Experimental studies have shown a swirl or circumferential velocity component stabilizes a constricted arc. This dissertation describes the equations governing flow through a constricted arcjet thruster. An assumption the flowfield is in local thermodynamic equilibrium leads to a single fluid plasma temperature model. An order of magnitude analysis reveals the governing fluid mechanics equations are uncoupled from the electromagnetic field equations. A numerical method is developed to solve the governing fluid mechanics equations, the Thin Layer Navier-Stokes equations. A coordinate transformation is employed in deriving the governing equations to simplify the application of boundary conditions in complex geometries. An axisymmetric formulation is employed to include the swirl velocity component as well as the axial and radial velocity components. The numerical method is an implicit finite-volume technique and allows for large time steps to reach a converged steady-state solution. The inviscid fluxes are flux-split and Gauss-Seidel line relaxation is used to accelerate convergence. Converging-diverging nozzles with exit-to-throat area ratios up to 100:1 and annular nozzles were examined. Comparisons with experimental data and previous numerical results were in excellent agreement. Quantities examined included Mach number and static wall pressure distributions, and oblique shock structures. As the level of swirl and viscosity in the flowfield increased the mass flow rate and thrust decreased. The technique was used to predict the flow through a typical arcjet thruster geometry. Results indicate swirl and viscosity play an important role in the complex geometry of an arcjet by shifting the Mach contours upstream and reducing the mass flow rate and thrust.				
14. SUBJECT TERMS Viscous nozzle flow; Swirling flow; Thin-layer Navier Stokes; Arcjet; MacCormack method			15. NUMBER OF PAGES 154	
			16. PRICE CODE A08	
17. SECURITY CLASSIFICATION OF REPORT Unclassified	18. SECURITY CLASSIFICATION OF THIS PAGE Unclassified	19. SECURITY CLASSIFICATION OF ABSTRACT Unclassified	20. LIMITATION OF ABSTRACT	

National Aeronautics and
Space Administration

Lewis Research Center
Cleveland, Ohio 44135

Official Business
Penalty for Private Use \$300

FOURTH CLASS MAIL

ADDRESS CORRECTION REQUESTED



Postage and Fees Paid
National Aeronautics and
Space Administration
NASA 451

NASA
